ELECTRIC FIELD EFFECT IN WATER DISSOCIATION ACROSS ATOMICALLY THICK GRAPHENE

A THESIS SUBMITTED TO THE UNIVERSITY OF MANCHESTER
FOR THE DEGREE OF DOCTOR OF PHILOSOPHY
IN THE FACULTY OF SCIENCE AND ENGINEERING

2021

By
Junhao Cai

Main Supervisor: Marcelo Lozada-Hidalgo
Co-supervisor: Irina Grigorieva

School of Physics and Astronomy

Contents

Word Count: 26686

List of Figures

Abstract

Intense electric fields can promote the dissociation reaction of weak electrolytes. Conventionally, high-voltage electrolysis cells are used to provide the required field intensity ($\sim 10^7\ \mathrm{V \cdot m^{-1}}$) for molecules like ammonia and acetic acid. However, such a phenomenon in water demands a more intensive field of $> 10^8\ \mathrm{V \cdot m^{-1}}$. Designing transport experiments with such high electric fields is difficult which makes observing a field effect in water much harder. Here in this thesis, we demonstrate that with a monolayer-graphene electrode that is selectively permeable to protons, it is possible to measure water dissociation reaction in a field of up to $\sim 10^9\ \mathrm{V \cdot m^{-1}}$. The water dissociation is accelerated by the strong electric field present in the electric double layer near the free-standing graphene electrode. The proton and hydroxide ions split from water molecules, they are then further separated across the two sides of the proton selective graphene interface. With a voltage bias of ~ 2 V, current densities of more than $10\ \mathrm{A \cdot cm^{-2}}$ are achieved in the field-accelerated water electrolysis. This current density outperforms traditional electrolysers with an improvement of one-two orders of magnitude. Mass transport experiments show that the H_2 and O_2 gases are generated with 100% Faradaic efficiency, providing direct evidence for water electrolysis across the graphene electrode. These findings demonstrate a physical approach to accelerate chemical reactions, which could be extended to other reactions related to proton transport and beyond.

Declaration

No portion of the work referred to in this thesis has been submitted in support of an application for another degree or qualification of this or any other university or other institute of learning.

Copyright

i. The author of this thesis (including any appendices and/or schedules to this thesis) owns certain copyright or related rights in it (the "Copyright") and s/he has given The University of Manchester certain rights to use such Copyright, including for administrative purposes.

ii. Copies of this thesis, either in full or in extracts and whether in hard or electronic copy, may be made **only** in accordance with the Copyright, Designs and Patents Act 1988 (as amended) and regulations issued under it or, where appropriate, in accordance with licensing agreements which the University has from time to time. This page must form part of any such copies made.

iii. The ownership of certain Copyright, patents, designs, trade marks and other intellectual property (the "Intellectual Property") and any reproductions of copyright works in the thesis, for example graphs and tables ("Reproductions"), which may be described in this thesis, may not be owned by the author and may be owned by third parties. Such Intellectual Property and Reproductions cannot and must not be made available for use without the prior written permission of the owner(s) of the relevant Intellectual Property and/or Reproductions.

iv. Further information on the conditions under which disclosure, publication and commercialisation of this thesis, the Copyright and any Intellectual Property and/or Reproductions described in it may take place is available in the University IP Policy (see `http://documents.manchester.ac.uk/DocuInfo.aspx?DocID=487`), in any relevant Thesis restriction declarations deposited in the University Library, The University Library's regulations (see `http://www.manchester.ac.uk/library/aboutus/regulations`) and in The University's policy on presentation of Theses.

Acknowledgements

I would like to take this opportunity to thank all the people without whom I would not have reached this point.

First and foremost, I would like to express my gratitude and appreciation to my supervisors for their continued support, especially Marcelo, for his guidance, cheerful encouragement, and endless patience. I would also like to thank China Scholarship Council for providing me with the opportunity and funding to study abroad.

I would like to thank Sheng Zhang, Guangping Hao, and Lucas Mogg for teaching me the majority of fabrication processes, the basics of measurement, and bearing with my silly questions. My gratitude extends to the technicians and cleanroom staff for their continuous maintenance of all the equipment and facilities that are essential for conducting my research.

I would like to thank my fellow PhD students, Yaping Yang, Wenjun Kuang, Tongcheng Yu, Shouqi Shao, and Yingxian Chen, for their advice and support that saved my sanity. I am also very thankful to colleagues in Marcelo's group who have helped me a lot: Donnchadh Barry, Eoin Griffin, and Victor G. Moreira. Special thanks go to my badminton buddies for their companions, with whom I had so many happy memories, not just on courts. There are certainly more people than I can mention here.

Finally, I would like to thank my family for their support both during my studies and throughout my life.

Chapter 1

Introduction

Interfaces are sites for many exciting processes, such as biological cell membrane transmitting sophisticated neural signals in the brain [1, 2], and fuel cells transforming hydrogen into clean and efficient energy to the world [3]. Exciting physics phenomena often occur with new properties introduced to the interfaces. The isolation of graphene opened an era of observing new phenomena on atomically thin interfaces. With a combination of excellent properties such as mechanical strength, electrical conductivity, and optical response, graphene becomes a promising material for future technology innovations [4].

The finding that protons can penetrate through graphene in ambient conditions without deteriorating its crystal structure enriches graphene's ability portfolio [5]. This has highlighted graphene's potential of being a core component in proton exchange membrane (PEM) fuel cells [3], and many other PEM-based applications like hydrogen isotope separation [6]. Apart from these, what new physics would we discover on interfaces that are both proton and electron conductive?

Intensive electric fields stretch and split water molecules which is the so-called Wien effect [7, 8]. The existence of an intensive electric field (gigavolt-level) near a charged electrode immersed in electrolytes is known to the scientific sphere [9].

Both of them are phenomena with well-established research. However, due to the electric screening of water, the field effect on water dissociation decays rapidly in just a few angstroms away from the electrode. This makes the observation of field effect in water only possible in some complicated high-voltage (kV-level) apparatuses, leaving a decent field effect observation in water illusive [10].

In this thesis, we demonstrate that microscale electrolysis cells made from proton-permeating graphene electrodes can accelerate the rate of the most fundamental chemical reaction, water dissociation, by two orders of magnitude. The potential-biased graphene interface provides strong E-fields that accelerates water dissociation. As a result, the proton-hydroxide pairs are separated readily by the same proton-permeable interface, preventing their recombination back to water molecules. This is a fundamentally different way to promote the rate of a chemical reaction. Further, results show that the whole water electrolysis process benefits from the field effect, achieving reaction rates surpassing the state-of-the-art water electrolysers.

The outline of this thesis is listed as follows:

In Chapter 2, we introduce fundamental concepts in electrolyte theory, which involves two important characteristic lengths, namely, the Debye length and Bjerrum length, accounting for the electrolyte screening of the electric field and the bound state of ion pairs, respectively. An overview is given on the electric double layer model, introducing its development and, of particular interest to this thesis, the field and potential profiles across the double layer. Onsager theory of the second Wien effect is introduced in the end.

Chapter 3 starts with the basics of water electrolysis. Then the mechanisms of several membrane-based water electrolysers are introduced, with an overview of the state-of-art current density performance of these electrolysers. We also introduce some additional information about the fundamentals of ion exchange membranes, which is relevant to understanding the transport properties of our devices. Finally, we reviewed the current state of studies on the field dissociation of water.

In Chapter 4, we overview graphene and its structural, mechanical, electrical, optical, and mass-transport properties. For the electrical and optical properties, we focus on the photonic hot-electron generation in graphene. In terms of mass transport, we briefly introduce the impermeability of graphene, then review studies about the proton transport across crystalline graphene.

In Chapter 5, the experimental techniques used in this thesis are introduced. We discuss the device fabrication processes from flake preparation to micro-fabrication. Characterisation methods and measurement techniques are also introduced.

The following two chapters involve all the main experimental results of this thesis.

In Chapter 6, we present the results from electrical transport experiments of our devices in the equilibrium region, proving that the water dissociation is promoted by the strong electric field in the electric double layer. With the double layer modelling help from our colleagues in Belgium, we show an excellent match between our results and Onsager theory of the Wien effect. Control experiments are also included in this chapter.

In Chapter 7, we present the results of actual water electrolysis using our graphene devices with light enhanced proton conductivity. Mass-transport data from direct H_2 and O_2 gas evolution experiments are presented, which provides direct evidence of the water electrolysis across the graphene electrode.

Chapter 8 concludes the main findings made in this thesis and gives an outlook of future research directions.

Chapter 2

Electrolyte Theories

In this chapter, we aim to introduce some concepts of electrolyte theory as a staging area of this thesis. A full overview of electrolyte theory would be well beyond the scope of this thesis. Hence, we only focus on theories that are closely related to the works in this thesis, namely, the electrolyte non-ideality, electrical double layer, and field effect in weak electrolytes. We consider only symmetrical electrolytes, and assume spherical ions when the ion size is considered.

We start with the non-ideality of electrolytes given in Debye-Hückel theory and Bjerrum's pairing theory. The Poisson-Boltzmann equation is introduced in the derivation of Debye–Hückel theory and then used in the electrical double layer model, where we discuss the behaviour of ions near the electrolyte-metal interface.

In this thesis, it is of interest to estimate the electric field strength near electrode-electrolyte interface, which requires electrical double-layer theories. We overview the development of electrical double-layer models, from simple capacitor model to the Gouy-Chapman-Stern model. Then, we modify the Gouy-Chapman-Stern model, considering the impact of finite ion size and electric field dependence of water dielectric constant. This modified model is used in later chapters to help explain our experimental results. We finished this part by describing the calculation process of the modified model in a step-by-step manner.

In the last part of this chapter, we introduce the second Wien effect, which predicts that the large field can accelerate the dissociation of weak electrolytes. A linear approximation of the second Wien effect is firstly derived, showing that the free ion density in a weak electrolyte increases with the field strength. We then introduce Onsager's exact solution to the second Wien effect, and use Onsager's theory to predict the change of free ion density in the compact layer of the electrical double layer.

Contributions

My contributions to the work in this chapter include: partly authored the codes for the complete model (see Sec. 2.2.6.3). Calculated and plotted all the figures using the modified models (Sec. 2.2.6) and the analytical models (Sec. 2.2.2 and 2.2.3).

Collaborator's contribution: Mehmet Yagmurcukardes and Francois Peeters authored the core codes for solving the complete model described in Sec. 2.2.6.1 and 2.2.6.2.

2.1 Non-ideality and Debye-Hückel Theory

The Debye–Hückel theory explains the non-ideality of electrolytes by treating electrolytes as systems of charges [11]. The deviation from ideality in this sense comes from the electrostatic interaction between the charged ions. In theory, each ion in the electrolyte is surrounded by an average charge cloud constituted by other ions. The internal energy of the electrolyte system is reduced by the attractive interaction between the ion and its ionic cloud, which determines the mean ionic activity coefficient γ.

The activity coefficient a_i for any ion species, i, with concentration c_i is then given by [11]

$$a_i = \gamma_i \cdot c_i \tag{2.1}$$

The activity coefficient replaces concentration in many physical chemical equations, such as chemical equilibrium equation, cell potential, Nernst equation, etc. The mean activity coefficient then accounts for the non-ideal effects, and the ideal solution assumption is valid only in very diluted solutions, i.e., $\gamma_i \to 1$ when $c_i \to 0$.

For a spherical central ion surrounded by charges in the electrolyte, the potential ϕ of the central ion j is a function of the electrostatic interaction between the central ion and its surroundings. Thus, it is governed by the Poisson equation, which is expressed in spherical coordinates here as

$$\nabla^2 \phi_j(r) = -\frac{1}{\varepsilon_r \varepsilon_0} \rho(r) \tag{2.2}$$

where $\phi_j(r)$ is the total potential at a distance r from a central ion j, ε_r, the dielectric constant of the electrolyte, ε_0, the permittivity of vacuum, and ρ, the charge density (total charge per unit volume) around the centre ion.

The concentration n_i of ion specie i near a charged centre ion j at a distance r can be described by Boltzmann distribution

$$n_i(r) = n_i^0 \exp\left(\frac{-z_i e \phi_j(r)}{k_B T}\right) \tag{2.3}$$

where n_i^0 is the bulk concentration, z_i, the signed charge on the ion, e, the charge on an electron, ϕ_j, the electrostatic potential away from the centre ion j, k_B, the Boltzmann constant, and T, the absolute temperature.

The charge density ρ is a sum over all ion species, which is then given by

$$\rho(r) = \sum_i z_i e n_i(r) \tag{2.4}$$

combining Eq. 2.2-2.4, we have the Poisson-Boltzmann equation in spherical coordinates as

$$\nabla^2 \phi_j(r) = -\frac{1}{\varepsilon_r \varepsilon_0} \sum_i n_i^0 z_i \exp\left(\frac{-z_i e \phi_j(r)}{k_B T}\right) \tag{2.5}$$

For symmetrical electrolytes, expanding the right-hand side of Eq. 2.5 and keeping only the first non-zero term, yields

$$\nabla^2 \phi_j(r) = \phi_j(r) \frac{e^2}{\varepsilon_0 \varepsilon_r k_B T} \sum_i n_i z_i^2 \tag{2.6}$$

For solutions with only one symmetrical electrolyte (*z*:*z* electrolyte), which is known as the restrictive primitive model, the above equation is then reduced to

$$\nabla^2 \phi(r) = \frac{\phi(r)}{\ell_D} \tag{2.7}$$

and ℓ_D, the Debye length, is defined by

$$\ell_D = \sqrt{\frac{\varepsilon_0 \varepsilon_r k_B T}{2 n z^2 e^2}} \tag{2.8}$$

where z is the amount of electron charge carried by ions in the electrolyte, and n is the bulk concentration of the electrolyte. Equation 2.7 is a linear second-order differential equation. Hence, the solution to Eq. 2.7 is of the following form

$$\phi = A \cdot \frac{\exp(-r/\ell_D)}{r} \tag{2.9}$$

where A is a constant and we ignore the exponentially growing term as it is non-physical. We consider that the central ion has a finite diameter a within which the charge cloud could not form. Thus, Eq. 2.9 is only applicable to $r \geq a$. Given by point-charge Coulomb potential with an constant offset B, the potential inside the ionic sphere (for a positive centre ion) is

$$\phi(0 \leq r \leq a) = \frac{ze}{4\pi\varepsilon_0\varepsilon_r}\frac{1}{r} + B \tag{2.10}$$

Applying the potential and field continuity boundary conditions at the ionic surface a to Eq. 2.9 and 2.10 yields

$$\begin{aligned} A &= \frac{ze}{4\pi\varepsilon_0\varepsilon_r}\frac{\exp(a/\ell_D)}{1+a/\ell_D} \\ B &= -\frac{ze}{4\pi\varepsilon_0\varepsilon_r}\frac{1}{\ell_D + a} \end{aligned} \tag{2.11}$$

The value of B is the electrostatic potential induced by the interaction of a ion and its surrounding ionic atmosphere.

Equation 2.9 gives a screened potential of the selected central ion, with the Debye length ℓ_D as the screening length. The Debye length decreases with the square root of bulk ion density. Hence, the Debye–Hückel theory is only applicable to dilute electrolytes of which ℓ_D is considerably larger than the ion size. For concentrated electrolytes, the experimentally measured screen length ℓ_D increases with concentration, deviating largely from the prediction of Debye–Hückel theory [12]. Ion-size effects now play a role in the for the higher concentrations. Modifications in theory to address the ion-size effects will be discussed in Section 2.2.4 later.

Going back the the Debye–Hückel theory, let us image a virtual charging process of all ions ($n_+ = n_- = n$, $z_+ = z_- = z$) to the system. Hence, the deviation of the system's chemical potential from ideal solution is the extra electrostatic work during the charging process, which is given by

$$\Delta\psi = -\frac{z^2e^2}{8\pi\varepsilon_0\varepsilon_r}\frac{1}{\ell_D + a} \tag{2.12}$$

The additional factor of 2 is due to each ion pair being counted twice. Recall that $\Delta\Psi = -k_B T \ln(\gamma)$, accounting for the reduction of energy cost when adding a new charge to the system after the activity correction, we have the activity coefficient

$$\gamma = \exp\left(-\frac{\ell_T}{\ell_D + a}\right) \tag{2.13}$$

where

$$\ell_T = \frac{z^2 e^2}{8\pi\varepsilon_0\varepsilon_r k_B T} \tag{2.14}$$

is known as Bjerrum length. The Bjerrum length is introduced in Bjerrum's bounded pair theory [13]. It determines the boundary between the bounded and separated states of an ion pair. We consider an ion pair separated if the ions in the pair are of distance larger than ℓ_T, the Bjerrum length. The length ℓ_T helps to define weak and strong electrolytes. In strong electrolytes, $\ell_T < a$, the bounded state does not exist, and the electrolytes are fully ionised. If $\ell_T \gg a$, then this is the weak electrolyte regime, both bounded and separated states exist in the electrolyte. We will come to Bjerrum length again in Section 2.3, where the field dissociation of weak electrolyte will be introduced.

2.2 Electrical Double Layer

The double-layer structure is the ionic configuration near a charged surface such as an electrode under potential. When the surface of the electrode is charged, there are counter charges in the liquid. The charges in the liquid will concentrate near the interface and distribute throughout the liquid phase. Such a structure is known as electrical double layer. In the following, we introduce the theories developed to model the electrical double layer. The developments of electrical double layer theories are introduced in a historical setting, mainly following the derivation in [14]. We only cover the theories used later in this thesis to explain our experimental findings. Specifically, we are interested in predicting the electric field near a charged electrode in aqueous solutions. We refer to [15] for a more comprehensive review on electrical double layer and water near charged surfaces.

2.2.1 The Helmholtz Model

The Helmholtz model assumed that the charge separation at the phase interface results in two layer of charges [16, 17]. One layer is formed by the surface charges of the electrode under potential. The other layer consists of the counter charges which are ions that reside near the electrode surface in the liquid. Such a double-layer structure is essentially a parallel-plate capacitor, with two layers separated by a distance of x_2 defined by the radius of the counter ions.

The charge density σ at the electrode surface is given by

$$\sigma = \frac{\varepsilon_r \varepsilon_0}{x_2} V \tag{2.15}$$

where V is the voltage drop across x_2. The differential capacitance C_d is given by

$$C_d = \frac{\partial \sigma}{\partial V} = \frac{\varepsilon_r \varepsilon_0}{x_2} \tag{2.16}$$

The electric potential profile across the plate is linear, as given by

$$\phi = V(1 - \frac{x}{x_2}) \tag{2.17}$$

and the electric field strength is

$$E = \frac{V}{x_2} \tag{2.18}$$

The Helmholtz model assumes that the counter-ion layer is rigid and confined in a thin layer of thickness x_2, which is not the case in nature.

2.2.2 The Gouy-Chapman Model

Gouy and Chapman independently raised the idea of a diffuse layer of ions in solution [18, 19]. The ions are attracted/repelled by the electrostatic force from the interface potential, and at the same time, they diffuse to/from the bulk solution due to thermal kinetic motion. Thus, the concentration of excess charge in the diffuse layer would be determined by the balance between electrostatic force and thermal process. Since the electrostatic force is the largest near the interface, the concentration of the excess charge on the surface would be the highest. As the electrostatic force decays away from the electrode surface, the concentration of excess charge decreases to the bulk level.

The total charge distribution is governed by the Poisson-Boltzmann equation as introduced in Section 2.1. Here we consider a simple planar case, i.e., a plate electrode in an electrolyte. If we divide the solution into laminae of thickness dx, parallel to the electrode surface, the total charge per unit volume is then

$$\rho = -\varepsilon_r \varepsilon_0 \frac{d^2\phi}{dx^2} \tag{2.19}$$

Combining Eq. 2.3 to 2.19 yields the Poison-Boltzmann equation in planar case:

$$\frac{d^2\phi}{dx^2} = -\frac{e}{\varepsilon_r \varepsilon_0} \sum_i n_i^0 z_i \exp\left(\frac{-z_i e \phi}{k_B T}\right) \tag{2.20}$$

After simplification and integration, we can relate electrostatic potential with distance by

$$\left(\frac{d\phi}{dx}\right)^2 = \frac{2k_B T}{\varepsilon_r \varepsilon_0} \sum_i n_i^0 \left[\exp\left(\frac{-z_i e \phi}{k_B T}\right) - 1\right] \tag{2.21}$$

With the limitation in systems that have only one symmetrical electrolyte, such as

H_2O and KOH, Eq. 2.21 can be rewritten to

$$\frac{d\phi}{dx} = -\left(\frac{8k_BTn^0}{\varepsilon_r\varepsilon_0}\right)^{1/2}\sinh\left(\frac{ze\phi}{2k_BT}\right) \tag{2.22}$$

Integrating Eq. 2.22 yields

$$\frac{\tanh(ze\phi/4k_BT)}{\tanh(ze\phi_0/4k_BT)} = \exp(-\kappa x) \tag{2.23}$$

where ϕ_0 is the potential at $x = 0$ relative to the bulk solution, and

$$\kappa = \left(\frac{2n^0z^2e^2}{\varepsilon_r\varepsilon_0k_BT}\right)^{1/2} = \frac{1}{\ell_D} \tag{2.24}$$

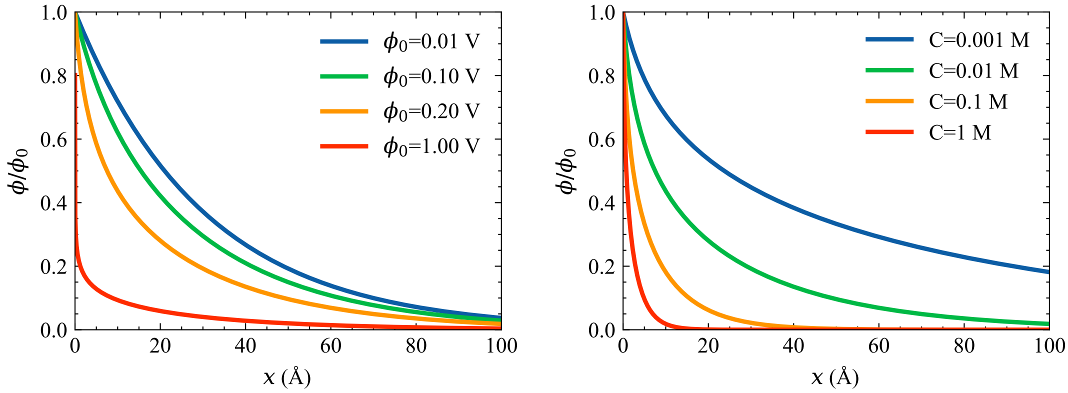

(a) (b)

Figure 2.1: Potential profiles across the diffuse layer. (a) Potential profile as a function of electrode potential with concentration $C = 10^{-2}$ M, i.e. ℓ_D = 30.4 Å. (b) Potential profiles as a function of concentration with electrode potential ϕ_0 = 0.2 V. Other parameters: diluted aqueous electrolytes ($\varepsilon = 78.49$), Z = 1, T = 298.15 K.

The parameter κ has a unit of m^{-1} and note that $\ell_D = 1/\kappa$, which is the Debye length. The ℓ_D here can be regarded as a characteristic thickness of the diffuse layer since it determines (partially) the spatial decay of potential. Nevertheless, one should also note that ℓ_D is not the actual thickness of the diffuse layer because the electrode potential also affects the diffuse layer thickness, as can be seen in Fig. 2.1a. The κ explains the concentration dependency of the defuse layer. The higher the concentration of the electrolyte, the denser the defuse layer (Fig. 2.1b).

Figure 2.1 shows the calculated potential profile through the diffuse layer. Increasing the electrolyte concentration has a similar effect on the potential profile — shrinking the thickness of diffuse layer. When ϕ_0 is sufficiently low, $\tanh(ze\phi/4k_BT) \approx ze\phi/4k_BT$, then the potential profile decays exponentially, $\phi/\phi_0 = e^{-\kappa x}$. If ϕ_0 is large, the potential profile will decay even faster than exponentially. And inevitably, the local electrical field strength near the surface of the electrode would explode to infinity. Such a trend is clear in the ϕ_0 = 1 V curve in Fig. 2.1a, as the sharp potential profile becomes almost indistinguishable from the vertical axis.

By treating the ions as point charges, the ions can approach the electrode surface arbitrarily close. This is not realistic because ions have finite size, and some have hydrate shells.

2.2.3 The Gouy-Chapman-Stern Model

Stern modified the Gouy-Chapman model by introducing the limitation that ions do have size. As a result, the ions can only approach the electrode surface at some distance x_2 [20]. The radius of the ions determines the distance x_2. Other factors such as electrode surface adsorption may also add to the distance [9]. The plane at $x = x_2$ is known as the outer Helmholtz plane (OHP) or the Stern plane.

The Gouy-Chapman-Stern (GCS) model suggests that the Poisson-Boltzmann equation Eq. 2.20 and its solution still apply at $x > x_2$. Thus, the electrical double layers is divided into two parts, the Stern layer ($0 < x <= x_2$) and the diffuse layer ($x > x_2$). For symmetrical electrolytes, now the potential profile in the diffuse layer is given by

$$\frac{\tanh(ze\phi/4k_BT)}{\tanh(ze\phi_2/4k_BT)} = e^{-\kappa(x-x_2)} \tag{2.25}$$

where ϕ_2 is the electrostatic potential at the OHP ($x = x_2$). The electric field $E = -\frac{d\phi}{dx}$ at the OHP is determined by

$$\left(\frac{d\phi}{dx}\right)_{x=x_2} = -\left(\frac{8k_BTn^0}{\varepsilon_r\varepsilon_0}\right)^{1/2} \sinh\left(\frac{ze\phi_2}{2k_BT}\right) \tag{2.26}$$

Since there are no ions between the electrode surface and the OHP, this region is essentially a parallel-plate capacitor. Thus, the electrical field in this region is constant and equal to the electrical field at the OHP.

$$\left(\frac{d\phi}{dx}\right)_{0\leq x\leq x_2} = \frac{\phi_2-\phi_0}{x_2} = \left(\frac{d\phi}{dx}\right)_{x=x_2} \tag{2.27}$$

where ϕ_2 is potential at OHP.

The electrostatic potential across the Stern layer is linear, as given by

$$\phi = \phi_0 + x\left(\frac{d\phi}{dx}\right)_{x=x_2} \tag{2.28}$$

With a known ϕ_2, it is easy to determine ϕ_0 from Eq. 2.26 and 2.27. But going from ϕ_0 to ϕ_2, Eq. 2.26 and 2.27 have to be numerically solved.

Equations 2.26 and 2.28 yield the potential profile of the Gouy-Chapman-Stern (GCS) model. An example calculation is depicted in Fig. 2.2a. To matched our experimental conditions, we used parameters for 0.01 M potassium chloride (KCl) solutions, and the electrode is negatively charged. Hence, the Stern layer thickness is assumed equal to the hydrated potassium ion radius, $x_2 = 3.3\text{Å}$.

The GCS model explains the electric potential distribution near an electrode. We

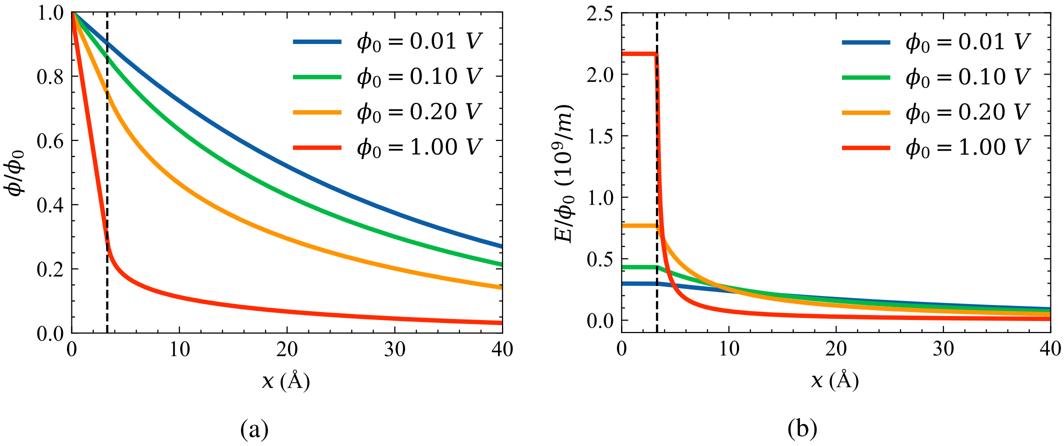

(a) (b)

Figure 2.2: Potential and electric field profiles in the Gouy-Chapman-Stern double layer. Parameters: $\varepsilon_r = 78.49$ for diluted aqueous electrolytes, concentration $C = 10^{-2}$ M, Z = 1, T = 298.15 K, ℓ_D = 30.4 Å, and x_2 = 3.3 Å (K^+ hydration radius).

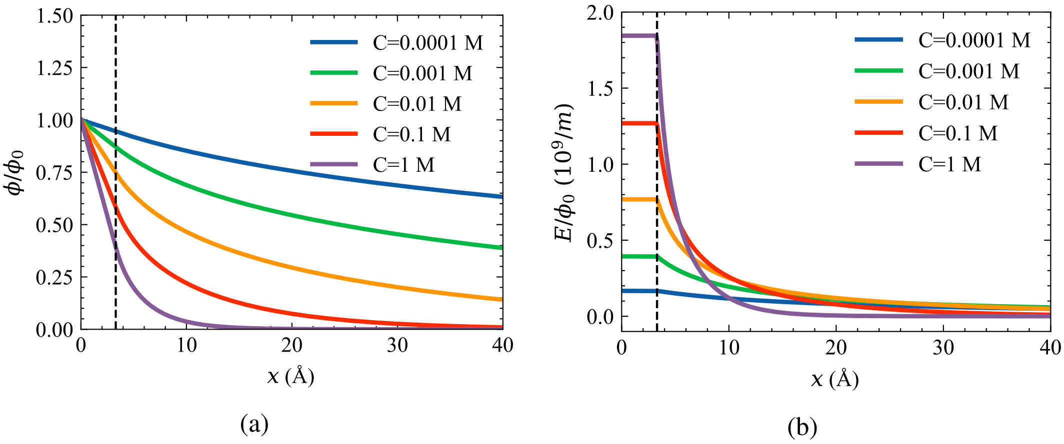

(a) (b)

Figure 2.3: Concentration dependency of potential and electric field profiles in the Gouy-Chapman-Stern double layer. Parameters: $\varepsilon_r = 78.49$ for diluted aqueous electrolytes, electrode potential ϕ_0 = 0.2 V, Z = 1, T = 298.15 K, ℓ_D = 30.4 Å, and x_2 = 3.3 Å (K^+ hydration radius).

could estimate that the electric field near the electrode can be as large as in the order of 10^9 V/m (Fig. 2.2b), with ~ 1 V potential drop across a Helmholtz layer of thickness 3.3 Å.

It should be noted that the field continuity assumption (Eq. 2.27) is another simplification of the GCS model. Stern model does not consider the fine structure of the compact layer. In an aqueous solution, owing to the polarised nature of water molecules, the relative dielectric constant of the electrolyte in an intensive electric field is lower than its bulk value [21–23]. Hence, the dielectric constants in the Stern and diffuse layer should be different, which violates the continuity assumption.

Apart from the discrete dielectric constant and dielectric dependency on the electric field, other matters such as the compression of compact layer under high electric field are not considered in Stern model [9].

The Stern model introduced here provides a concise picture of the electrical double layer. However, some modifications are needed for the Stern model to support the explanation of our experimental observation in this thesis. We will address these in the rest of this section.

2.2.4 Finite Ion-size Modification in Diffuse Layer

Recall that when we introduce the GCS model, the finite ion size contributes to a compact layer of counter ions situated at the distance $x = x_2$ away from the electrode. However, the ions in the diffuse layer still behave like points charges. This simplification leads to a deviation from reality when the electrode is biased at high potential or in contact with high concentration electrolytes [24].

Here we introduce the Bikerman model, which is a modification of the GCS model that considers the finite size of ions in the diffuse layer [24].

For the diffuse layer in a 1:1 symmetric electrolyte, Eq. 2.20 can be simplified to

$$\frac{d^2\phi}{dx^2} = \frac{k_B T}{e\ell_D^2} \sinh\left(\frac{e\phi}{k_B T}\right) \tag{2.29}$$

The Bikerman model multiplies a correction term $f_C(\phi)$ to the right hand side of Eq. 2.29, which yields the differential equation proposed in [25]

$$\frac{d^2\phi}{dx^2} = \frac{k_B T}{e\ell_D^2} f_C(\phi) \sinh\left(\frac{e\phi}{k_B T}\right) \tag{2.30}$$

where

$$f_C(\phi) = \frac{1}{1 + 2\nu \sinh^2\left(\frac{e\phi}{2k_B T}\right)} \tag{2.31}$$

In the above equation, the parameter $\nu = 2C/C_{\max}$ with $C_{\max} = (a^3 N_A)^{-1}$, a is the ionic diameter of K^+, N_A is the Avogadro number, and C is the bulk concentration of electrolyte. As $C \to 0$, $f_C(\phi) \to 1$, the Bikerman model approaches to the GCS model (Eq. 2.29). Equation 2.30 is numerically solved in this thesis to calculate electric fields for concentration and electrode potential experimentally obtained.

2.2.5 Field-Dependent Dielectric Constant of Water

As shown in the above theoretical calculation, the electric fields in the Stern layer are typically in GV/m level. This strongly affects both the physical and chemical properties of liquid water near the electrode/liquid interface. We will introduce the fact that E-field increase water's dissociation rate in the next section. Here, to introduce the last modification to the electric double layer model used in this thesis, we note that the strong E-field also change water's behaviours as a dielectric medium [21, 22]. The polarisability and dielectric constant of interfacial water are determined by the orientation and arrangement of local water structures, which has been verified by several experiments addressing from optical [21, 23] and electrical [26] approaches.

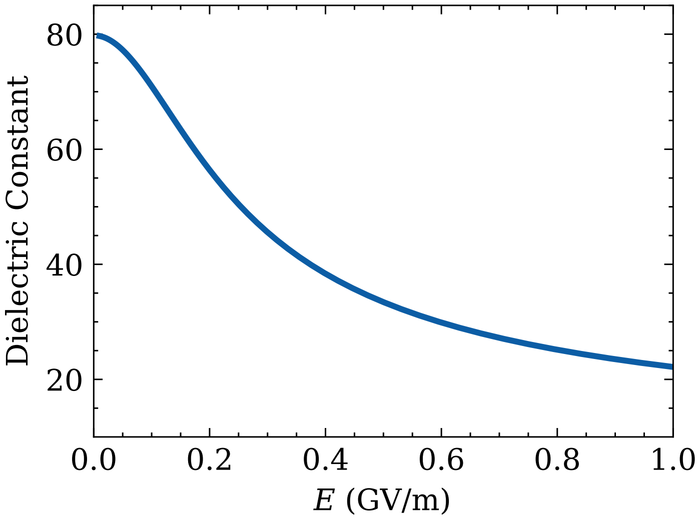

Figure 2.4: Dielectric constant as a function of electric field strength. This is calculated by Eq. 2.32.

We model the field-dependent dielectric constant using an empirical modification of the Kirkwood equation [27], similar to that used in ref. [22].

$$\varepsilon_r = \beta\nu^2 + \frac{28\pi(\beta\nu^2+2)(\alpha N_{\mathrm{water}})(\gamma\mu)}{2\sqrt{73}E}\mathrm{L}\left[\frac{\sqrt{73}(\delta E)(\beta\nu^2+2)(\gamma\mu)}{6k_BT}\right] \tag{2.32}$$

where ν is the optical reflex index of bulk water (ν = 1.33) at room temperature, $\mu = 1.97$ D is the dipole moment, N_{water} is the number density of water molecules in the Stern layer, and $\mathrm{L}(x) = \coth(x) - 1/x$ is the Langevin function. The equation contains four fitting parameters, α, β, γ, and δ, each scaling the water density, the refractive index, the dipole moment of water, and the electric field in Stern layer, respectively. This account for the differences of water in the Stern layer from the bulk water. The values for these parameters used in this thesis are $\alpha = 1.672$, $\beta = 0.96$, $\gamma = 0.338$, and $\delta = 5.317$, taken from [25].

To adopt the field-dependence of dielectric constant in the electric double layer model, we followed the manners in [22]. Firstly, we consider the dielectric constant as a function of field strength $\varepsilon_r(E)$ only in the Stern layer. Thus, the Bikerman model Eq. 2.30 is still applicable in the diffuse layer. This is a reasonable assumption, because the field strength in the diffuse layer is relatively small (Fig. 2.2b), and the dielectric constant is practically the bulk value (~ 78, as in Fig. 2.4).

Then, the field strength and corresponding dielectric constant have to satisfy the following equation governing the compact layer.

$$E = \frac{\sigma}{\varepsilon_0 \varepsilon_r(E)} \tag{2.33}$$

where σ is the charge density near the interface. The surface charge density can be determined from the Poisson equation once the Bikerman model (Eq. 2.30) is solved in the diffuse layer. The electric field in the Stern layer has to satisfy Eq. 2.33, which in turn determines the dielectric constant of the Stern layer via Eq. 2.32.

2.2.6 The Complete Model

With the two modifications added to the initial GCS model, we now introduce the calculation details of the complete model, which will be used to explain our results in the Chapter 6.

2.2.6.1 Calculation in the Diffuse Layer

The first step is to solve the Bikerman model (finite ion size modification) for the diffuse layer for $x \geq x_2$. Following the same manner as in Section 2.2.2 and in [9], we simplify Eq. 2.30 by noting that

$$\frac{d^2\phi}{dx^2} = \frac{1}{2}\frac{d}{d\phi}\left(\frac{d\phi}{dx}\right)^2 \tag{2.34}$$

hence,

$$d\left(\frac{d\phi}{dx}\right)^2 = \frac{2k_BT}{e\ell_D^2} f_C(\phi) \sinh\left(\frac{e\phi}{k_BT}\right) d\phi \tag{2.35}$$

Integrating both parts gives

$$\frac{d\phi}{dx} = -\frac{k_BT}{e\ell_D}\sqrt{\frac{2}{\nu}\ln\left[\sinh\left(\frac{e\phi}{k_BT}\right)\right]} \tag{2.36}$$

To solve Eq. 2.36 in diffuse layer, we use boundary condition $\phi_{x=x_2} = \phi_2$, and numerically integrate the differential equation using the MATLAB ODE Suite (ode45, Runge-Kutta formula) [28, 29]. This allows calculation of potential profile $\phi_{x\geq x_2}$ across the diffuse layer for a given potential at OHP, ϕ_2, and ion concentration, C.

Noting that

$$E = -\frac{d\phi}{dx}, \tag{2.37}$$

hence, the electric field profile in the diffuse layer, $E_{x\geq x_2}$, can be calculated by plugging $\phi_{x\geq x_2}$ back into Eq. 2.36.

2.2.6.2 Calculation in the Stern Layer

In the complete model, the Stern layer is treated as a capacitor with field-dependent capacitance ($C_d = \varepsilon_0\varepsilon_r(E)/x_2$), i.e., the $\varepsilon_r(E)$ modification. The charge density per unit area σ on the electrode is determined by the charges distributed in the diffuse layer. From [9], σ is given by

$$\sigma = -\varepsilon_0\varepsilon_r\left(\frac{d\phi}{dx}\right)_{x=x_2} = \varepsilon_0\varepsilon_r E_2 \tag{2.38}$$

, which can be calculated by plugging ϕ_2 into Eq. 2.36.

The electric field in the Stern layer, E_0, can be calculated by numerically solving Eq. 2.33, using standard root-finding techniques (such as fsolve in MATLAB). Once

E_0 is calculated, the potential profile across the Stern layer is linear, as given by

$$\phi(0 \leq x < x_2) = \phi_2 + E_0(x_2 - x) \tag{2.39}$$

Hence, the potential at the electrode

$$\phi_0 = \phi_2 + E_0 x_2 \tag{2.40}$$

It should be pointed out that Eq. 2.28 introduced in GCS model no longer stands in the modified model, since $E_0 \neq E_2$. This is a result of the discrete dielectric constant from Stern layer to the diffuse layer.

2.2.6.3 Connecting Model with Experiment

With the above two steps, we now have the method to calculate ϕ and E for any distance from the electrode, with a given ϕ_2 and concentration. However, in the experimental work of this thesis, the potential across the electrode-electrolyte interface is applied externally (see Sec. 5.2.1). This leads to a good estimation of electrode potential ϕ_0, but not ϕ_2, the potential a few angstroms from the electrode surface.

Nevertheless, it is possible to calculate ϕ and E using the complete model with ϕ_0 instead of ϕ_2. To show this clearer, we express E_0 in Eq. 2.40 as $E_0(\phi_2)$, a function of ϕ_2 , and get the following equation

$$\phi_0 = \phi_2 + x_2 \cdot E_0(\phi_2) \tag{2.41}$$

The next step is to find a ϕ_2 that satisfies Eq. 2.41, which again can be solved using standard root-finding techniques. Note that the physically meaningful root of Eq. 2.41 must sit between 0 and ϕ_0. Knowing this could accelerate the calculation of ϕ_2.

2.2.6.4 Calculation Results

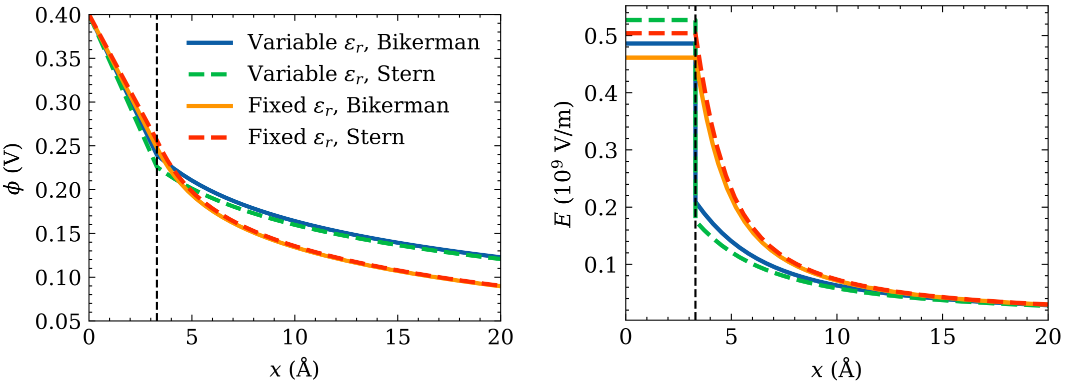

(a) (b)

Figure 2.5: Potential and electric field profiles calculated using the modified double-layer models. (a) Potential profiles, and (b) electric field profiles, calculated with/without Bikerman's finite ion size modification, and with and without field-dependent ε_r in Stern layer. Parameters: fixed $\varepsilon_r = 78.49$, electrode potential $\phi_0 = 0.4$ V, $Z = 1$, $T = 298.15$ K, $C = 1$ mM, and $x_2 = 3.3$ Å.

As an example, we show the potential and electric field profiles calculated by the modified models (including the complete model), and compare them with the original GCS model. Figure 2.5 displays the calculation results from four models: GCS model, Bikerman model (i.e. with finite-ion-size modification), GCS model with variable ε_r, and Bikerman model with variable ε_r. Figure 2.6 summarises the concentration and electrode-potential dependencies of the electric field strength in the Stern layer. The Bikerman model with variable ε_r is the complete model we used in the later chapters to interpret our experimental results.

2.3 Second Wien Effect

An electrical field pushes electrolytes away from equilibrium [10, 30], Max Wien discovered firstly that the conductivity of strong electrolytes increases in the presence of an electrical field (normal Wien effect) [30]. Moreover, it is found that the dissociation

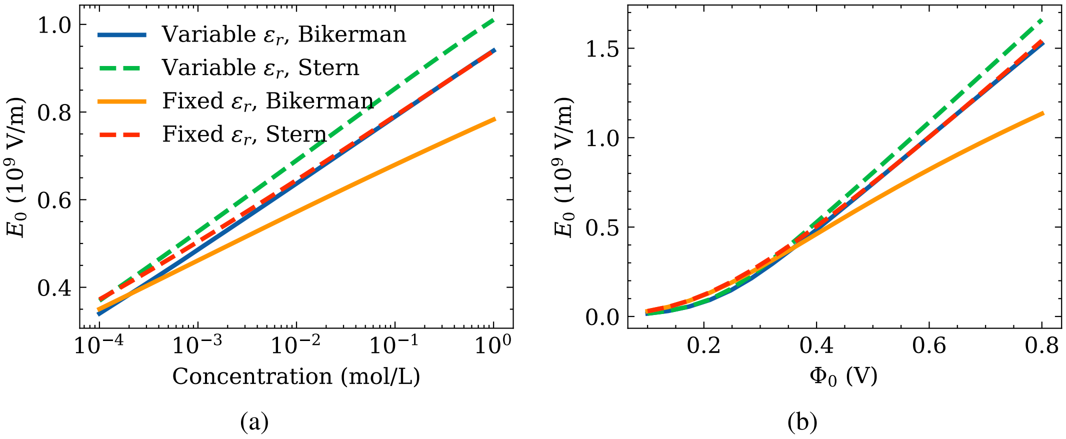

(a) (b)

Figure 2.6: Electric field strength in Stern layer as functions of concentration and electrode potential. (a) Concentration dependency, with electrode potential $V = 0.4$ V. (b) Potential dependency, with concentration $C = 1$ mM. Parameters: fixed $\varepsilon_r = 78.49$, $Z = 1$, $T = 298.15$ K, and $x_2 = 3.3$ Å.

of bound pairs in weak electrolytes is enhanced under a large external field, giving rise to the conductivity [7, 8, 30]. The latter is known as the second Wien effect, which we will refer to as the Wien effect in the rest of this thesis.

2.3.1 The Linear Law

In the following, we will describe a simple approximation to achieve a linear relationship between the dissociation with electric field strength. Without losing generality, we will limit the expression to 1:1 symmetrical electrolytes, which is also suitable for our interests in water dissociation under the electric field. Here we follow the derivation presented in [31].

The bound pairs in a weak electrolyte are neutral chemical species in equilibrium with their free-ion forms. This can be expressed by the following dissociation reaction

$$< +, - > \longleftrightarrow < + > + < - > \tag{2.42}$$

An ion pair $< +, - >$ is bounded by the Coulombic interaction, the energy of which

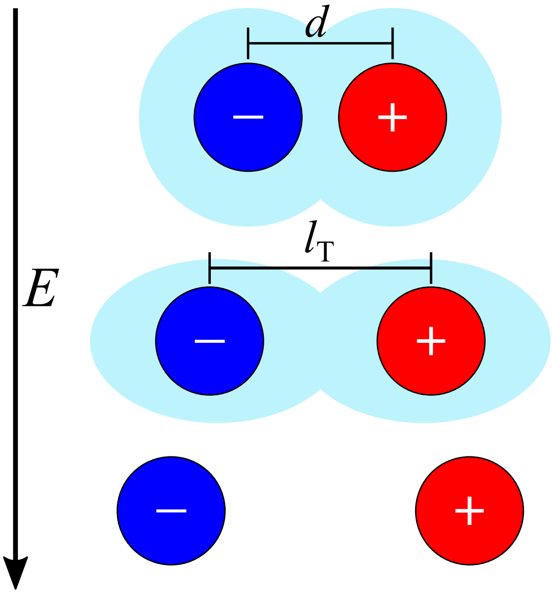

Figure 2.7: Diagram of the second Wien effect.

is given by its Coulombic potential energy

$$U_C(d) = -\frac{e^2}{4\pi\varepsilon_0\varepsilon_r d} \tag{2.43}$$

where d is the distance between the two ions ($<+>$ and $<->$). The pair is considered bounded if its thermal energy is less than half of its Coulombic potential energy. This defines a length parameter known as Bjerrum length ℓ_T at which the potential energy is $U_C(\ell_T) = -2k_BT$. In this case, the Bjerrum length is

$$\ell_T = \frac{e^2}{8\pi\varepsilon_0\varepsilon_r k_B T} \tag{2.44}$$

which has the same form as Eq. 2.14. The Bjerrum length ℓ_T is the minimum point of the probability of finding an ion pair that are separated by d. Thus the Bjerrum length determines the intermediate stage between the bounded pair and free ions (see Fig. 2.7).

The rate of the dissociation reaction is determined by the dissociation equilibrium constant K_D. The constant K_D is given by the Gibbs energy ΔG, which is the potential energy barrier corresponding to ion pairs that are separated by a distance of Bjerrum length ℓ_T. Hence we have

$$K_D = \exp\left(-\frac{\Delta G}{k_B T}\right) \tag{2.45}$$

The bound state of an ion pair can be modelled as a dipole. Under an electric field E, the dipole aligns with the field. As the field strength increases, the dipole stretches to the size of Bjerrum length and becomes easier to dissociate. In this process, the change of Gibbs energy $\Delta G(E) - \Delta G(0)$ is equal to the electric work done on the dipole, which is given by

$$\Delta G(E) - \Delta G(0) = -eE\ell_T \tag{2.46}$$

This results in the change of the dissociation constant:

$$\frac{K_D(E)}{K_D(0)} = \exp\left(\frac{eE\ell_T}{k_B T}\right) \tag{2.47}$$

In a reversible chemical reaction, the equilibrium constant is related to the concentration of each side of the reaction equation. For the dissociation reaction, let us note n_b the concentration of ions in bound pairs, and n_f the concentration of free ions. Then, n_f is twice the concentration of ions in opposite sign,respectively, i.e. $n_f = 2n_f^- = 2n_f^+$. Hence the equilibrium constant K_D is given by

$$K_D = \frac{n_f^- n_f^+}{n_b/2} = \frac{n_f^2}{2n_b} \tag{2.48}$$

With assumption that $n_f + n_b = 1$ and $n_f \ll 1$, the concentration of free ions can be calculated from the dissociation constant K_D by

$$n_f = \sqrt{2K_D} \tag{2.49}$$

The shift of dissociation equilibrium induced by electrical field results in an increase of free ion density. Plugging Eq. 2.49 into Eq. 2.47 yields

$$\frac{n_f(E)}{n_f(0)} = \sqrt{\frac{K_D(E)}{K_D(0)}} \approx 1 + \frac{1}{2}\frac{eE\ell_T}{k_BT} \tag{2.50}$$

This shows that, to a first-order approximation, the free ion density increase linearly with electric field. As the carrier density increases, the conductivity of the electrolyte increases.

The linear law clarifies the nature of the second Wien effect, although it is over-simplified. A more advanced theory involves solving the drift-diffusion equation of charges, a solution of which is given by Onsager [8]. Other approaches include numerical simulation using the Monte Carlo algorithm and molecular dynamics simulation [7].

2.3.2 Onsager's Theory

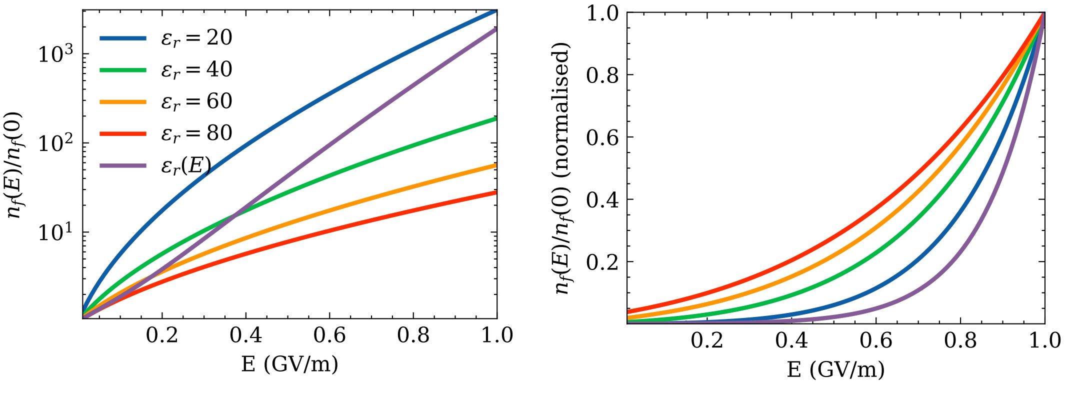

(a) (b)

Figure 2.8: Increase of free ion density $n_f(E)/n_f(0)$ as a function of electric field strength. Calculated by Onsager's theory with T = 298.15 K, and (a) in log scale, (b) normalised by values at $E = 1\ \mathrm{GV \cdot m^{-1}}$.

In Onsager's 1934 paper [8] he shows that the change in dissociation equilibrium constant of 1:1 weak electrolytes can be expressed as an explicit function of electric field in the following form.

$$\frac{K_D(E)}{K_D(0)} = F(x) = \frac{I_1\left(\sqrt{8x}\right)}{\sqrt{2x}} = 1 + x + \frac{1}{3}x^2 + O\left(x^3\right) \tag{2.51}$$

where F is the Onsager function, I_1 is the modified Bessel function, and the parameter $x = \ell_T/\ell_E$ which is a ratio between the Bjerrum length ℓ_T and the field length $\ell_E = k_B T/eE$. The change of free ion density is given by

$$\frac{n_f(E)}{n_f(0)} = \sqrt{F(x)} = \left(\frac{I_1\left(\sqrt{8x}\right)}{\sqrt{2x}}\right)^{\frac{1}{2}} = 1 + \frac{x}{2} + \frac{x^2}{24} + O(x^3) \tag{2.52}$$

At low electric field strength, Eq. 2.52 reduces to the linear form in Eq. 2.50. The response of ion density to small electric fields is notably large. Even more, the Onsager function F grows exponentially in a large electric field as given by

$$F(x) = \left(\frac{2}{\pi}\right)^{\frac{1}{2}} (8x)^{-\frac{3}{4}} \exp\left(\sqrt{8x}\right)\left(1 - \frac{3}{8\sqrt{8x}} + O\left(\frac{1}{x}\right)\right) \tag{2.53}$$

The field dependency of free ion density increase $n_f(E)/n_f(0)$ is shown in Fig. 2.8, as predicted by Onsager's theory. The function is calculated for several dielectric constant values.

In Onsager's theory, the dielectric constant was not dependent on electric field strength, which is enough for systems with low E-field and non-polar solvents [8]. However, as described in Section 2.2, the electric field in the Stern layer is at GV level. Hence the decreases of the dielectric constant of water under such an intense field can not be neglected. Here we introduce the field-dependent dielectric constant into Onsager's theory by plugging the dielectric constant function Eq. 2.32 into Eq. 2.44, which yields a field-dependant Bjerrum length.

$$\ell_T(E) = \frac{e^2}{8\pi\varepsilon_0\varepsilon_r(E)k_BT} \tag{2.54}$$

This equation and Eq. 2.51 are used in this thesis to model the field-dependent dissociation constant. As shown in Fig. 2.8, the Onsager function with variable dielectric constant converges with the $\varepsilon_r = 80$ branch in the low-field range and approaches the $\varepsilon_r = 20$ branch in the high-field range.

Chapter 3

Water Electrolysis and Electric Field Effect

In this chapter, we firstly introduce some fundamentals of water electrolysis. Then we give a review on the electrolysis current density achieved in the state-of-the-art water electrolysers. Followed by this, we overview the theoretical and experimental investigations of the electric field effect in water dissociation.

3.1 Water dissociation and electrolysis

Electrochemical water splitting, or water electrolysis, is a reaction in which electricity is consumed to split water into oxygen and hydrogen gas. The overall reaction of water electrolysis is described by

$$\mathrm{H_2O\,(l)} \xrightarrow{\text{Electricity}} \mathrm{H_2\,(g)} + \frac{1}{2}\mathrm{O_2\,(g)} \tag{3.1}$$

First observed in 1789 [32], water electrolysis is one of the earliest experiments in electrochemistry. The reaction is typically performed in an electrolysis cell, with two inert electrodes (anode and cathode) immersed in electrolyte solution, as shown in the schematics in Fig. 3.1. Catalyst metal materials such as platinum can be used as electrodes for water electrolysis.

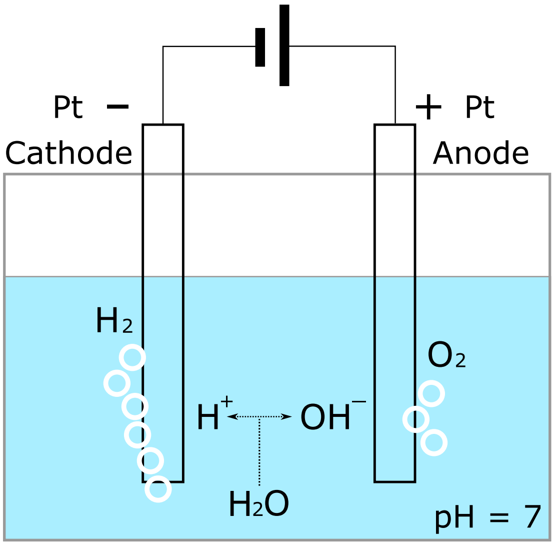

Figure 3.1: Illustration of a water electrolysis cell. Two platinum electrodes are immersed in pure water (pH=7). External voltage bias is applied between the two electrodes. Hydrogen gases evolve from the cathode, the electrode connected with low-potential end of the voltage source. Oxygen gases evolve from the anode.

The overall electrolysis occurs in a few intermediate steps and consists of two half-cell reactions. The first step is water dissociation, water molecules dissociate into proton and hydroxide ions:

$$\mathrm{H_2O\,(l)} \rightleftharpoons \mathrm{H^+\,(aq)} + \mathrm{OH^-\,(aq)} \tag{3.2}$$

With an electric voltage bias applied to the two electrodes, protons migrate to the cathode (negative electrode) and hydroxide ions to the anode (positive electrode). On the cathode, protons receive electrons and evolve into hydrogen gas via the reaction:

$$2\,\mathrm{H^+\,(aq)} + 2\,\mathrm{e^-} \rightleftharpoons \mathrm{H_2\,(g)} \tag{3.3}$$

On the anode, oxygen evolves from hydroxide ions via the reaction given by

$$2\,\mathrm{OH^-}\,(\mathrm{aq}) - 2\,\mathrm{e^-} \rightleftharpoons \frac{1}{2}\mathrm{O_2}\,(\mathrm{g}) + \mathrm{H_2O}\,(\mathrm{l}) \tag{3.4}$$

These two reactions are known as the hydrogen evolution reaction (HER) and oxygen evolution reaction (OER). The exact reactions on each electrode change depending on the pH of the electrolyte. as summarised below.

In acidic and neutral electrolytes:

$$\begin{aligned} &\text{HER (Cathode):} \quad 2\,\mathrm{H^+}\,(\mathrm{aq}) + 2\,\mathrm{e^-} \rightleftharpoons \mathrm{H_2}\,(\mathrm{g}) \\ &\text{OER (Anode):} \quad \mathrm{H_2O}\,(\mathrm{l}) - 2\,\mathrm{e^-} \rightleftharpoons \frac{1}{2}\mathrm{O_2}\,(\mathrm{g}) + 2\,\mathrm{H^+}\,(\mathrm{aq}) \end{aligned} \tag{3.5}$$

In alkaline condition:

$$\begin{aligned} &\text{HER (Cathode):} \quad 2\,\mathrm{H_2O}\,(\mathrm{l}) + 2\,\mathrm{e^-} \rightleftharpoons \mathrm{H_2}\,(\mathrm{g}) + 2\,\mathrm{OH^-}\,(\mathrm{aq}) \\ &\text{OER (Anode):} \quad 2\,\mathrm{OH^-}\,(\mathrm{aq}) - 2\,\mathrm{e^-} \rightleftharpoons \frac{1}{2}\mathrm{O_2}\,(\mathrm{g}) + \mathrm{H_2O}\,(\mathrm{l}) \end{aligned} \tag{3.6}$$

3.1.1 Thermodynamics

Thermodynamically, the electrode potential (E) of the anode and cathode is pH dependant. The Nernst potential for the two electrode reactions with respect to the normal hydrogen electrode (NHE) is related to proton and hydroxide activity, respectively, as given by

$$\begin{aligned} E_{\mathrm{HER}} &= E^0_{\mathrm{H_2/H^+}} - \frac{RT}{F}\ln\left(a_{\mathrm{H^+}}/P^{1/2}_{\mathrm{H_2}}\right) \\ &= 0.000 - 0.059 \times \mathrm{pH\ V\ vs\ NHE} \\ E_{\mathrm{OER}} &= E^0_{\mathrm{O_2/H_2O}} + \frac{RT}{F}\ln\left(1/a_{\mathrm{H^+}}P^{1/2}_{\mathrm{O_2}}\right) \\ &= 1.229 - 0.059 \times \mathrm{pH\ V\ vs\ NHE} \end{aligned} \tag{3.7}$$

where E^0 is the electrode potential at standard condition (25 °C, 1 bar pressure.), R the universal gas constant, T temperature, F Faraday constant, and P pressure. Different signs before the Nernst term accounts for the charge transfer direction (reduction and oxidation.) Figure 3.2 shows the Nernst potential of HER and OER as a function of electrolyte pH.

The difference between E_{cathode} and E_{anode} is know as the cell potential Δ_{cell}, given by

$$\Delta_{\text{cell}} = E_{\text{anode}} - E_{\text{cathode}} \tag{3.8}$$

Δ_{cell} corresponds to the open-circuit voltage of a hydrogen fuel cell, which is a reverse of the water electrolysis cell. The cell potential is always 1.229 V (grey arrow in Fig. 3.2) if the electrolyte is kept at the same pH. This is indeed the thermodynamic potential for water splitting. The electrode potential E is the thermodynamic equilibrium potential at which the electrode reaction starts to happen. In an electrolysis cell, the electrode potential is controlled by an external energy source. For HER to happen, electrode potential (E) has to be lower than E_{HER}, for OER, $E > E_{\text{OER}}$. As a result, the external voltage bias has to be larger than Δ_{cell} to start water electrolysis.

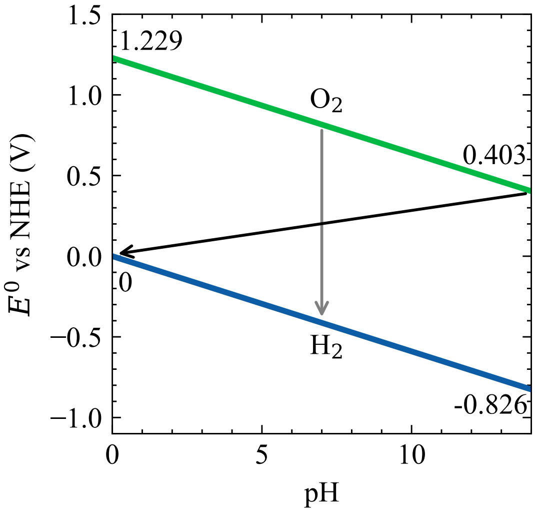

Figure 3.2: Nernst potential (E versus NHE) of the O_2 and H_2 evolution reaction as a function of pH.

As displayed in Fig. 3.2, the OER potential decreases as pH increases, requiring lower oxidative potential, which indicates that OER is favoured in alkaline conditions. On the contrary, HER required higher reductive potential as pH increases due to lower proton activity. If the cathode and anode are placed in alkaline and acidic conditions to promote OER and HER, respectively, the cell potential Δ_{cell} becomes less than 1.229 V.

The earliest work using a pH gradient can be traced back to Teschke *et al.*, in which a homogeneous ion-exchanging membrane was used to separate the two electrodes but keeping the ionic connection of the electrolyte [33]. Such reduction in cell voltage is clearly not under thermodynamic equilibrium, and extra care must be taken to maintain the pH gradient. Recent research introduced bipolar membrane to maintain the pH gradient [34]. This membrane prevents the proton and hydroxide cross-over and allows water molecules to dissociate in the bipolar interface. Further information on ion-exchanging membranes will be introduced later in the next section.

The cell potential with electrode pH difference (ΔpH) is given by

$$\Delta_{\text{cell}} = 1.229 - 0.059 \times \Delta\text{pH}, \tag{3.9}$$

which shows that the applied voltage in the cell can be made as small as 0.4 V in theory (black arrow in Fig. 3.2).

In practical electrolysis systems, more energy is needed to overcome excess barriers contributed by factors such as electrolyte resistance, electrode activation energy, and surface charged depletion. Thus the actually potential required to initiate the electrolysis is higher than the thermodynamic prediction (including those using pH gradient) This excess potential is known as overpotential (η).

3.1.2 Catalysts for water electrolysis

Catalysts are typically used to accelerate the rate of reaction in both half reactions of water electrolysis. For high-current-density electrolysis, the best catalyst for HER is Pt, and IrO_2 for OER. Pt and Ir both are scarce metals [35, 36]. In this thesis, platinum nanoparticles are used as an HER catalyst material on the micro-sized graphene electrode. For OER, Pt wires or Pt-decorated carbon electrodes are used. Although Pt is not the best catalytic material for OER [37], the OER is not the bottleneck of our micro electrolysis cell, because of the large effective area of the OER electrode compared with the graphene electrode (see Section 5.1). Let us go through some information about platinum's HER catalytic properties.

Three chemical processes are generally adopted to describe HER catalysis occurs at various metals (such as Pt), note as M [38]. The ion species involved in the processes vary from different pH conditions. Here we focus on acidic and neutral conditions, as it is most close to the case in this thesis. The first step is a Volmer process, which involves charge transfer to proton and the generation of intermediate adsorbed hydrogen (MH_{ads}) on the catalyst surface. The Volmer process is described by:

$$\mathrm{M} + \mathrm{H}^+ + \mathrm{e}^- \rightleftharpoons \mathrm{MH}_{\mathrm{ads}} \tag{3.10}$$

This step is followed by a Heyrovsky process which is the formation of a hydrogen molecule by combining an intermediate hydrogen adatom, a proton, and an electron, given by

$$\mathrm{MH}_{\mathrm{ads}} + \mathrm{H}^+ + \mathrm{e}^- \rightleftharpoons \mathrm{H}_2 + \mathrm{M} \tag{3.11}$$

Depending on the catalyst material, the second step can be alternatively a Tafel process in which two (MH_{ads}) combine to a H_2 molecule. The Tafel process has the form

$$2\,MH_{ads} \rightleftharpoons H_2 + 2\,M \tag{3.12}$$

Both pathways (Heyrovsky-Volmer and Tafel-Volmer) occur in HER at Pt surface. The dominance of these two paths depends on the crystal orientation of Pt, which affects the rate of HER in those crystals, Pt(111)<Pt(100)<Pt(110) <Pt polycrystals. The Volmer process on Pt is rapid (in the order of tens of femtoseconds), while the gas-evolving processes (Heyrovsky and Tafel) are usually the rate-limiting step [39]. For Pt(110)/Pt(100), the Tafel/Heyrovsky step is rate-limiting, respectively. For polycrystal Pt, the Tafel step is the dominant rate-limiting step [40, 41].

3.2 Membranes in Water Electrolysis

Practical water electrolysis cells typically incorporate a gas-impermeable (although gas cross-over cannot be avoided) and ion-conducting membrane, which isolates the half-reactions in two cells. The membrane is to separate the product gases (O_2 and H_2) and preserved ion migration pathways.

During water electrolysis, the diffusion of O_2 and H_2 to the opposite electrode is hazardous. O_2 on the HER electrode will recombine with H_2 back to water under the influence of catalysts. In the OER cell, hydrogen mixing with oxygen gases also need to be avoided to benefit efficiency and safety.

The membranes most widely used in the literature and industry are diaphragm [42] and ion-exchanging membrane (IEM). Ion-exchanging membranes are selective to specific types of ions, which can be categorised into proton-exchanging membranes (PEM, conductive for protons and cations) [35, 43, 44], anion-exchanging membranes (AEM, conductive for hydroxides) [43, 45, 46], and bipolar membranes (BPM, layered stack of a PEM and an AEM) [34]. In this section, we will introduce some fundamentals about these membranes and their performances in water electrolysis.

3.2.1 Ion exchange Membrane

In this thesis, we used AEM mainly as supporting material. However, the properties of AEM do affect the characteristics of the devices, which requires understanding the basics of ion exchange membrane. Let us start with homogeneous membranes, i.e. PEM and AEM.

3.2.1.1 Structure

Ion exchange membranes consist of a fixed polymer backbone decorated with charged functional groups for the ion exchange purpose. For example, Nafion, the first synthetic ionic polymer, is a PEM material based on a Teflon backbone with ($-SO_3{}^-$) which is a cation exchange group [47]. The AEM material used in this thesis, Fumion, has a poly(arylene ether) backbone and quaternary ammonium ($-NR_4{}^+$) groups [48], selectively allow anions to permeate.

These ionic functional groups are fixed charges that attract mobile counter ions. When the ionic polymer cross-links to form a membrane, the ionic groups cluster into conductive channels for the counter ions. An illustration of such ion-conducting channels is shown in Fig. 3.3a, where we use Nafion as an example.

Ionic functional groups cluster together at the boundary of the channel, with each ionic group attracting counter ion, in this case, a hydrated proton. Since these functional groups are hydrophilic, these channels are also filled with water. A working condition with suitable humidity is crucial for the ion transport in the membrane to be efficient. In the scale of the whole membrane, the channels interconnect and form a network around the polymer backbone and side chains (Fig. 3.3b) [49]. Since the

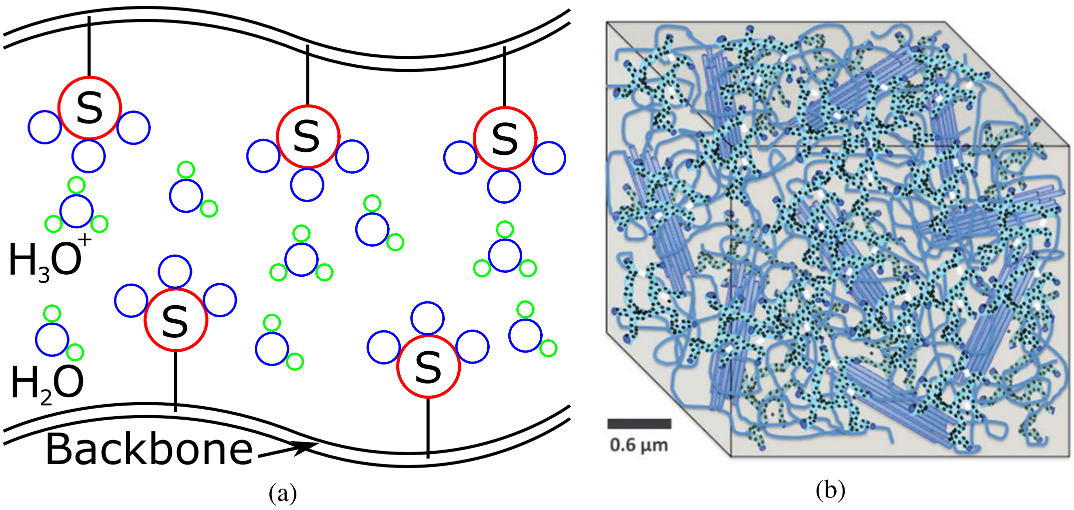

(a) (b)

Figure 3.3: Illustration of ion-conducting membrane structure. (a) Schematic of ion-conducting channel in Nafion, Showing $-SO_3^-$ groups clustering on PTFE backbone with water molecules and hydrated proton filling in the channel. Red circle: Sulfur. Blue circle: Oxygen. Green circle: Hydrogen. (b) Cluster network of Ion-conducting channels in Nafion. Network (light blue channels) of fixed functional group clusters (black dots) surrounded by PTFE backbone chains (dark blue). Taken from [49].

counter-ions are mobile in the channels, the membrane becomes conductive for these ions.

3.2.1.2 Proton and Hydroxide Transport

Protons and hydroxide ions are unique in terms of transport in aqueous solutions. Other ions following the vehicular mechanism — ions attract water molecules to form hydration shells and diffuse with the shells [50]. Protons and hydroxide ions, on the contrary, transport via the Grotthuss mechanism [50–52]. In the Grotthuss mechanism, protons hop between neighbouring water molecules, in the meantime forming and breaking hydrogen bonds [50].

The molecular structures of the protonated water involve two basic cluster structures proposed by Eigen and Zundel [53]. As annotated in Fig. 3.4a, the Eigen cation (E, black dashed circle), is a proton localised in a water molecule and solvated by three water molecules. The Zundel cation (Z, red dashed circle), is a proton being equally shared between two water molecules. There are more molecular clusters in the protonated water structure family, see [54] for a detailed description. These are the minimum-energy structures in protonated hydrogen-bond networks, which has been researched intensively by theoretical simulation and experiments such as infrared spectroscopy [53, 54].

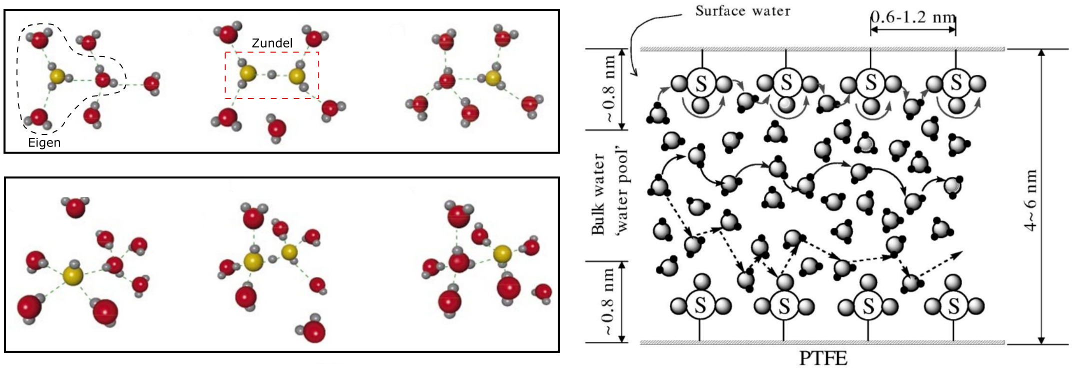

(a) (b)

Figure 3.4: Proton and hydroxide transport mechanism. (a). Proton and hydroxide transport in water. Top: the transport mechanism of hydrated protons. Bottom: the transport mechanism of hydroxide ions. Red spheres: oxygen. Grey spheres: hydrogen. Yellow spheres: oxygen in hydrated protons and hydroxide ions. Dashed green lines: hydrogen bonds. Black dashed circle: Eigen structure. Red dashed circle: Zundel structure. Adapted from [52] (b). Proton transport mechanism in Nafion channel. Adapted from [55].

When protons hop between water molecules, the local hydrogen bond clusters undergo a rearrangement [52]. This is shown in the top panel of Fig. 3.4a as an E-Z-E transition. This proton-hopping process starts with a Eigen cation, with a protonated water molecule forming a hydrogen-bond network with other three water molecules (Top left in Fig. 3.4a). The localised proton in the Eigen cation from hydrogen bond with another water molecule, sitting between two oxygen atoms. In ambient condition, the separation between the two oxygen atoms (O-O distance) oscillates because of thermal fluctuation. Once the O-O distance reduces to a certain length, it becomes easier for the proton to overcome the energy barrier, and forms a Zundel cation (Top centre in Fig. 3.4a). The proton finishes the hopping process by transferring to the other water molecule, turning back into an Eigen cation (Top right in Fig. 3.4a).

The transport mechanism for hydroxide ions is similar (Bottom in Fig. 3.4a), which can be treated as a 'proton hole' picture [52, 53]. Note that the transport mechanism of hydroxide ions is not a strict reverse of protons,since the minimum-energy hydroxide water clusters are different from the protonated water clusters [53], which require additional rearranging of hydrogen band [52].

The picture is more complex in ion-exchanging membranes, as the hydrogen bond network involves ionic functional groups in the polymer. Figure 3.4b shows possible proton transport pathways in Nafion, which includes Grotthuss diffusion in surface water, in bulk water, and H_3O^+ vehicular transport. Theoretical calculation shows that proton diffusion in bulk water is $\sim$ 5 times faster than vehicular transport and about two orders of magnitude faster than surface diffusion [55]. This explains why water content affects the proton conductivity of the membranes — surface diffusion becomes dominant when the membrane has low water content.

3.2.1.3 Donnan Exclusion and Selectivity

The most basic property of ion-exchange membranes is selectivity. Only cations and anions can permeate PEM and AEM, respectively. However, the selectivity of an ion-exchange membrane is not always perfect. For example, in high concentrations, both cations and anions can pass through PEM or AEM. Let us look into more details about selectivity.

Assuming a PEM is immersed in a 1:1 electrolyte solution, the ion concentration in the membrane $\overline{C}_-$, $\overline{C}_+$ can be calculated according to the Donnan equilibrium theory [56]. The results are given as follows

$$\begin{aligned}\overline{C}_+ &= \frac{1}{2}\left(\sqrt{\overline{C}_R^2+4C^2}+\overline{C}_R\right)\\ \overline{C}_+ &= \frac{1}{2}\left(\sqrt{\overline{C}_R^2+4C^2}-\overline{C}_R\right)\end{aligned} \tag{3.13}$$

where $\overline{C}_-$, $\overline{C}_+$ are the concentration of anions and cations in the membrane, $\overline{C}_R$ is the concentration of fixed functional groups in the membrane, and C is the concentration of the solution. It is clear that cations have higher concentration than anions in the membrane. The ratio between the two species in the PEM ($\overline{C}_-/\overline{C}_+$) is given by

$$\frac{\overline{C}_-}{\overline{C}_+} = \frac{\sqrt{\overline{C}_R^2+4C^2}-\overline{C}_R}{\sqrt{\overline{C}_R^2+4C^2}+\overline{C}_R}, \tag{3.14}$$

Equation 3.14 shows that $\overline{C}_-/\overline{C}_+$ is monotonically increasing with C from 0 toward 1. This is the Donnan exclusion of anions caused by the repelling effect of the fixed functional groups (negatively charged) at lower concentrations. In terms of $\overline{C}_R$, $\overline{C}_-/\overline{C}_+$ increases as $\overline{C}_R$ decreases, and approaches 1 as $\overline{C}_R \to \infty$. This shows that the Donnan exclusion is enhanced at higher $\overline{C}_R$.

To quantify the selectivity over multiple ions, the transport number of ion i is defined as

$$\overline{t}_i = \frac{z_i^2\overline{u}_i\overline{C}_i}{\sum z_i^2\overline{u}_i\overline{C}_i}, \tag{3.15}$$

where z_i is the charge number of ion i.

3.2.1.4 Electric conductivity

The electrical conductivity of the ion exchange membrane is related to the concentration of ions in the membrane ($\overline{C}_-$ and $\overline{C}_+$) by [56]

$$\kappa = F(\overline{\mu}_+\overline{C}_+ + \overline{\mu}_-\overline{C}_-) = F\overline{\mu}_+(\overline{C}_+ + \frac{\overline{\mu}_-}{\overline{\mu}_+\overline{C}_-}) \tag{3.16}$$

From Eq. 3.13, 3.15 and 3.16, one can calculate the conductivity of an ion exchange membrane. Figure 3.5 displays typical conductivity as a function of C and $\overline{C}_R$ for an PEM in NaCl, using $n = u_{\text{Cl}}/u_{\text{Na}}$ as a parameter. Because of Donnan exclusion, κ is constant over C for $C \ll \overline{C}_R$, as shown in Fig. 3.5a. For higher C, κ increases monotonically with C, which is, however, contributed by non-negligible cations transporting in PEM. In this region, the selectivity of the membrane is imperfect. Both anions and cations can transport through the membrane because of the relatively weak Donnan exclusion.

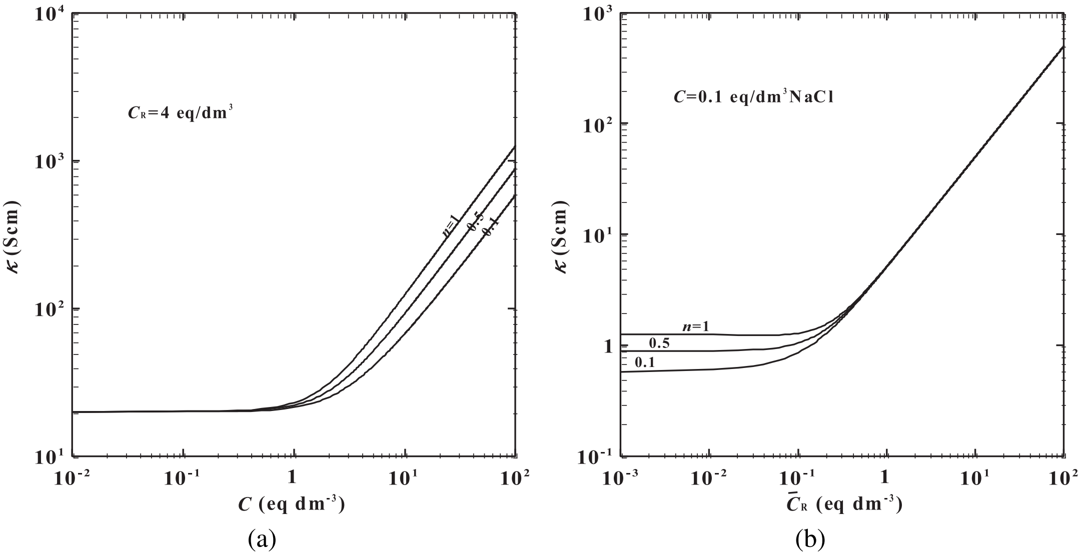

(a) (b)

Figure 3.5: Concentration dependence of ion exchange membrane conductivity. (a). Conductivity of a cation exchange membrane as a function of NaCl concentration. (b). Conductivity of a cation exchange membrane as a function of ion exchange group concentration ($\overline{C}_{\text{R}}$). Taken from reference [56].

The capacity of ionic functional groups determines both the selectivity and conductivity of the membrane. In a fixed electrolyte concentration C, for $\overline{C}_R \gg C$, the conductivity of membrane increases with $\overline{C}_R$. For lower $\overline{C}_R$, the membrane is no longer selective to anions and cations.

3.2.1.5 Membrane Potential

Suppose both sides of a PEM are in contact with solutions of the same 1:1 electrolyte, but in different concentrations, the cations can diffuse through the PEM because of the concentration difference, while the anions are blocked due to Donnan exclusion. This starts to create a positive net charge on the low-concentration side and a negative net charge on the high-concentration side. The excess net charges lead to an electric field with a direction opposite to the diffusion gradient. Hence, there would be a potential difference when the system reaches equilibrium. This potential difference is known as the membrane potential.

The building up of membrane potential changes the system energy because of the electrical work done on the diffused ions. Assuming the change of energy is reversible, one can apply the Nernst equation to the system which yields

$$\phi = -(\bar{t}_+ - \bar{t}_-)\frac{RT}{F}\ln\frac{a_2}{a_1}, \tag{3.17}$$

where a_1 and a_2 is the activity of cations and anions in the two sides of the membrane.

Taking Eq. 3.17 and that $\bar{t}_+ + \bar{t}_- = 1$, the membrane potential for PEM and AEM can be further written as

$$\begin{aligned} \text{PEM:} \quad & \phi = -(2\bar{t}_+ - 1)\frac{RT}{F}\ln\frac{a_2}{a_1} \\ \text{AEM:} \quad & \phi = (2\bar{t}_- - 1)\frac{RT}{F}\ln\frac{a_2}{a_1} \end{aligned} \tag{3.18}$$

3.2.2 Diaphragm

Unlike ion exchange membranes, diaphragms do not selectively transport ions [57]. Diaphragms are membranes with typically 100-nm-size pores which are filled with electrolytes in a water electrolysis cell. [42, 57]. Such a pore-electrolyte system can reduce gas cross-over. However, to achieve a comparable H2/O2 purity with AEM [57], diaphragms are usually much thicker ($\geq$ 500 µm) than non-porous membranes. As such, a highly concentrated electrolyte is essential to support high ionic conductivity when a diaphragm is used as a separator in water electrolysis to reduce the overpotential.

3.2.3 Membrane-based Water Electrolysis

Water electrolysis based on diaphragms is the most commercially matured water electrolysis technology because of its cost efficiency and long-term durability. Diaphragm water electrolysis is known as alkaline water electrolysis, as it operates in alkaline environments, which is less corrosive than in acidic electrolytes and thus preferred in the industry. Conventional alkaline water electrolysis can achieve a current density of 100-300 $\mathrm{mA \cdot cm^{-2}}$ at $\sim$ 2 V with near ambient temperature of 70-90 °C [42]. The limitation of alkaline water electrolysis is that 25-30 wt.% KOH aqueous solutions need to be used to provide optimum electrolyte conductivity for diaphragms.

Compared with diaphragms, polymer ion exchange membranes are densely packed structures, thus offering better gas impermeability with a thinner membrane thickness and higher ionic conductivity. Ion exchange membranes do not require a highly concentrated electrolyte and are suitable for neutral conditions because of the ionic functional groups in membranes.

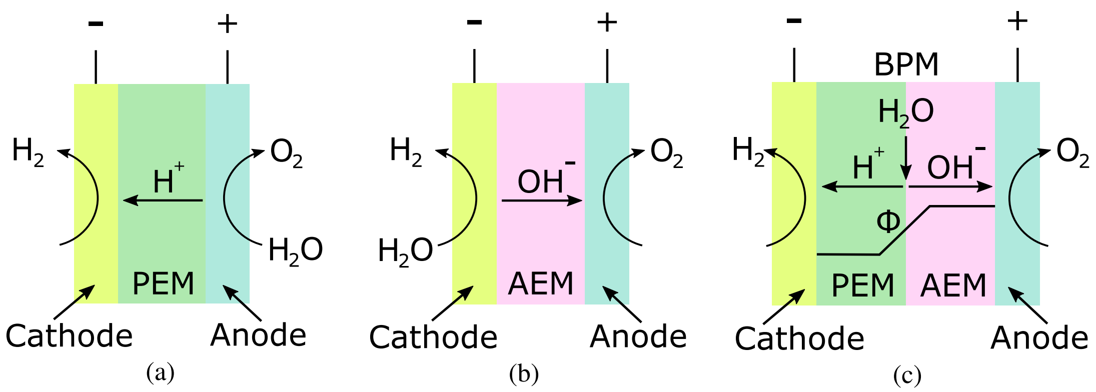

Figure 3.6: Schematic illustration of membrane-based water electrolysis. (a) Proton exchange membrane (PEM) water electrolysis. (b) Anion exchange membrane (AEM) water electrolysis. (c) Bipolar membrane (BPM) water electrolysis. Black curve: A illustration of ϕ profile across the bipolar membrane.

PEMs are used in acidic water electrolysis cells as a separator. The acidic half-reactions in Eq. 3.5 show that OER generates excess protons while HER consumes protons. A PEM allows protons to permeate from the anode-side half cell to the cathode-side half cell (Fig. 3.6a). The current densities observed for PEM water electrolysis range around 1-2 $A \cdot cm^{-2}$ with an applied bias of $\sim$ 2 V at $\sim$ 80 °C [44].

In alkaline water electrolysis, AEM-based electrolysers, as an alternative to diaphragms, have been developed over recent years. Two half cells are separated by an AEM, hydroxide ions transport through the AEM as hydroxide generated at the cathode and consumed at the anode (Fig. 3.6b). The state-of-the-art AEM water electrolysis systems operate under a current density of 200-500 $mA \cdot cm^{-2}$ at temperature 50-70 °C with cell voltage of $\sim$ 2 V [46].

BPM is a membrane junction made by an AEM and a PEM. It can be fabricated by lamination or multilayer-coating [34]. The two homogeneous membranes are bound together by a strong electrostatic force between the opposite signed fixed charges. Although BPM is traditionally applied in other electrochemical applications such as acid and alkali production, it was only adopted in water electrolysis at 2014 [58, 59]. In BPM water electrolysis, the BPM is placed in the cell in a way that the AEM faces the alkaline electrolyte and the PEM faces the acid electrolyte. Without external bias, the counter-ions (protons and hydroxide) in the AEM and PEM layers diffuse toward each other and recombine into water molecules. As a result, the region near the interface of AEM and PEM is depleted and left with the fixed charges. The spacial charges generate a junction potential and a built-in electric field, pointing from AEM to PEM layer. Applying a cell voltage with the same polarity as the field, as shown in Fig. 3.6c, increases the field strength at the interface, which lead to a larger current.

Several mechanisms have been proposed to explain this enhanced field effect. One is the Onsager's theory of the (second) Wien effect, that the strong field polarises the water molecules and accelerate water dissociation [60]. The other mechanism is water dissociation catalysis via protonation-deprotonation reactions on the site of ionic function groups [61].

The main advantage of BPM electrolysis is the conservation of a long-term stable pH gradient across the membrane. This leads to a reduction in the water-splitting voltages, and enables the usage of HER and OER catalysis in different optimum pH conditions. Recent improvements of current densities of BPM water electrolysis have involved the use of efficient water dissociation catalysis [62–64], an asymmetrical design of layer thickness [63, 65], and 3D bipolar junctions [66, 67].

Catalysts can be inserted into the interfacial region to accelerate water dissociation. Oener *et al.* in 2021 demonstrated a current density of $\sim 500\ \mathrm{mA \cdot cm^{-2}}$ with a cell voltage of 2 V at room temperature, using a BPM with ultrathin ($\sim 2\ \mu\mathrm{m}$) CEM layer and $\mathrm{IrO_2/NiO}$ water dissociation catalytic layer (see Fig. 3.7a). The thin CEM layer is designed to enhance the water diffusion into the interface region to promote the water dissociation rate. This is so far the largest current density achieved in regular BPM water electrolysis.

It is worth mentioning that Thiele *et al.* adopted a hybrid BPM/PEM design that operated at a current density of $5\ \mathrm{A \cdot cm^{-2}}$ (2 V cell voltage, 80 °C). The discontinuous

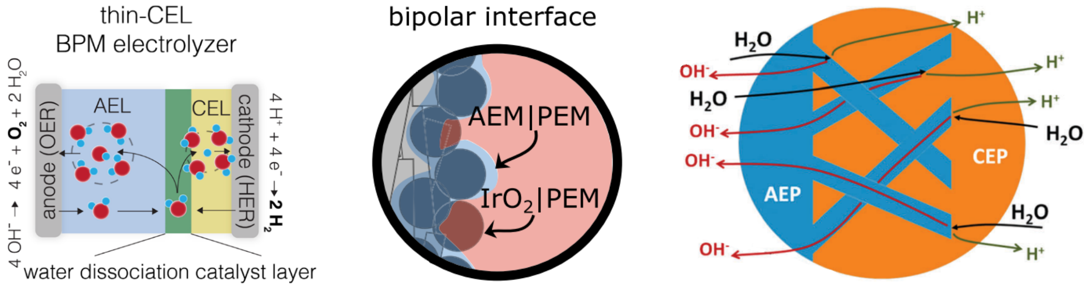

(a) (b) (c)

Figure 3.7: State-of-the-art bipolar membrane designs achieving high current densities. (a). Thin cation exchange layer (CEL) with water dissociation catalyst layer. Taken from [63]. (b). Discontinous ultranthin anion layer with water dissociation catalyst layer. Taken from [65]. (c). 3D bipolar junction made with cation exchange polymer (CEP) and anion exchange polymer (AEP) fibres. Taken from [66].

thin AEM layer they used forms microscale BPM junctions and PEM|anode interfaces, as shown in Fig. 3.7b, which makes it difficult to directly compare the performance with regular BPM water electrolysis systems.

Another method is to use 3D bipolar junctions to improved the BPM interface area. In [66], the authors used electrospinning to fabricate interpenetrating PEM and AEM fibres (Fig. 3.7c) in what would be an interfacial region in traditional planar BPM. It is anticipated that such a structure would improve the bipolar reaction area, where water dissociation takes place. In their experiments, current densities $\sim 1.2\ \mathrm{A \cdot cm^{-2}}$ were achieved with a cell voltage of 2 V at room temperature.

3.3 Electric Field effect in Water dissociation

The Wien effect was first observed in the 1920s in high-voltage conductance cells (for measuring electrolyte conductivity) [30]. In these early experiments, fields of about $1 \times 10^7\ \mathrm{V \cdot m^{-1}}$ was achieved and could accelerate the dissociation of weak electrolytes in water and partially ionised strong electrolytes in organic solvents [30].

3.3.1 Theoretical Research

There has long been strong interest in promoting water dissociation using electric field [10]. However, most of what is known about field effects in water come from ab initio theories using molecular dynamics simulation. The lack of experimental insights is due to the high field strength ($>1 \times 10^8$ $\mathrm{V \cdot m^{-1}}$) required to overcome the dielectric screening of water [8, 10]. It is clear, as can be seen in Eq. 2.44 and 2.50, that the large dielectric constant ε_r of water limits the change of ion density under electric field.

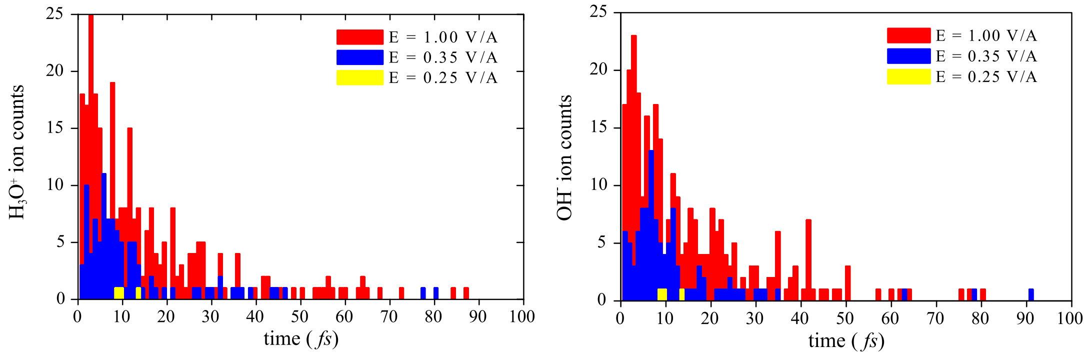

(a) (b)

Figure 3.8: Counts of OH^- and H_3O^+ ionic species as a function of time. (a) Counts of OH^-. (b) Counts of H_3O^+. Taken from reference [68].

In ab initio studies, field effects have been found relevant to the water auto-ionisation, i.e. the water dissociation equilibrium without an external field. Parrinello *et al.* found that oxygen-hydrogen bond becomes unstable when a rare fluctuation in solvent electric field occurs, which leads to the auto-ionisation of water molecules [69]. The field fluctuation causes the cleavage of an oxygen-hydrogen bond, generating an unbound proton which later hops away along hydrogen bond wires via the Grotthus mechanism. Typical solvent fluctuation vanishes within 150 fs, which is followed by a fast recombination (<100 fs) of proton and hydroxide ions[69]. However, if the reorganisation of the hydrogen-bond network breaks the hydrogen bonds, then the rapid recombination through proton transport can not happen. Further study shown that a longer time

($\sim$ 0.5 ps) is typically needed to observe a collective compression of the hydrogen bond wires and then can rapid recombination happen through the compressed wires [70].

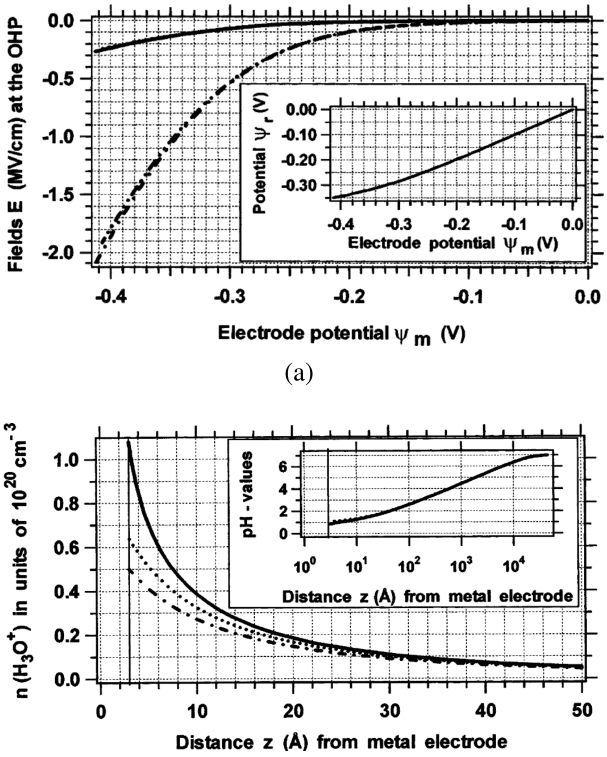

(a)

(b)

Figure 3.9: Analytical calculation of field effect on water near metal electrodes. (a) Field strength in the electrical double layer as a function of electrode potential. (b) Density of H_3O^+ as a function of distance to the electrode surface. Taken from reference [71].

The effect of an applied electric field on the water dissociation was also studied by ab initio molecular dynamics [68]. Saitta *et al.* found that in low fields ($<$ $0.35\ \mathrm{V}\cdot\mathrm{\mathring{A}}^{-1}$), water molecules start to align with the field, and protons jump back and forth along the hydrogen bond wires. Water dissociation and increase of proton currents are observed once the field increases above the threshold due to a more frequent proton hopping along the direction of the field. Figure 3.8 shows the counts of OH^- and H_3O^+ in fields of $0.25\ \mathrm{V}\cdot\mathrm{\mathring{A}}^{-1}$, $0.35\ \mathrm{V}\cdot\mathrm{\mathring{A}}^{-1}$, and $1\ \mathrm{V}\cdot\mathrm{\mathring{A}}^{-1}$. Both the counts of ion species and their lifetimes increase with electric field strength. With a field reaching $1\ \mathrm{V} \cdot \mathrm{\AA}^{-1}$, about 15%–20% of water molecules instantaneously dissociate, and a conductance of $\sim 7.8\ \mathrm{S} \cdot \mathrm{cm}^{-1}$ can be achieved.

Apart from ab initio studies, analytical calculations also predicted consistent results with these studies. As we discussed before, the electric field at the surface of a planner electrode immersed in an electrolyte can be estimated using the electric double layer model. Onsager's theory of the Wien effect can be used to calculate the concentration of dissociated ions under an electric field. The results of an analytical model calculated for a negatively charged electrode in pure water are displayed in Fig. 3.9 [71]. It is shown that the electric field strength at the electrode surface can be as high as $2\ \mathrm{MV} \cdot \mathrm{cm}^{-1}$ ($2 \times 10^8\ \mathrm{V} \cdot \mathrm{m}^{-1}$) at a electrode potential of 0.4 V (Fig. 3.9a) and the concentration of H_3O^+ increases near the electrode surface (Fig. 3.9b).

3.3.2 Experiments

From the above discussion, it seems viable to observe the field effect using the large field present on the surface of any electrodes by measuring the change of electrolyte conductivity. However, two separated electrodes have to be used for such transport measurements. Since the proton concentration decays rapidly in just a few angstroms away from the electrode surface because of water recombination, the effect would be again below the detection limit. One could place these two electrodes just a few angstroms away from each other to measure the electrolyte conductivity close to the electrode surface. But the pressure ($P = \varepsilon_r \varepsilon_0 E^2/2 \sim 1000$ bar) caused by the electrostatic forces would certainly lead the two electrodes to collapse into each other.

Due to these reasons, observation of field effecting in water by transport measurement remains elusive. So far, the direct observation of field effects in water dissociation is from complicated experiments using high-voltage cells [72, 73]. Other research works that claimed observation of field effects in water include nano-gap electrolysis cells [74], and BPM-based water electrolysis cells [60, 62]. Let us review these results.

High-voltage cells take advantage of field amplification on sharp metal tips, which can routinely produce electric fields around $1\ \mathrm{V}\cdot\mathrm{\AA}^{-1}$ by applying potential ~ 1 kV on tips with radius ~ 500 Å [10, 72, 75]. These tips are known as field emitters. A typical apparatus consists of a field emitter and a counter electrode (see Fig. 3.10). Water is adsorbed on the tip by vapour depositing. Combined with mass spectrometry, the field effect in water can be observed. The earliest experimental results in field ionization of water can trace back to the 1950s, where protonated water clusters ($(H_2O)_nH^+$) were observed. Schmidt *et al.* reported in [73] a 10^4 times increases of the ionization rate of water on tungsten and platinum at a field of $\sim 1\ \mathrm{V}\cdot\mathrm{\AA}^{-1}$. A detailed review of this direction can be found in [10].

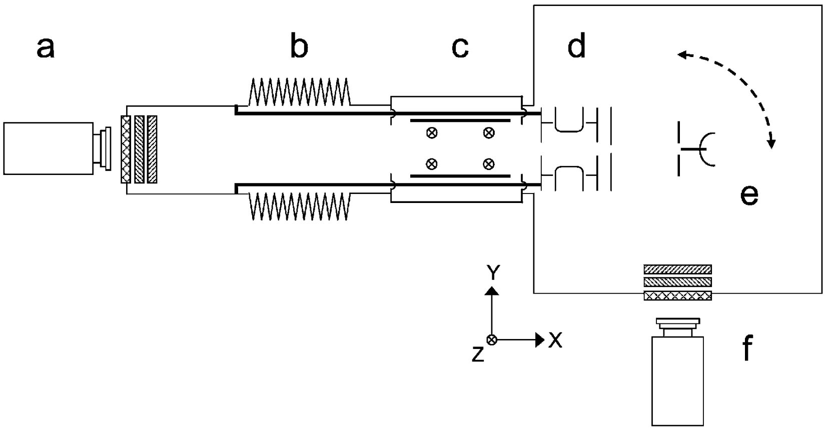

Figure 3.10: Schematics of a field ionisation apparatus. (a) Camera for signal acquisition. (b) Adjustable ion flight tube. (c) Wien field for mass selection. (d) Ion focusing length. (e) Field emitter assembly. (f) Camera for field ion microscopy. Taken from [75].

There have been research works on electrolysis cells with two electrodes separated in sub-Debye-length to study nanoscale electrochemistry [76, 77]. Wang *et al.* adopted the nano-gap electrolysis cell in water splitting [74]. They fabricated devices with two micro-electrodes (gold anode and Pt cathode) sandwiching a SiNx layer with a thickness as thin as 37 nm, which could achieve a field $\sim 1 \times 10^7\ \mathrm{V \cdot m^{-1}}$ by simulation. The author argued that the electrolysis current of pure water (0.15 mA at 1.8 V) were comparable to 1 M NaOH solutions (0.3 mA at 1.8 V) in their devices, thus claimed a 10^5 improve of water conductivity according to conductivities of pure water and 1 M NaOH in literature. However, since their results are based on electrolysis, straightforward comparison between the currents is not as reliable as conductivity transport measurements.

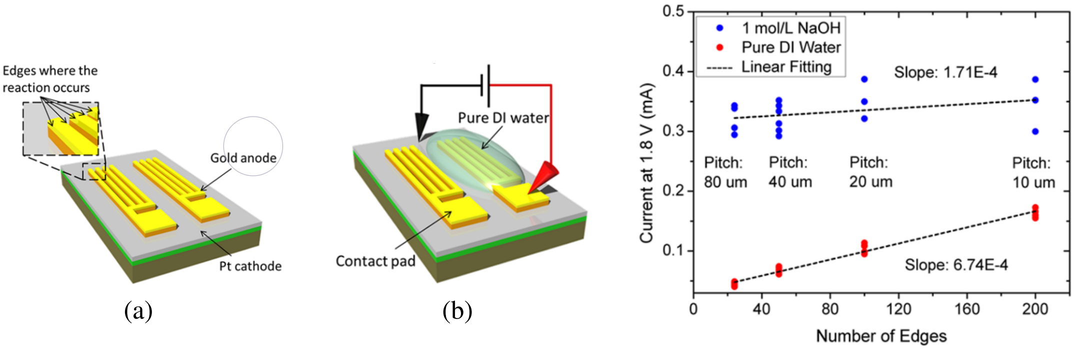

(a) (b) (c)

Figure 3.11: Field-assisted water electrolysis in a nanogap cell. (a). Device geometry. (b). Experimental setup. (c). Electrolysis current from water splitting in pure water and 1 M sodium hydroxide solution. Taken from [74].

Bipolar membrane another system that one could observe a field effect in water dissociation [60]. We have reviewed works in BPM water electrolysis cells in Section 3.2.3. Here we comment specifically on the observation of field effect in water dissociation with BPM cells.

In the interfacial region of BPM, there is a built-in electric field, with a strength predicted to be around $10^7 - 10^8\ \mathrm{V \cdot m^{-1}}$. Such a strong field should result in high current density if the field effect is dominant in BPM water electrolysis. However, no BPM systems without a water dissociation catalyst have shown higher current densities than their counterparts (PEM, AEM). Typical current densities of membrane-based water electrolysis cells range from $\sim 0.1-2$ A $\cdot$ cm^{-2} with a bias of ~ 2 V, as we have reviewed in Section 3.2.3.

Indeed, there has been a long-standing debate on which of the two mechanisms — field effect [60] or the water dissociation catalysis [61] — is more important to the enhancement in the BPM junction. The catalytic properties of functional groups in the membrane are considered to account for the enhancement of water dissociation rate in BPM, which shows more realistic theoretical predictions on the reaction rate [61, 78]. Oener *et al.* systematically studied bunches of water dissociation catalysts in BPM junction [62]. It is found that even BPM with the weakest catalyst shows higher current density than the BPM without catalyst (thinnest interface layer, largest field strength). Although this can not fully rule out the contribution from the field effect, it provides strong support for the catalytic explanation for BPM. With the catalytic effects, it is difficult to solely study the field effect using BPM systems.

Chapter 4

Fundamentals of Graphene

The objective of this chapter is to give an introduction to the properties of graphene. In the beginning, the lattice and the electronic band structure of graphene are discussed, which is followed by an introduction to the electrical and optical properties of graphene. After that, the mass transport properties of graphene are reviewed, among which graphene's impermeability and proton conductivity are of particular importance.

4.1 The discovery of graphene

Graphene, the first isolated two-dimensional material, is a monolayer building block of graphitic crystals. The discovery of isolated graphene, achieved by A. K. Geim and K. S. Novoselov, earned them the 2010 Nobel prize in physics [79]. Before its isolation, graphene was believed for a long time to be a non-existent material, impossible to isolate [80].

Back in the 1930s, it was argued that two-dimensional crystal lattices were not thermodynamically stable [81, 82]. Monolayers of these thin films would melt at any finite temperature to from islands or decompose [83, 84]. The only experimental exceptions are atomic monolayers epitaxially grown on single crystals with a matching crystal lattice [83, 84]. In 2004, atomically thin carbon layers were isolated from graphite by mechanical exfoliation with exceptional quality using a cost-effective and commonly available method [79]. The success in isolating graphene demonstrates that monolayer carbon atoms can exist without the need of a matching monocrystal base. Not violating the theory, the isolated crystals become stable because of their strong interatomic bonds and gentle warping in the third dimension [80].

4.2 Graphene lattice and band structure

The crystal structure of graphene resembles a honeycomb structure, which can be described by a triangular Bravais lattice with a two-atom unit cell as a basis, or equivalently, two sets of sublattice (*A* and *B*), as shown in Fig. 4.1a.

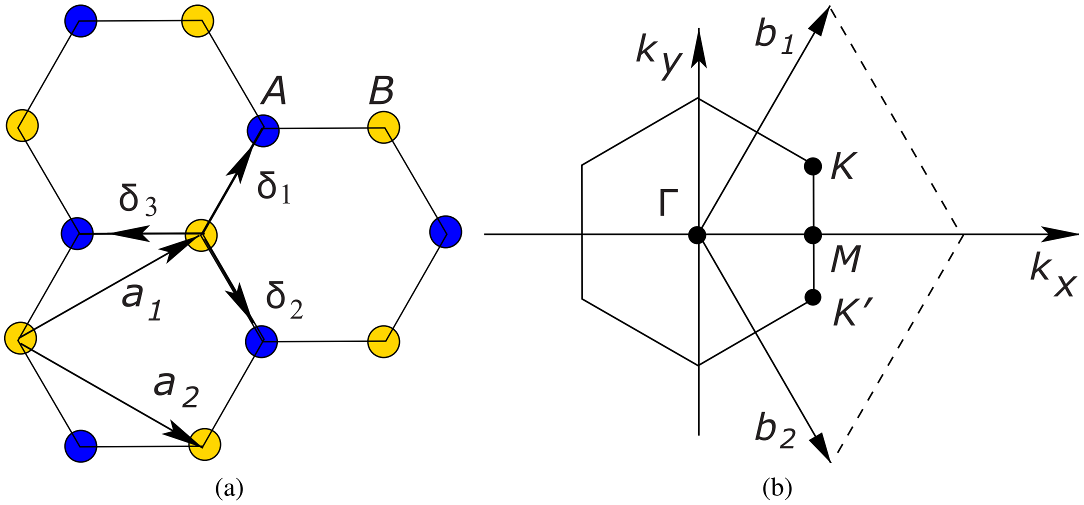

Figure 4.1: Graphene lattice structure and Brillouin zone. (a) crystal lattice structure of graphene, $\boldsymbol{a_1}$ and $\boldsymbol{a_2}$ are the lattice unit vectors, δ_1, δ_2 and δ_3 are the nearest-neighbour vectors.(b) Graphene Brillouin zone with Γ, Q, M, K, K' points, $\boldsymbol{b_1}$ and $\boldsymbol{b_2}$ the reciprocal lattice vectors. Figures from [85].

Layers of such structures are stacked and bound by a relatively weak van der Waals force in graphite, which allows for exfoliating monolayer graphene [79]. The bonding formation of graphene requires reconfiguration of carbon's shell atomic orbitals. The

$2s$, $2p_x$ and $2p_y$ orbitals of each carbon atom hybridise to sp^2 hybrid orbitals. Each carbon atom forms three in-plane σ bonds via the sp^2 hybrid orbitals with their nearest neighbours, determining its great mechanical stiffness [86]. Indeed, graphene is the strongest of any material, with Young's modulus of 1 TPa and an ultimate tensile strength (breaking limit) of 130 GPa (500 times stronger than steel).

The residual shell electrons form delocalised π bonds with the neighbours' paralleling $2p_z$ orbitals, allowing its in-plane electron transport [87]. Experiments have characterised a bunch of graphene's electronic properties, many of which are exceptional among other materials. The first experiment on few-layer graphene achieved carrier mobility of $\sim 10\,000\,\mathrm{cm}^2 \cdot \mathrm{V}^{-1} \cdot \mathrm{s}^{-1}$ in room temperature [79]. By encapsulating monolayer graphene between two hexagonal boron nitride crystals, the room-temperature carrier mobility was further improved to $> 1 \times 10^5\,\mathrm{cm}^2 \cdot \mathrm{V}^{-1} \cdot \mathrm{s}^{-1}$ at low carrier density of $\sim 1 \times 10^{11}\,\mathrm{cm}^{-2}$ [88]. The thermal conductivity of graphene is $5300\,\mathrm{W} \cdot \mathrm{m}^{-1} \cdot \mathrm{K}^{-1}$ (10 times higher than copper, twice higher than carbon nanotube and graphite) [89].

The electronic band structure of monolayer graphene can be calculated using a tight-binding approach. This was firstly done by Wallace in 1947, where graphene was used as an academic material to study the electronic properties of graphite [90]. The rest information in this section much follows the works in [85] and [91]. The real space triangular lattice vectors of the graphene primitive cell are given by

$$\boldsymbol{a_1} = \frac{a}{2}(3, \sqrt{3}), \quad \boldsymbol{a_2} = \frac{a}{2}(3, -\sqrt{3}), \tag{4.1}$$

where $a \approx 1.42$ Å is the distance of the nearest neighbour. Each carbon atom from sublattice A are surrounded by three atoms from sublattice B, and vice versa. The nearest neighbour vectors are given by

$$\boldsymbol{\delta_1} = \frac{a}{2}(1,\sqrt{3}), \quad \boldsymbol{\delta_2} = \frac{a}{2}(1,-\sqrt{3}), \quad \boldsymbol{\delta_1} = a(-1,0), \tag{4.2}$$

and the six secondly nearest neighbour vectors are

$$\boldsymbol{\delta'_1} = \pm \boldsymbol{a_1}, \quad \boldsymbol{\delta'_2} = \pm \boldsymbol{a_2}, \quad \boldsymbol{\delta'_2} = \pm(\boldsymbol{a_2} - \boldsymbol{a_1}) \tag{4.3}$$

The graphene Brillouin zone — the reciprocal space primitive cell — is shown in Fig. 4.1b. The reciprocal lattice vectors are

$$\boldsymbol{b_1} = \frac{2\pi}{3a}(1,\sqrt{3}), \quad \boldsymbol{b_2} = \frac{2\pi}{3a}(1,-\sqrt{3}). \tag{4.4}$$

The two corner points in the Brillouin zone are expressed as K and K' whose coordinates in the reciprocal space are given by

$$\boldsymbol{K} = (\frac{2\pi}{3a}, \frac{2\pi}{3\sqrt{3}a}), \quad \boldsymbol{K'} = (\frac{2\pi}{3a}, -\frac{2\pi}{3\sqrt{3}a}). \tag{4.5}$$

The energy bands derived from tight bonding theory considering electron hopping to the nearest and second-nearest neighbours can be expressed as [90]

$$E_{\pm}(\boldsymbol{k}) = \pm t\sqrt{3 + f(\boldsymbol{k})} - t' f(\boldsymbol{k}), \tag{4.6}$$

$$f(\boldsymbol{k}) = 2\cos\left(\sqrt{3}k_y a\right) + 4\cos\left(\frac{\sqrt{3}}{2}k_y a\right)\cos\left(\frac{3}{2}k_x a\right) \tag{4.7}$$

where $\boldsymbol{k} = (k_x, k_y)$ represents coordinate in the first Brillouin zone, the ± sign refers to upper anti-bonding π^* band and lower bonding π band, $t \approx 2.8$ eV is the hopping energy to nearest neighbours and t' is second-nearest hopping energy.

The electronic band structure of graphene is exhibited in Fig. 4.2. The π^* and π

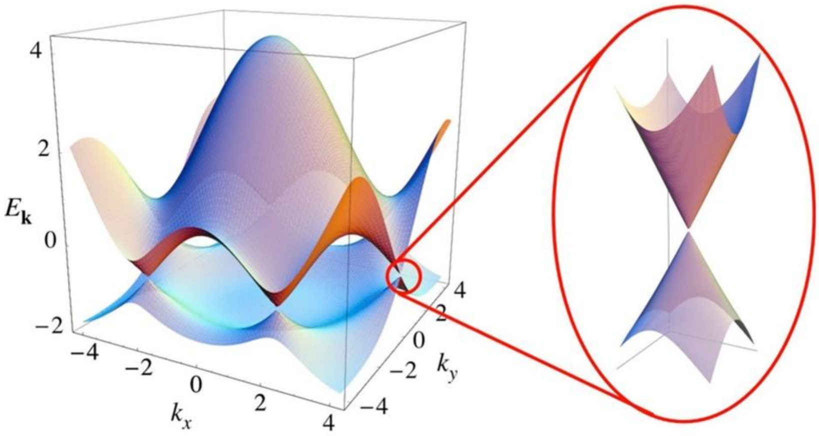

Figure 4.2: Band structure of monolayer graphene. Left: $E_\pm(\boldsymbol{k})$ with $t = 2.7$ eV and $t' = -0.2t$. Right: zoom-in of a Dirac cone. Figure from ref. [85]

bands are also known as the valence band and the conduction band, they crossover via a singular point (K or K'). In equilibrium, electrons fill the bands starting from the lowest energy level and only up to a threshold determined by the chemical potential of the system, known as the Fermi level. For undoped graphene, the Fermi level sits at the intersection point of the cone, which means graphene has a filled valence band and an empty conduction band. It is neither a metal (half-filled and continuously overlapping bands) nor an insulator (fully filled valence band, large band-gap), and not a semiconductor (narrow band-gap). This cone-shaped band structure determines graphene as a semi-metal.

A zoom-in of the band structure near one of the corner points is known as Dirac cone. K or K' points are thus named as Dirac points. The Dirac cone can be expressed by expanding $E_\pm(\boldsymbol{k})$ at K or K' points, as

$$E_\pm(\boldsymbol{q}) = \pm\hbar v_F q + O[(q/K)^2], \tag{4.8}$$

where $\boldsymbol{q}$ is a momentum with respect to K or K' points with $q = |\boldsymbol{q}| \ll |\boldsymbol{K}| = K$,

$v_F = 3ta/2$ is the Fermi velocity, $\hbar$ is the reduces Planck's constant. This linear dispersion relation is one of graphene's landmark properties. In a conventional bulk semiconductor, the band structure near the band minimum/maximum is usually approximated with a parabolic dispersion $E(q) = \hbar^2 q^2/2m^*$ where m^* is the carrier mass within the system. The linear dispersion determines that the charge carriers in graphene behave as massless Dirac fermions.

4.3 Electric field effect in graphene

Electronic transport study reveals a lot of interesting phenomena in graphene, such as electrical field effect, non-vanishing zero-field conductivity, room-temperature quantum Hall effect, Klein tunneling through potential barriers. Let us review the electric field effect in graphene that allows controlling of graphene's Fermi energy to tune its carrier polarity and density [79].

In a typical electron transport measurement, graphene was fabricated into a structure known as Hall bar, as shown in Fig. 4.3. A Hall bar contains multiple pairs of electrodes making contact with micro-etched graphene channels. The geometry of electrode allows for a typical four-probe resistivity measurement of the crystal to eliminate the contact resistance.

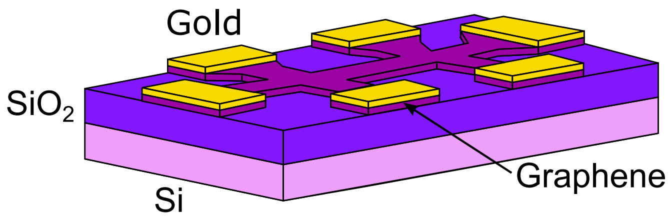

Figure 4.3: Schematic of a graphene Hall bar for electric transport measurement.

The graphene channel is placed on a dielectric layer (SiO_2) on a conductive substrate (Si), allowing a gate voltage applied to the substrate. Consider the device as a capacitor with capacitance C per unit area, with a gate voltage of V_g applied, the carrier density in graphene is given by

$$n = \frac{CV_g}{e}, \tag{4.9}$$

where e is the elementary charge. For a channel with length l and width w, the resistivity of the channel is given by

$$\rho = R\frac{w}{l}, \tag{4.10}$$

where $R = V/I$ is the resistance measured from I-V characterisation. A typical dependence of ρ on the gate voltage V_g and thus on the carrier concentration n is exhibited in Fig. 4.4a. The position of Fermi level moves across the Dirac point with V_g moving from negative to positive, which indicates a electrostatic doping controlled by the gate voltage.

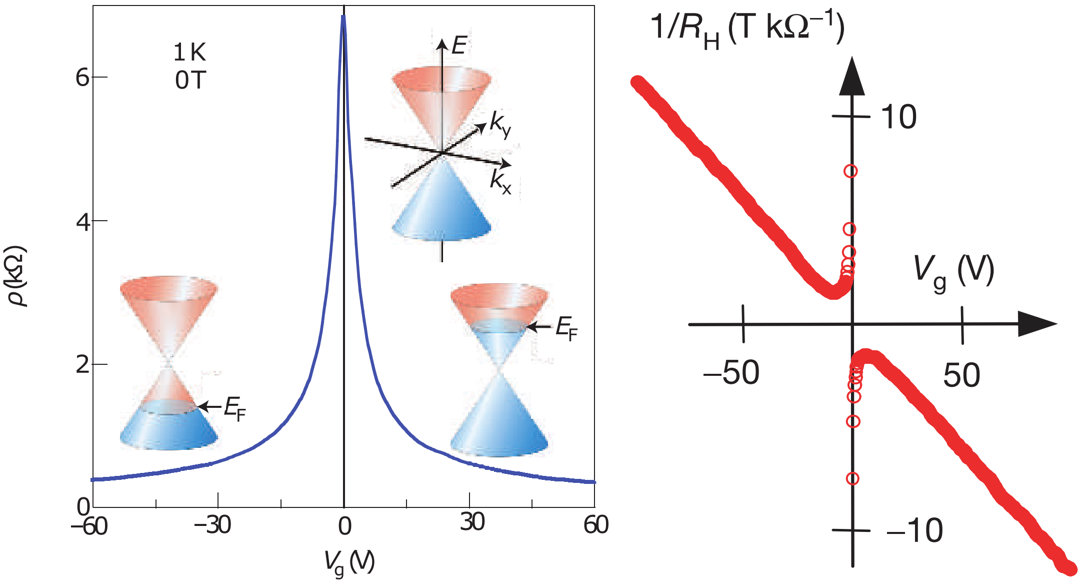

(a) (b)

Figure 4.4: Electric field effect in graphene. (a) Resistivity ρ of monolayer graphene versus gate voltage V_g. Insets show the Fermi energy level corresponding to there different gating voltages. Taken from [80]. (b) Hall coefficient R_H as a function of V_g. Taken from [92].

The carrier concentration can be determined experimentally using the Hall effect.

By placing the graphene device in a non-quantising magnetic field B orienting perpendicularly to the graphene plane [79, 92], the Hall coefficient R_H can be measured by

$$R_H = \frac{V_H}{I}\frac{1}{B}, \tag{4.11}$$

where V_H is the Hall voltage measured transversally to the direction of current I.

According to the Drude model, which treats the charge carriers classically, the conductivity $\sigma = 1/\rho$ is determined by

$$\sigma = \mu e n, \tag{4.12}$$

where μ is the charge mobility that determines how fast the charge carriers move in the system. Note that $1/R_H \propto n$, as the Hall coefficient is determined by

$$R_H = 1/en. \tag{4.13}$$

From Eq. 4.9, $n \propto V_g$. Hence $1/R_H \propto V_g$, which is shown in Fig. 4.4b. Combining Eq. 4.12 and 4.13 yields

$$\mu = \sigma R_H = \frac{R_H}{\rho}. \tag{4.14}$$

This allows the measurement of charge carrier mobility.

Another important feature is graphene's non-vanishing zero-field conductivity. As shown in Fig. 4.4a, the resistivity ρ reaches maximum at the neutrality point ($V_g = 0$), but $\rho \neq \infty$. In Fig. 4.4b, $1/R_H$ diverges near the neutrality point indicating a non-zero carrier density. Confirmed by multiple experiments [80, 92], the zero-field resistivity $\rho_{\max}$ is $\sim h/4e^2$ which is a robust phenomena and does not require high quality (mobility) graphene. Indeed, near the neutrality point, graphene is conductive as a random network of electron and hole puddles because of the self-doping induced by the warping/rippling of graphene sheets [80, 92]. This feature indicates that graphene is always conducting. This results in graphene's low on/off ratio, hence hindering its digital application. Nevertheless, this is suitable in some cases, for example, using graphene as an electrochemical electrode. Moreover, graphene is naturally doped by depositing it onto a substrate or metal contact, which increases its conductivity in practice.

4.4 Optical properties

Graphene shows several appealing optical properties making it a remarkable material for photonics and optoelectronics applications [93–95]. The optical properties of nanomaterials are determined by the light-matter interaction — photons interacting with electrons and nucleis. These interactions include processes such as light absorption, emission, electron relaxation, as depicted in Fig. 4.5a. As a background of this thesis, graphene's basic optical properties are briefly reviewed in this section, focusing on the absorption and hot carrier relaxation properties. In particular, the physical mechanisms allowing graphene's photocurrent generation will be discussed.

The optical absorption of graphene arises from two different pathways, intra-band absorption and inter-band absorption. When a photon is absorbed, an electron is excited from an energy level to a high-energy level, leaving a hole in the low-energy level. The energy difference between the two energy levels determines the energy of the photon and the frequency of light that graphene can absorb. In an intra-band transition, the two energy levels involved are from the same band, which contributes to the light absorption in far-infrared region.

An inter-band transition is a direct optical transition from graphene's valence band to conduction band, as shown in Fig. 4.5b. For light absorption in the linear dispersion region, theory predicted that the transmittance of graphene is independent of

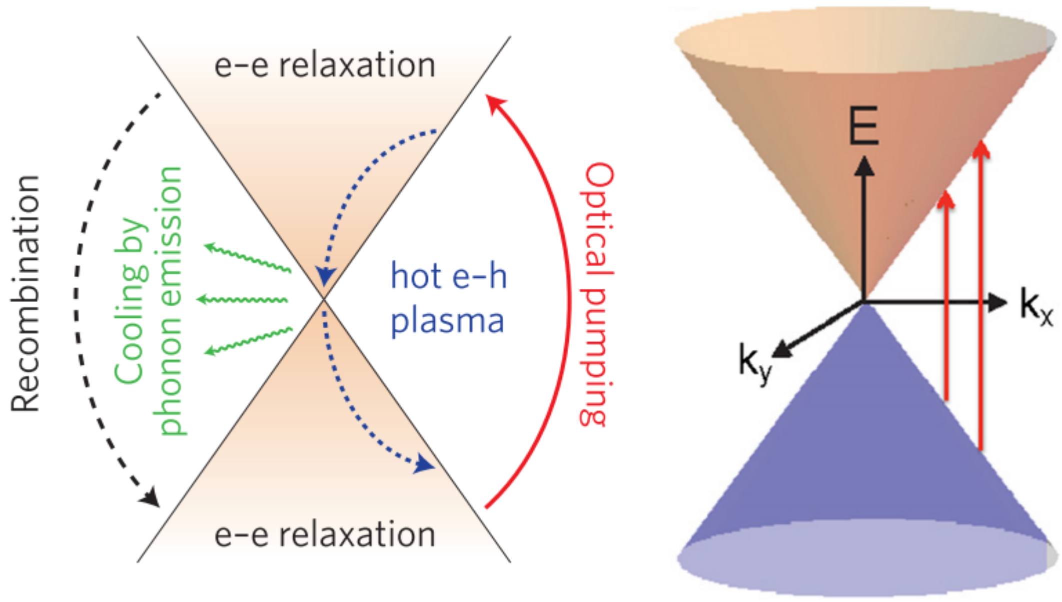

(a) (b)

Figure 4.5: Light-matter interaction in graphene. (a) Photo excitation and possible relaxation pathways in graphene. Taken from [93]. (b) Graphene inter-band absorption. Taken from [94].

the light wavelength [96]. Experimental results show that the absorption spectrum of single layer graphene is quite flat $\sim$ 2.3 % from 300 nm to 2500 nm (visible to near infrared) [96, 97]. This property makes graphene suitable for use as a transparent electrode for display and solar energy applications [93]. For photon energy in near ultra violet, interband transition is contributed by the energy dispersion around the saddle point M, as shown in Fig. 4.2 and 4.1b. A peak of absorption at $\sim$ 270 nm arises due to the saddle-point excitons [98].

As electron-hole pairs are generated during light absorption, the nonequilibrium carriers can result in a photocurrent that can be detected in graphene photodetectors. Photocurrent has been reported in graphene/metal interfaces [99–101], gated graphene bipolar junctions [102–105] and graphene/semiconductor Schottky junctions [106]. Several mechanisms were used to explain the photocurrent generation in graphene devices, as shown in Fig. 4.6.

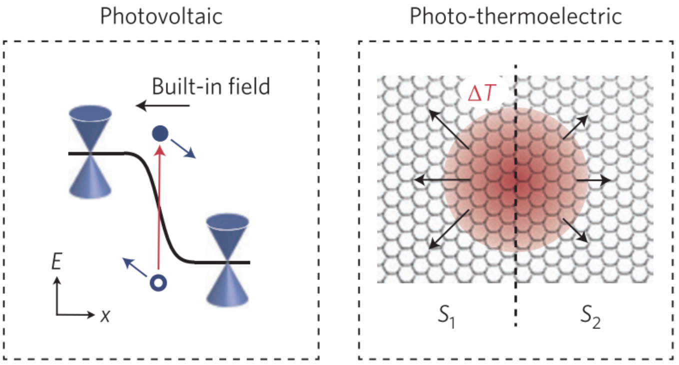

Figure 4.6: Schematic representation of the photocurrent generation mechanisms in graphene.

Initially, photocurrent detection in graphene/metal contacts suggested that the photocurrent is generated by the photovoltaic effect [99–101]. Doping of graphene by metallic contacts or gating introduces chemical potential differences across graphene regions with different doping strengths. This results in a band bending, causing the carriers to redistribute to equilibrium and thus a built-in electric field. Photo-excited charge pairs are then separated by the built-in field, which results in a photocurrent. This can also explain the photo-response in graphene Schottky diodes, where band bending occurs at the interface between graphene and semiconductor [106].

Further studies show that relaxation pathway of photo-excited carriers in graphene support relatively long-lived hot electron. Carriers are initially cooled by electron-electron scattering and optical phonon emission, which only involves very hot electrons. The electron cooling is then limited by the inefficient electron-to-lattice energy transfer. Because of this, the temperature difference (ΔT) created by long-lived hot electrons allows photocurrent detection by thermoelectric effect [102, 103]. It was soon clear that this photothermoelectric (PTE) effect dominates the photocurrent generation in graphene [102, 103], although the photovoltaic effect contribution can not be fully neglected in some cases [104]. Thermoelectric current is strongly dependent on the carrier type (electron/hole, determines the sign of the generated current) and the thermoelectric power (S, determines how large voltage can be generated per unit temperature) of a material (Fig. 4.6). For undoped homogenous graphene, the net thermoelectric current induced by ΔT would be zero, as the current is isotropic.

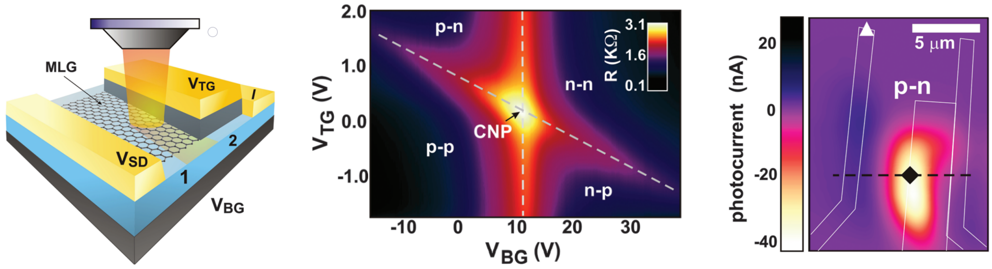

(a) (b) (c)

Figure 4.7: Graphene dual gate p-n junction. (a) Device geometry. (b) Resistance map as a function of dual gate voltage. (c). Photocurrent map of the device. Figures taken from [102].

A typical geometry used to demonstrate PTE effect in graphene is a dual gate structure, as shown in Fig. 4.7a. The dual-gate structure allows doping differences in the two graphene areas, one with a bottom gate and the other with both bottom and top gates, forming a junction between the two areas. This results in a four-fold resistance map as a function of the dual gate voltage (Fig. 4.7b). The doping difference results in a broken symmetry of S in graphene. Thus, the photocurrent can be observed by illuminating the p-n junction area (Fig. 4.7c). The photocurrent ($I = V_{\mathrm{PTE}}/R$) are induced by the photothermoelectric voltage (V_{PTE}) which is given by the Seebeck effect as

$$V_{\mathrm{PTE}} = (S_2 - S_1)\Delta T, \tag{4.15}$$

where $\Delta T = T_e - T_l$ is the difference between the excited hot electron temperature T_e and lattice temperature T_l.

Figure 4.8a shows a photovoltage map as a function of the dual gate voltage. The six-fold pattern is a result of multiple sign reversal of the quantity $S_2 - S_1$ [102]. This is one of the characteristic properties of graphene's photo-response via the thermoelectric process.

Another feature of PTE effect in graphene is its dependence on the incident light power obeys a power law, as shown in Fig. 4.8b. According to the super collision model [103], which predicsts a more efficient electron-lattice cooling pathway, the electronic temperature T_e in graphene induced by an incident power P is given by

$$T_e = (P/A)^{1/3} \tag{4.16}$$

Since the phonon system (lattice) may take a larger portion of the energy at higher power excitation, the power scaling is expected to be $T_e \propto P^{1/n}, n \geq 3$. According to Eq. 4.15, $V_{\text{PTE}} \propto T_e$, thus $I \propto V_{\text{PTE}} \propto P^{1/n}$.

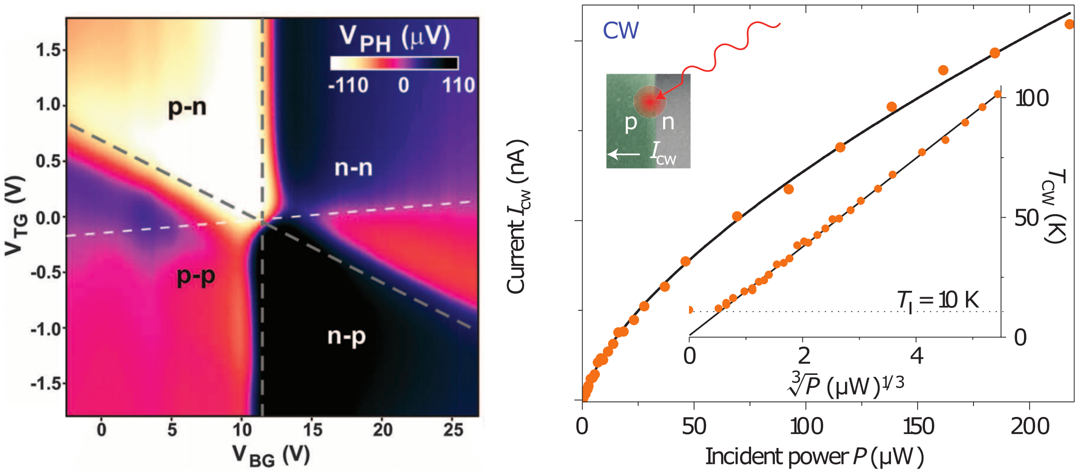

(a) (b)

Figure 4.8: Photothermoelectric response of graphene. (a). Photovoltage map as a function of dual gate voltage. Taken from [102]. (b). Photo response obeys the super-collision cooling power law. Taken from [103].

4.5 Impermeability

As for the gas impermeability, Bunch *et al.* have experimentally shown that pristine graphene is impermeable to all gases under ambient conditions [107]. Their experiment was conducted by measuring the volume change of a graphene-sealed and helium-filled SiO_2 micro-chamber over time, which showed a constant leaking behaviour. The leak rate could not be explained by either the gas diffusion through pin holes on graphene or tunnelling through the pristine membrane, but match the leak rate of gas diffusion through the SiO_2 layer. This finding of gas impermeability was supported by further experiments with a detection limit of 10^5 to 10^6 atoms per second [108, 109].

The use of leak SiO_2 curtails the detection limit. A recent study by Sun *et al.* in 2020 pushes the limit to a few atoms per hour for helium and other standard gases by sealing a graphite micro-chamber with graphene [110]. With this exceptional accuracy, they are able to observe that hydrogen gas, although larger than helium in size, shows higher permeability ($\sim$ 1 H_2 per second) across monolayer graphene. This H_2 permeation is attributed to the bond-flipping of surface adsorbed H_2 (in a form of sp^3-bond H adatom) [110]. The flip of bonds is similar to the mechanism of proton transport across graphene, which we will cover in the next section.

Moreover, graphene is impermeable to liquids like water [111], ions (Li^+, Na^+, K^+, Ru^{3+}, Cs^+, Cl^-) [112, 113] and molecules [114] under ambient conditions.

4.6 Proton Conductivity

In 2014, Hu *et al.* demonstrated that protons can penetrate pristine graphene at an unexpectedly fast rate under ambient conditions [5].

In their experiment, a suspended graphene membrane was sandwiched between two Nafion layers and then connected to proton-injecting electrodes; see top-left inset, Fig. 4.9a. Nafion is a good proton conductor, as described before, and it should be noted that its electron conductivity is negligible. Also, multiple characterisation methods were applied to rule out the existence of pinholes and defects on the graphene, which ensures that there are no short circuits for protons to go across the graphene membrane. By applying DC current-voltage (I-V) measurement, the areal proton conductivity of pristine graphene was estimated to be 5 mS cm^{-2} in room temperature, Fig. 4.9b. After decorating the graphene with platinum nanoparticles, the areal conductivity was improved to 20 mS cm^{-2}.

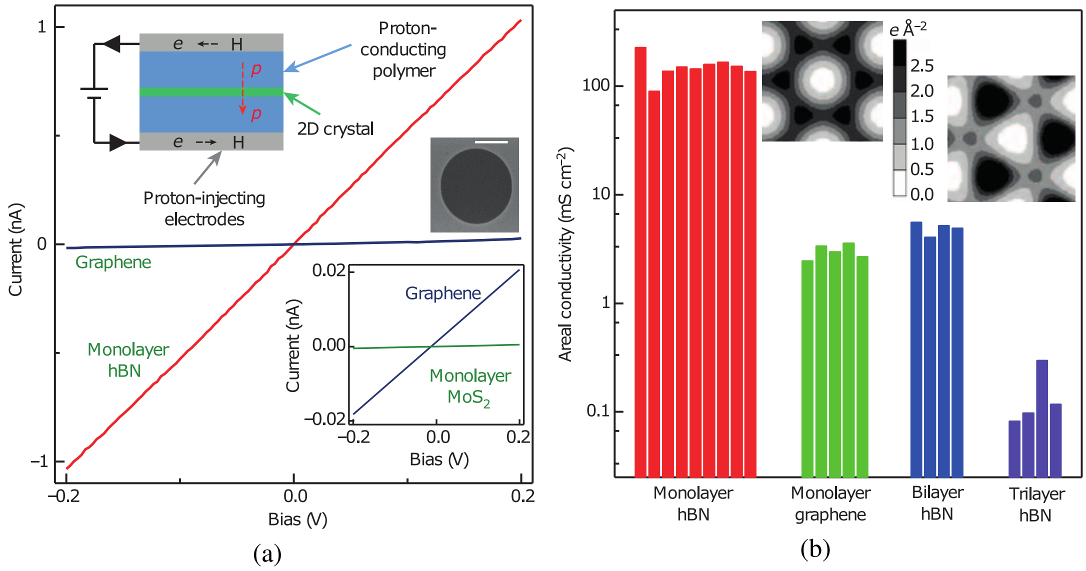

Figure 4.9: Proton transport through 2D crystals. (a) The current-voltage characterisation of different 2D crystals including h-BN, graphene and MoS$_2$. Top inset, device schematic; middle inset, scanning electron micrograph of a suspended graphene membrane; bottom inset, a zoom-in of measurement for MoS$_2$. (b) Areal conductivity for different 2D crystals. Insets, electron cloud density calculation for graphene (left) and h-BN (right). Adapted from Ref. [5].

How does this area conductivity compare to Nafion? The conductivity of high-quality Nafion membranes (for example, Nafion 117) is around 0.1 S·cm^{-1} [115], while the conductivity of a bare-hole device (1 µS conductance, 10 µm aperture and 0.5 µm hole length) used in the experiment is ~ 1 mS·cm^{-1} [5]. The areal conductivity of the bare-hole device is calculated to be ~ 1 S cm $^{-2}$. Therefore the proton conductivity of graphene (with or without Pt decoration) is three orders of magnitude smaller than that of high-quality Nafion.

The proton permeability of graphene is invaluable, considering its impermeability to all other atoms, molecules, ions, and gases — pristine graphene is a perfectly proton-selective membrane [113]. Since Sun *et al.* shown that H_2 molecules are considerably easier to permeate graphene, we may wonder how much will this affect graphene's ability to reduce hydrogen crossover, for example, in PEM-based cells. Hence it is worthy to compare the rate of H_2 permeation with proton transport across graphene. At a typical bias voltage of 0.1 V, the proton current through pristine graphene is about 20 protons per second per nm^2 [5], while for H_2 this figure is $\sim 2 \times 10^{-8}$ s$^{-1} \cdot$nm^{-2} at 1 bar H_2 pressure [110]. Notice that the hydrogen permeation in Nafion is ~ 20 s$^{-1} \cdot$nm^{-2} at 1 bar [116], which is a huge difference (nine orders of magnitude) compared with graphene. For other gasses, such as N_2 and O_2, the permeation difference is even larger. With graphene, one can reduce the H_2 and O_2 crossover to a negligible label while still getting fast proton-transport ability.

The mechanism of proton transport through graphene is different from the proton hopping mechanism in the hydrogen bond network introduced in Section 3.2.1. Although graphene presents dense 2D electron cloud barriers, protons could tunnel through the electron cloud vacancy at an unexpectedly fast rate; see inset, Figure 4.9b. In Ref. [5], proton conductivities of different two-dimensional (2D) crystals other graphene were measured. The differences in their conductivity were linked to the different sizes of the 2D crystals' electron cloud vacancies. The vacancy size determines an activation energy barrier for proton transport through 2D crystals [5, 117]. The activation energy can be calculated by Arrhenius measurement according to the relationship between areal conductivity (σ) and temperature (T): $\sigma \propto \exp(-E/k_BT)$.

Experimentally, it was found that the activation energy is ~ 0.78 eV for protons to permeate through graphene [5]. This marks for the failure of the previous theoretical research that predicted activation energies of 1.25–1.40 eV [118–120]. The large difference between experiment and theory is understandable since the protons and graphene were assumed in a vacuum [118–120], while in the experiment, they are in a much more complicated environment, surrounded by water molecules and Nafion polymers [5].

Luckily, more experimental results in [5] show that the theoretical model did not fail entirely and at least could explain the finding qualitatively. Correlative experiments were performed on other 2D materials, such as hexagonal boron nitride, and on Pt-decorated 2D materials. The change of activation energy in these experiments all matches well with the theoretical calculation. It is thus suggested that the activation energy decreases from what it would be in the vacuum condition to a lower level with the presence of solvents, Nafion, and platinum [5]. A later report on the isotope effect in proton transport shown that the differences of activation energies of hydrogen isotopes again agreed with simulation, which indicates that the zero-point energy of hydrogen bonding with surrounding chemicals also reduces the effective energy barrier [117]. As shown in Fig. 4.10, the effective energy barrier is determined by the zero-point energy of hydrogen (E_H and E_D), and the height of 2D crystal energy barrier that is subjected to the structure of 2D material and its surroundings.

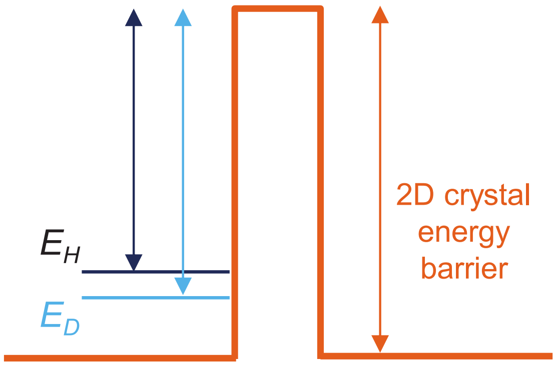

Figure 4.10: Schematic of the energy barrier for proton transport. From ref. [117].

To date, a considerable amount of theoretical research has been trying to explain the mechanism for the lowered 2D barrier [121–124] and full consensus on the topic has not been reached [125, 126].

Few early studies suspect that atomic defects naturally present in graphene could be the reason for the proton permeation [127, 128]. Achtyl *et al.* studied fused silica covered with graphene that was subjected to cycles of low and high pH [127]. It is shown that acid-base chemistry of the silica was not hindered by graphene at all, indicating fast protons permeation through graphene. Reference [128] reported transport experiments in aqueous HCl electrolytes but using CVD graphene. Their results showed proton conductivity orders of magnitude larger than pristine graphene studied later in similar conditions [113], and small membrane potential (< 10 mV) in pH differential measurement that indicates only minimal proton selectivity [128].

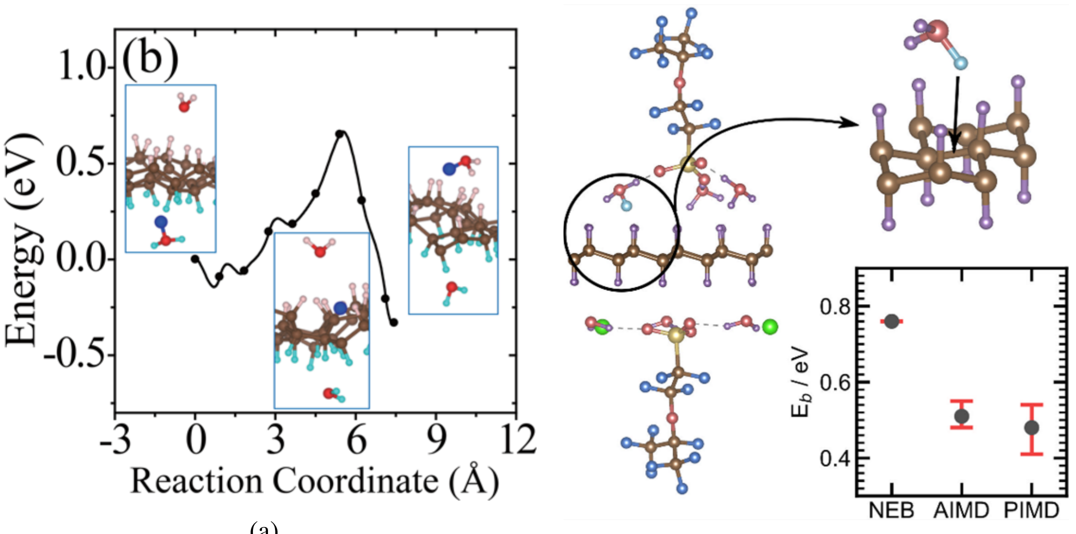

(a)

(b)

Figure 4.11: Proton transport across fully hydrogenated graphene. (a) Energy profile. Insets are molecular configurations for the reactant, transition, and product stages. O (H, C) atoms are presented as red (pink, brown) balls. Blue balls are protons. Cyan balls: H adatoms below the sheet. Taken from Ref. [121]. (b) Left: molecular configuration of water-Nafion-graphane complex. Top right: zoom-in. Bottom left: estimated energy barriers by different calculation methods. The violet, brown, red, blue, yellow and green balls represent H, C, O, F, S, and Cl atoms, respectively. Taken from Ref. [124].

Both experiments in [127, 128] used CVD graphene instead of pristine graphene [113]. Indeed, CVD graphene membranes are known to be abundant with atomic defects, and even macroscopic ones [113, 127]. In this case, the proton transport should be dominated by defects. Theoretical calculation on graphene with atomic defects [127] found activation energy barriers close to those measured in [5]. However, in stark contrast, aqueous experiments on pristine graphene show perfect proton selectivity and 2-3 orders of magnitude smaller proton conductivity than CVD graphene [113]. All these indicate that proton transport through pristine graphene is different from those of CVD graphene and provide further support for theoretical explantation to proton transport through defect-free graphene [113].

Actually, theoretical progress developed in recent years has brought more insights into understanding proton transfer through pristine graphene. Several ab initio studies have shown that hydrogenation of graphene could facilitate the proton transfer barrier [121, 122]. Figure 4.11a shows a typical energy profile and corresponding molecular configuration for this mechanism. It is reasonable to assume that partial hydrogenation of a micro-scale graphene sheet could happen in aqueous solutions at an external bias, which was also demonstrated to be a reversible process by a recent experiment [129]. Their simulations were based on fully hydrogenated (within a nano-scale simulation box) graphene surrounded by water molecules, yielding activation barriers of ~ 0.6 eV [121, 122]. These works also verified the zero-point energy contribution to the isotope effect. A more recent theoretical calculation simulating fully hydrogenated graphene in Nafion-water environments, which is closer to the realistic conditions, shown consistent results with the above works [124]; see Fig. 4.11b.

Bond flipping of hydrogen adatom could be the main mechanism when protons actually transfer across graphene, though in this study, the authors argued that hydrogen adsorption on graphene would lead to a stable chemisorption state of proton, thus higher energy barriers (> 3 eV) [126]. It was later shown by Bartolomei *et al.* that

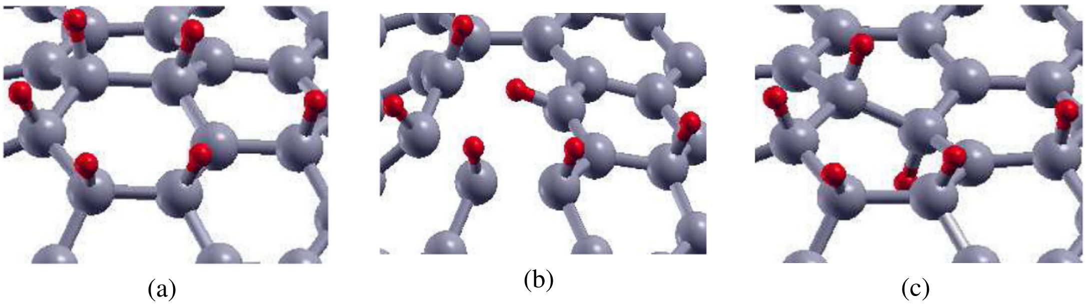
(a) (b) (c)

Figure 4.12: Proton-flipping mechanism for multi-protonation of a graphene sheet. The protonation number is five. Grey balls: carbon atoms. Red: hydrogen. (a) Reactant configuration with five protons adsorbed on a carbon ring. (b) Transition state configuration showing that a flipping proton is inserted in between two adjacent carbon atoms. (b) Product configuration showing the proton flips to the other side of the carbon ring. Taken from Ref. [123].

multi-protonation would lead to a considerably lower energy barrier (~ 1 eV) for bond flipping [123], if there is a hydrogen adatom near the flipping one. A schematic of such a mechanism is shown in Fig. 4.12. With a relatively low-barrier transfer from in-water protons to chemisorbed hydrogen on graphene, the multi-protonation flipping could be a determining process for proton transport across graphene. Take these together with other factors that could reduce the effective barrier, including zero-point effect [124], quantum-nuclear tunnelling [130], bias potential effect [5, 117], and ripple/strain [110], the experimental determined unexpectedly low activation energy now becomes a reasonable value.

Apart from the above investigation, another finding is that proton transport through graphene is sensitive to light [131]. Under illumination, the conductivity of Pt-decorated graphene is improved by a factor of ~ 10. A photoresponsivity of $\sim 1 \times 10^4$ $\mathrm{A} \cdot \mathrm{W}^{-1}$ was reported with a response time in the µs range. The device also showed a high sensitivity with a noise-equivalent power of 10^{-14}-10^{-16} W $\mathrm{Hz}^{1/2}$. These figures of merit are comparable to monolayer MoS_2 and conventional silicon photodiodes.

It was suggested that a localised photovoltage was generated around the nanoparticles sitting on graphene due to the hot electron generation under light excitation [131].

For nanoparticles like Pt that n-dopes graphene, the photovoltage helped to drive protons towards the nanoparticles, where protons and electrons form hydrogen gases, so that the proton current was increased. This explanation agrees with the experimental observations. A direct evidence is that the light power dependence of the photon-proton effect follows the power law observed in the PTE experiments, as we have introduced in Section 4.4. However, undeniably, further experiments/theories are still needed to better understand the mechanism of this photon-proton effect.

Chapter 5

Experimental techniques

In this chapter, we describe the experimental techniques used in this thesis. The techniques include fabrication processes to suspend single-layer graphene membranes, drop-cast cation-conducting polymer membranes, and assemble contacts and electrodes with devices for measurement. Methods for measuring electrical properties, mass-transport properties, and photo-proton effect are described.

Contributions

My contributions to the experimental techniques in this chapter include: improved methods to efficiently fabricate substrates in wafer scale (see Page 93), developed and optimised methods to fabricate Fumion layer on suspended graphene membranes (see Sec. 5.1.5), developed a LabVIEW potentiostat programme based on a Keithley sourcemeter to perform three-electrode measurement (see Fig. 5.10), designed and developed the experimental setup for oxygen flux measurement (Sec. 5.2.3). Other techniques described in this chapter are based on the previous works of our group with only minor modifications.

5.1 Device fabrication

Let us start with the typical geometry of the devices we fabricated and measured in this thesis. A schematic of the device can be found in Fig. 5.1. Graphene flakes are suspended on a through-hole fabricated in silicon nitride substrate (SiNx). The graphene flakes are decorated with Platinum (Pt) nanoparticles on the top side and cover the gold electrodes micro-fabricated on the substrates. In this way, the suspended graphene itself serves as an electrode. The other side of the graphene flake is contacted with cation-conducting polymer membranes (Fumion FAA-3-SOLUT-10, FuMA-Tech) and then attached with a porous carbon electrode (carbon cloth with Pt catalyst loading of 0.2 $\mathrm{mg \cdot cm^{-2}}$). These form the typical two-electrode structure of the devices we made. The fabrication methods for the suspended graphene membrane are based on the previous works of our group (see methods in [5, 131, 132]). The detailed fabrication processes will be described step-by-step in the following subsections.

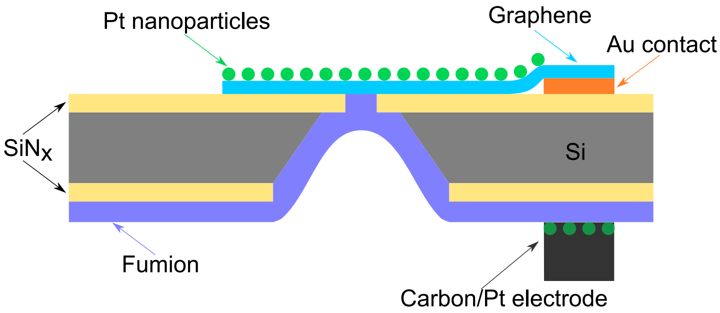

Figure 5.1: Schematic of the device of suspended graphene membrane for photoeffect measurement.

5.1.1 Substrate preparation

To suspend the graphene membrane, a perforated substrate is needed. We start with double-side CVD-coated Si/SiNx wafers with a typical thickness of 500 µm/500 nm. The SiNx substrate was chosen for its electrical insulating nature and good impermeability to all gases and liquids. Moreover, the SiNx proves to be a good mask for silicon

KOH wet etching to create through-holes across the silicon substrates.

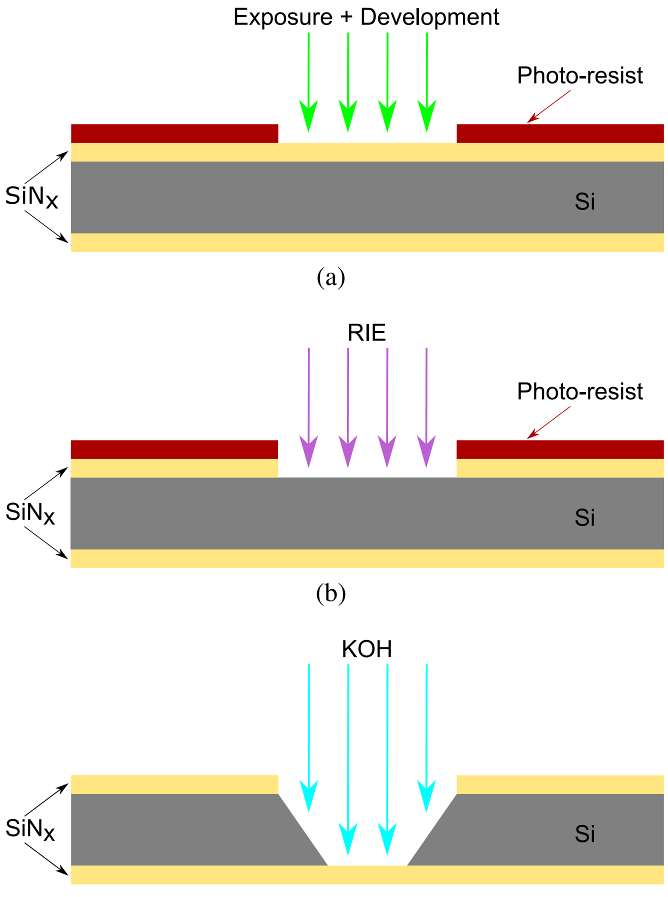

(a)

(b)

(c)

Figure 5.2: Etching of silicon substrate to suspend SiNx. Pattening (a). and etching (b). of the SiNx mask; (c). KOH etching of silicon substrate.

Firstly, a SiNx mask is prepared on one side of the substrate. The windows on the mask are patterned by photolithography (Fig. 5.2a) and opened up by reactive ion etching (RIE, Fig. 5.2b). A Microtech laser writer (LW405) is used to pattern a photoresist mask such that most of the SiNx layer is protected except for a 0.8-mm-by-0.8-mm square window. This can be done on a wafer scale by exposing a square array of such patterns with a typical pattern separation of 1 to 2 cm, to open up windows for multiple substrates.

The typical photolithography process is as follow. A Microposit S1813 positive-tone photoresist is spun onto the Si/SiNx wafer with a spin speed of 3000 rpm for 60 s. The photoresist layer is then baked on a hotplate at 110 $C^{\circ}$for 60 s, which results in a cross-linked 1.3-µm layer of S1813 resist. After being exposed in the laser writer, the cross-linking in the exposed region is broken, and a Microposit MF319 solution is then used to develop the pattern. The development is done by immersing the wafer in the MF319 solution for 30 s to remove the exposed photoresist. After that, deionised water is used to clean the MF319 solution from the wafer to stop the developing process.

Then the resist-patterned side of the SiNx wafer is etched using an RIE system (Oxford Plasmalab System 100). An RIE system incorporates both physical plasma etching (removal with kinetic energy) and chemical plasma etching (with reactive ions, typically using SF_6 on silicon nitride). RIE is a powerful dry etching technique that can achieve highly directional etching (less undercut) with relatively high cleanness. The System 100 RIE uses a combination of parallel plates and inductively coupled plasma (ICP) RIE. Samples are placed on an electrically isolated sample holder that situates between the parallel plates. In the ICP scheme, a low-pressure gas mixture turns into plasma in a strong electromagnetic field oscillating at radio frequency (RF). During the whole etching process, the gas flow is controlled to maintain the vacuum in the RIE chamber and to keep the plasma ignited. In the meantime, the ICP-ignited plasma is guided by a strong direct-current (DC) electric field between the parallel plates to attack the samples.

In our recipe, the plasma is generated with a $O_2/Ar/SF_6/CHF_3$ gases mixture. The chemical removal of atoms in the SiNx layer is described by the following chemical equations [133]:

$$\mathrm{Si_3N_4\,(s) + 3\,SF_6\,(g) \longrightarrow 3\,SiF_4\,(g) + 3\,SF_2\,(g) + 2\,N_2\,(g)}$$

$$Si_3N_4\,(s) + 4\,CHF_3\,(g) + 5\,O_2(g) \longrightarrow 3\,SiF_4\,(g) + 4\,CO_2\,(g) + 2\,H_2O\,(g) + 2\,N_2\,(g)$$

The photoresist mask is also etched but with a much lower etching rate compared with SiNx because the etching of photoresist involves mainly the physical bombardment from the plasma. The etching rate of SiNx in our recipe is about 4 nm/s and the selectivity (ratio between SiNx and S1813) is 1:15. After the RIE process, the window area of the SiNx layer is etched, and the underlying silicon is exposed, while the other area of the SiNx layer are protected by the mask. The remnant photoresists are removed by rinsing in acetone.

Our total etching time is typically 3 minutes on a sample scale (only a few windows) and 4 minutes on a wafer scale. The prolonged etching on a wafer scale is to overcome the inhomogeneity of the System 100 RIE — the etching rate near the edge area of the wafer is lower than that in the central area. Although there is a built-in nitrogen temperature control system to cool the sample plate in the System 100 RIE, a continuous etching of over 3 minutes could still cause burning of the photoresist, as the photoresist is bombarded by the energetic plasma. This usually leads to persistent photoresist contaminations that are hard to remove using standard solvents like acetone. Thus, the etching process is usually broken down into several etching cycles, each followed by a ramping-down cycle in which the etching is ceased to allow the wafer to cool down.

Once the SiNx mask is prepared, we use the wet-etching technique to fabricate a through-hole in the silicon layer. Potassium hydroxide (KOH) solution is chosen to be the etchant. The etching process is guided by the following chemical equation:

$$Si\,(s) + 2\,OH^-\,(aq) + 2\,H_2O\,(l) \longrightarrow Si(OH)_4{}^{2-}\,(aq) + H_2\,(g)$$

SiNx is a perfect mask for etching silicon with KOH, as the selectivity (etching rate

Si:SiNx) is at least a few thousand (for PECVD SiNx).

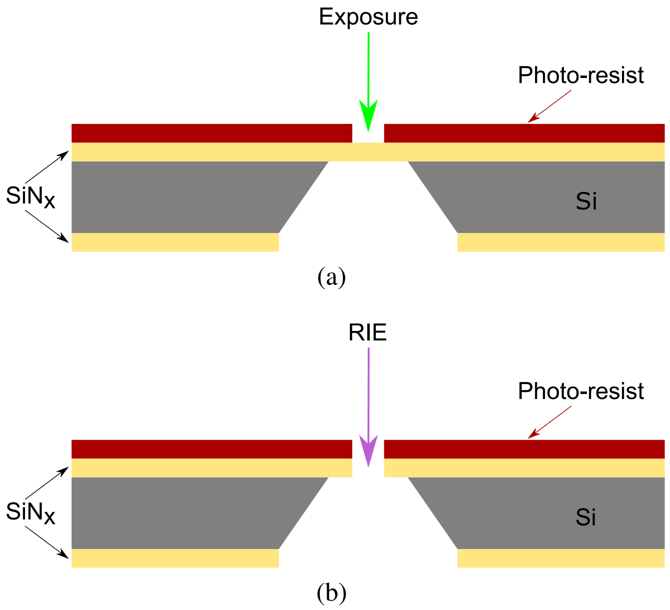

(a)

(b)

Figure 5.3: Completing through-holes. (a). Patterning, and (b). etching the suspended SiNx.

The KOH etching of silicon is anisotropic — the etching rate of silicon is dependent on its crystallographic orientation [134]. The etching rate of $\{111\}$ plane is much slower than the rate on the planes $\{100\}$ and $\{110\}$ with a ratio around 1:500. Typically, the $\{100\}$ plane is aligned with the wafer plane, so the etching goes perpendicularly through the wafer plane. The wet etching process results in a tapered square hole with a side angle of $\sim 54.74^\circ$ ($\tan^{-1}\sqrt{2}$) as shown in Fig. 5.2c. The etching rate becomes slow after etching through the 500 μm silicon layer and reaching the SiNx on the other side because there is now only $\{111\}$ plane exposed. This creates a suspended and square-shaped SiNx layer. The other case is that the two $\{111\}$ planes intersect, hiding the underlying $\{100\}$ plane, which terminated the etching process with the hole not etched through the Si substrate. To avoid the later case, the window size of the SiNx mask should be large enough. The window size is chosen according to the following calculation. If neglecting the etching of the 111 plane, the size W_2 of the suspended SiNx layer can be easily estimated by

$$W_2 = W_1 - \sqrt{2} Z_{etch}$$

where W_1 is the size of the window in the SiNx mask, and Z_{etch} is the etching depth. With the etching depth being 500 µm, our 0.8-by-0.8 mm window results in a suspended SiNx membrane with a width of ∼100 µm. Besides, due to the etching of {111} plane, there will be an undercut beneath the SiNx mask.

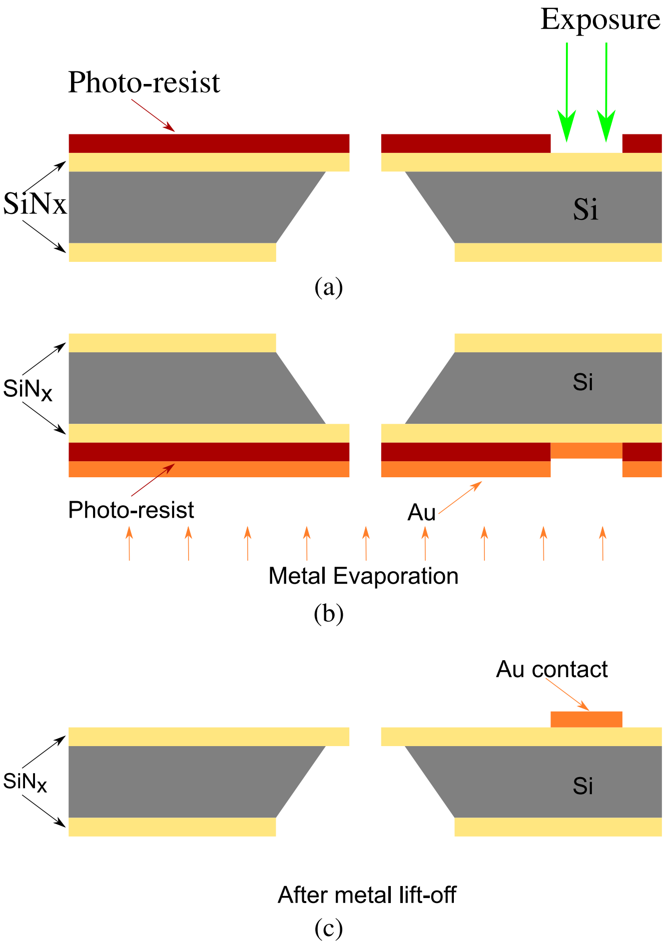

Figure 5.4: Microfabrication of gold contacts. (a). Patterning. (b). Contact deposition. (c) liftoff.

In the wet etching process, we use 30% w/w (wt%) KOH solution. Wafers are immersed in the etchant solution heated with a water bath at temperature 80 C°. The etching rate of Si in this setup is $\sim$80 µm per hour. Thus, a period of 6-7 hours is required to etch through the 500 µm silicon substrate. After the etching process, the wafers are removed from the etchant solution and rinsed in a large amount of deionised water.

The suspended SiNx layer is further patterned and etched to create a vertical circular through-hole with a designated diameter, typically 10 µm, following the same photolithography and RIE processes described above. The processes to fabricate the circular holes are shown in Fig. 5.3.

Finally, gold contacts are fabricated on the substrate. To this end, we use photolithography to pattern the designed electrode area on an S1813 photoresist layer near the circular hole (Fig. 5.4a). Then, electron beam physical vapour deposition (Moorfield e-beam evaporator) is used to deposit the electrode. In an e-beam evaporator, a high energy electron beam bombards the target metal reservoirs and turns the metal into the liquid phase in a vacuum chamber. Atoms from the target are further transformed to metal vapour by the electron beam. The metal vapour precipitates into a thin layer covering the whole chamber, as well as the sample. In our recipe, a 2-nm chromium layer and a 40-nm gold layer are deposited on the substrate (Fig. 5.4b). The chromium layer is necessary to make gold easier to adhere to the substrate. After this, a lift-off process is performed by dissolving the photoresist layer in acetone, which leaves the gold contacts on the substrate (Fig. 5.4c). At this point, the substrate fabrication process is finished.

The above processes, from photolithography to electrode growth, except the final lift-off, can be done on a wafer scale. These wafer-scale lithography processes were developed and optimised by the author of this thesis, using the standard pattern alignment of the laser writer (LW405). Instead of using the array patterning functionality (typically used for exposure parameter optimisation) of the laser writer, our method uses a wafer-scale design file with an array of multiple substrate designs. By carefully choosing the alignment points in the design array, we can perform multiple photolithography processes on a wafer, correctly overlapping features in different design layers. Compared with other techniques for wafer-scale lithography, such as using a mask aligner, our method does not require the fabrication of expensive masks, and is more flexible.

5.1.2 Graphene preparation

5.1.2.1 Mechanical Exfoliation

Graphene flakes in this thesis are exfoliated using mechanical cleavage. The process starts with pressing a piece of natural graphite (single crystal) onto a piece of adhesive tape. After that, the graphite bulk is removed from the tape, with several graphite flakes remain on it. Then the tape is peeled — folded, pressed against itself, and released — repeatedly. Because of the graphite's layered nature, the repeated peeling thins the graphite flakes. Then a SiO_2/Si substrate (290 nm/500 µm) is prepared. The substrate is O_2/Ar plasma cleaned using a Moorfield nanoETCH etcher. Immediately after that, the thinned graphite flakes on the adhesive tape are pressed onto the substrate. The plasma etching removes water and hydrocarbon contamination on the substrate to increase the adhesion between graphite and the substrate. The tape is then removed, and some flakes are left on the SiO_2 substrate. The flakes are further examined using the techniques described later to identify monolayer graphene.

5.1.2.2 Identifying Monolayer Graphene

Optical microscopy is the handiest approach to distinguish graphene flakes of different thickness/layers on SiO_2. The oxide/Si and oxide/air interfaces reflect a rainbow of visible lights. Layers of graphene flakes on SiO_2 layer tune the interference of the reflected light and provide enough visible contrast [135]. With a little training, graphene monolayers can be easily distinguished from the multilayers under an optical microscope by bare eyes.

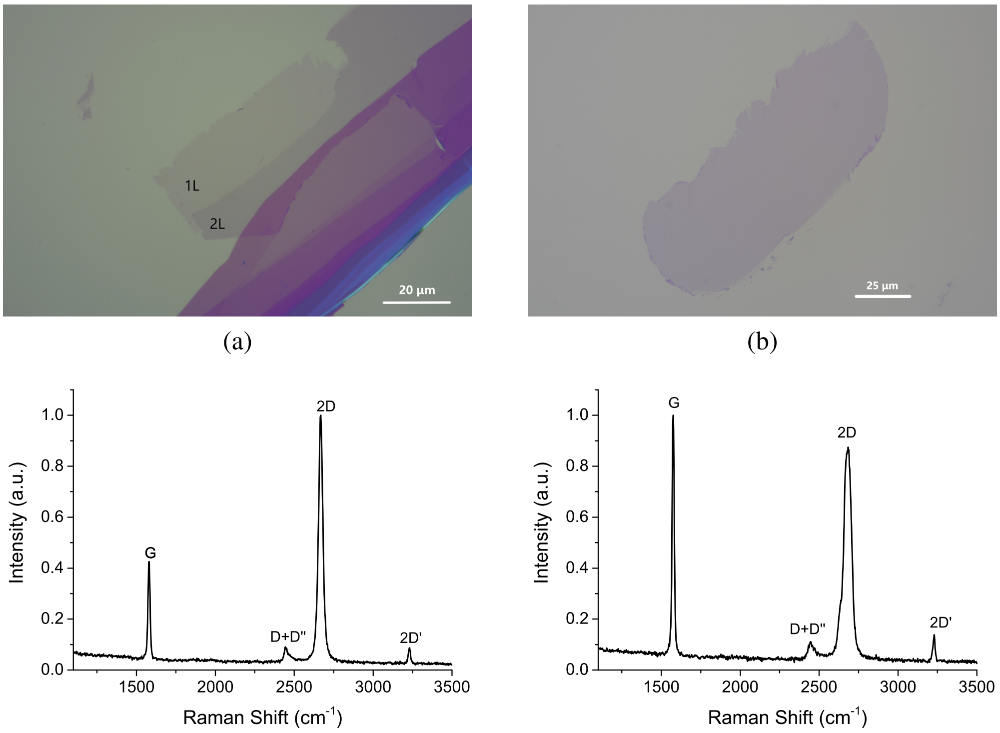

(a) (b)

(c) (d)

Figure 5.5: Examples of graphene flakes and Raman characterisation results. (a). and (b)., two graphenes flake on SiO_2 substrate. Labels in (a) indicate monolayer and bilayer. The Raman response of the monolayer (d) and bilayer (d) graphene shown in (a).

As an example, we show two optical images of the graphene flakes on SiO_2 substrates in Fig. 5.5a and Fig. 5.5b.

Although optical microscopy is a rapid and frequently used method in searching for monolayers and multilayers of two-dimensional materials, other characterisation techniques should be used together to accurately identify the thickness of graphene.

Let us take Raman spectroscopy, which is a commonly used non-invasive characterisation method, as an example [136]. Figure 5.5c and 5.5d show the Raman responses of the single-layer and bilayer areas of the flake (Fig. 5.5a), respectively. The signal was measured using a Horiba Raman spectroscopy system.

The Raman spectrum of graphene has two main peaks: the 2D peak at $\sim$2700 cm^{-1} and the G peak at $\sim$1580 cm^{-1}. The relative intensity of the G and the 2D peak is an indicator to distinguish monolayer graphene from multilayers. This can be seen from the I(G)/I(2D) ratio changing from $\sim$0.5 (Fig. 5.5c) to >1 (Fig. 5.5d). Another feature is the line profile of the 2D peak. For single-layer graphene, the 2D peak has a Lorentzian profile. As the layer number increases, the 2D peak broadens with another peak arising, and the position of the 2D peak up-shifted. When there are defects like vacancies and adatoms, another feature at $\sim$ 1350 cm^{-1} known as D peak can be observed. Only flakes with no D peak are used to make our suspended device.

5.1.3 Graphene transfer method

After characterising the monolayer graphene flakes, the flakes are transferred onto the perforated SiNx substrates. For graphene flakes on SiO_2 substrates, a wet transfer method is used in this thesis [137]. The process is depicted in Fig. 5.6.

A layer of Poly(methyl methacrylate) (PMMA) is spin-coated onto a graphene flake, followed by hotplate baking, forming a PMMA membrane. Then the PMMA-coated substrate is put in a KOH solution. The KOH attacks the SiO_2 layer, and as the oxide layer is etched away, the PMMA membrane is released from the substrate. Because of the adhesion between Graphene and PMMA, the graphene flakes are transferred onto the PMMA membrane. Next, the PMMA membrane is handled by a three-dimensional precision translation stage. With the help of an optical alignment system, the flake is precisely placed onto a SiNx substrate to cover the holes and gold contacts on the substrate. The sample is then baked at 100 C°on a hot plate for 10 minutes to increase the binding between the flake and substrate. The next step is to dissolve the PMMA on the sample. The sample is emersed in acetone and allowed standing for 10 minutes to dissolve PMMA. Then the sample is transferred carefully into fresh acetone and stay for one minute to remove the dissolved PMMA to reduce contaminations. Note that the sample is not allowed to dry during the transfer.

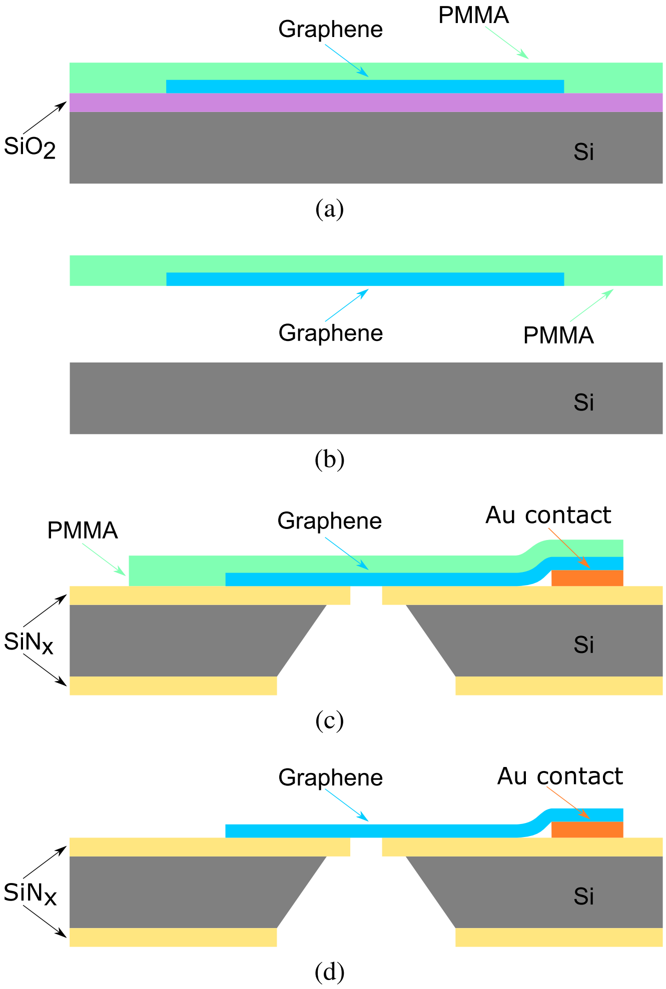

Figure 5.6: Graphene wet transfer. (a). PMMA coating. (b). SiO_2 etching. (c). Graphene transfer. (d). Dissolving PMMA.

Last, the sample should be carefully dried. This step is crucial because the shear force created during evaporation by the surface tension of solvent droplets sitting on the unsupported graphene flake is highly possible to create breaches on the flake. Two approaches are typically used to finish this step. One is to exchange the acetone with hexane which evaporates rapidly in the atmosphere and has small surface tension [138]. This reduces the probability to damage the suspended graphene membrane. The sample (in acetone) needs to be carefully transferred into hexane, without drying in the process. After standing in hexane for 30 seconds, the sample can be slowly taken out of hexane and allowed to dry in air.

The other method is to remove the acetone using a critical point dryer [139]. In the critical point dryer, the acetone is exchanged by a highly pressurised CO_2 liquid. The CO_2 liquid is further heated to above its critical point where there is no boundary between gas and liquid state, thus nearly no surface tension, and finally, the CO_2 is extracted as gas. The critical point dryer can further increase the yield of suspended graphene membranes. So far, the core of the device, the suspended graphene membrane, has been made, and it is contacted with a gold electrode on one side. However, to ensure there are proton/hydrogen pathways for proton transport measurement, a few more steps are needed.

5.1.4 Catalyst Deposition

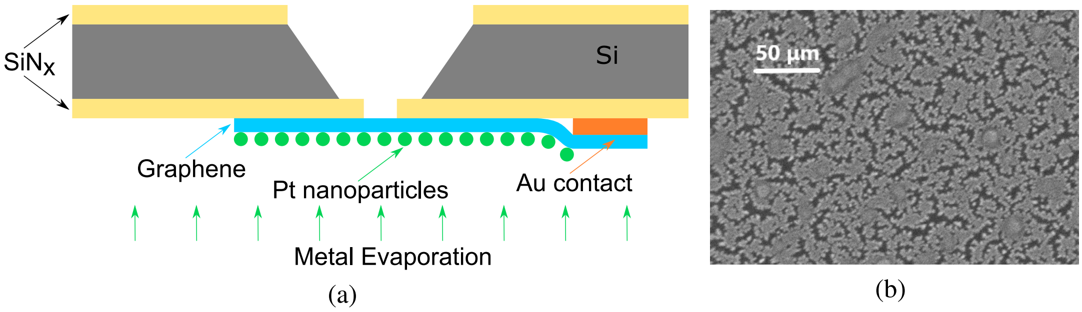

(a) (b)

Figure 5.7: Catalyst deposition. (a). Pt nanoparticles deposition. (b). SEM image of Pt nanoparticles on suspended graphene.

On the gold contact side, a 2-nm (nominal) platinum layer is deposited on the graphene by e-beam evaporation (AJA E-beam Evaporator), as shown in Fig. 5.7a. The layer consists of discontinuous Pt nanoparticles. The Pt nanoparticles deposited on the graphene membrane serve as catalysts to reduce protons into hydrogen gases.

5.1.5 Final Assembly

On the other side of the membrane, we drop-cast an anion-exchanging ionomer solution (Fumion FAA-3-SOLUT-10, FuMA-Tech) over the through-hole. The solvent in the ionomer solution evaporated in ambient conditions, leaving a thin polymer layer on the substrate (Fig. 5.8a).

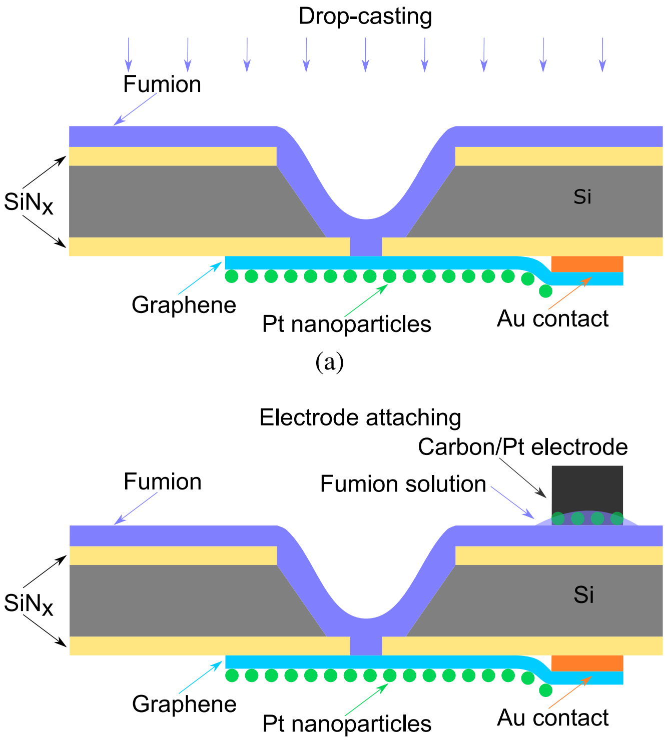

(a)

(b)

Figure 5.8: Final assembly. (a). Polymer drop-casting. (b). Mechanically attaching of carbon/Pt electrode.

Next, a porous carbon electrode (carbon cloth with Pt catalyst loading of $0.2\ \mathrm{mg} \cdot \mathrm{cm}^{-2}$ is mechanically attached to the polymer using the same ionomer solution as a binder material. Due to the undercut introduced in the silicon wet etching process, the polymer can be pierced by the sharp silicon nitride cantilever edges, which may cause the polymer to detach from the substrate during further processes and reduce the lifetime of devices. This type of device failure was rarely seen for similar devices in our previous works, which using Nafion as the polymer material [5, 131, 132]. Fumion membrane is stiffer and less flexible than Nafion, thus more prone such fault. To overcome this drawback, we applied epoxy resins to the undercut region to cover and protect the polymer. This process needs to be carefully proceeded without blocking the through-hole. Finally, the polymer side is rinsed repeatedly with deionised water and left in deionised water for several hours to remove impurity ions from the polymer. At this point, the device fabrication finishes, and the device is ready for measurement.

5.2 Measurement Techniques

Two categories of measurement techniques are used in this thesis. Electrical properties, such as conductivity and zero-current voltage of the devices, are measured via taking the current-voltage (*I*-*V*) response. Mass transport experiments, including measuring the hydrogen flux and oxygen concentration, are used to monitor the generation of gas products directly and simultaneously alongside the electrical measurement.

5.2.1 Electrical measurements

The *I*-*V* response in our experiments is measured by sourcing voltage and measuring current using a Keithley's SourceMeter 2636A. A home-made PTFE cell for holding KOH or KCl solutions (typically 1 mL volume) with electrolyte concentrations of 10^{-5} M to 0.1 M is attached to the devices. The device and the cell are sealed by a gasket made from double-side adhesive silicone sheets (Grace Bio-Labs, Press-To-Seal, 0.8 mm). A light source (a calibrated Newport Oriel Sol3A solar simulator) is used

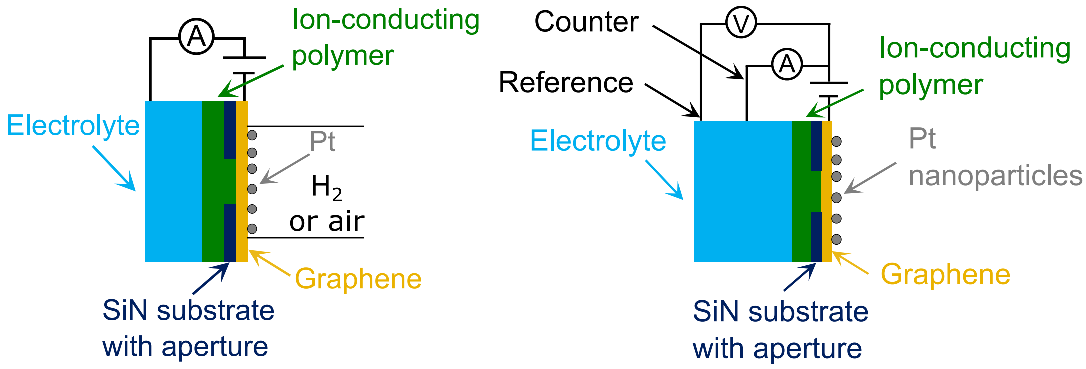

(a) (b)

Figure 5.9: Schematic of experimental setup for electrical conductivity measurement.(a) Two-terminal geometry and (b) three-terminal geometry.

to provide simulated solar illumination to the devices. The solar simulator's aperture diaphragm is used to adjust the light intensity from 0.7 $\mathrm{mW \cdot cm^{-2}}$ to 100 $\mathrm{mW \cdot cm^{-2}}$.

For low bias measurements (linear regime), the applied voltage is scanned between ± 200 mV around the zero-current voltage (ZCV) at a sweep rate of 0.01 $\mathrm{V \cdot min^{-1}}$. The electrical conductivity is then calculated from the slope of I-V curves.

ZCV can be extracted from the x-intercept of I-V curves from low-bias measurements. However, for a more precise ZCV measurement, the current flow through the devices is set to zero and voltage is measured over time until the voltage stabilises.

For measurements at larger bias, we apply a fixed voltage to our devices, measure current continuously, and then illuminate the devices with one-minute on/off light pulses. The on/off pulses are repeated several times for each to ensure reproducibility.

The schematics of two different electrical measurement setups are shown in Fig. 5.9. The two-electrode geometry (Fig. 5.9b) described above (porous carbon electrodes) are simple to set up. Because of its large size compared to the graphene electrode, The electrolyte resistance of a cell with a micro-electrode can be neglected. The voltage drop measured between the two electrodes is mainly accounted for the potential across graphene and the electrode potential of the porous carbon. Factors such as mass-transport resistance do not contribute to the voltage either. Hence, the carbon/Pt electrode acts as a pseudo-reference electrode and allows for stable measurements of the potential and ZCV.

The three-electrode measurement uses an additional standard silver-chloride reference electrode, as depicted in Fig. 5.9b. This geometry aims to get potential values that can be transformed to the standard Hydrogen reference potential, an electrochemical standard. In chemistry terms, the graphene electrode is now a working electrode, and the porous carbon electrode is called a counter electrode. Besides the different electrode potentials, this geometry differs in that the Ag/AgCl electrode is in direct contact with the hydroxide solution rather than with the polymer, which creates a liquid junction at the salt-bridge/solution interface.

On top of that, *I*-*V* measurement using the three-terminal geometry requires the current flow between the reference electrode and each one of the other electrodes to be zero. Typically, a potentiostat is needed to ensure the zero-current restraint. An operational amplifier is responsible for the cut-off of current flow. For the current response of the cell under a specific potential to be measured, the operational amplifier circuit controls the potential of the working electrode to be the desired value (specified by the voltage input) with respect to the reference electrode by adjusting the current flow between the working electrode and the counter electrode.

In this thesis, we replaced the operational amplifier with a software controller. Two channels of the Keithley 2636A sourcemeter are used as a voltmeter and a current source, respectively. Channel operating in voltmeter mode allows no current flow through the reference electrode. A LabVIEW programme was developed by the author of this thesis to control the sourcemeter, essentially turning the sourcemeter into a software potentiostat. The programme uses a software PID control loop to keep the potential of the working electrode as desired, by tuning the current flow across the cell via the current source channel. The programme provides an graphical interface for users to manually input the required working electrode potential, and allows automatic

Potential channel Channel A
Set Potential 0
Actual Potential 0
Min Set P -1
Max Set P 3
Cell channel Channel A
Compliance (A) 2
Cell Voltage (PID) 0
Min CV 0
Max CV 3

PID gains
proportional gain (Kc) 0.5
integral time (Ti, min) 0.001
derivative time (Td, min) 0

Voltage Sweep **Min** 0 **Volt Step (Volt)** 0.01 **Max** 3
Current loop No 1
Delay Time (s) 1
No of loops 1
Delay Time (s) before 5
Ramp **Strat From** Min **Ramp Step (Volt)** 0.1 **Ramp Delay Time (s)** 1

Figure 5.10: The user interface of the home-developed software potentiostat. The programme was developed using LabVIEW.

potential sweep to perform three-electrode *I*-*V* measurement (see Fig. 5.10).

5.2.2 Hydrogen mass spectroscopy

The hydrogen flow was measured using a mass spectrometer (Inficon UL200 Leak Detector). Similar experimental setup was used in the previous works of our group [5, 131]. The leak detector is able to measure the flux of gases with 2, 3, and 4 relative molecular mass. A schematic of the experimental setup is shown in Fig. 5.11. Devices of size 1-by-1 cm are glued by epoxy to a perforated thin copper foil plate. The aperture on the plate ensures that the devices are not blocked. The plate here works as an adaptor for our devices to fit into a chamber connected with the mass spectrometer and a vacuum pump. Devices are clamped to the chamber with an O-ring, which separates the chamber from the atmosphere. The Pt-decorated side of the device faces the inside of the chamber. The chamber is then evacuated by a vacuum pump before measurement.

Before the hydrogen flow test can proceed, We check the airtightness of membranes and the sealing of devices in the chamber. To this end, the leak detector is set in helium-detecting mode, and a suitable amount of helium gas is released near the device. The

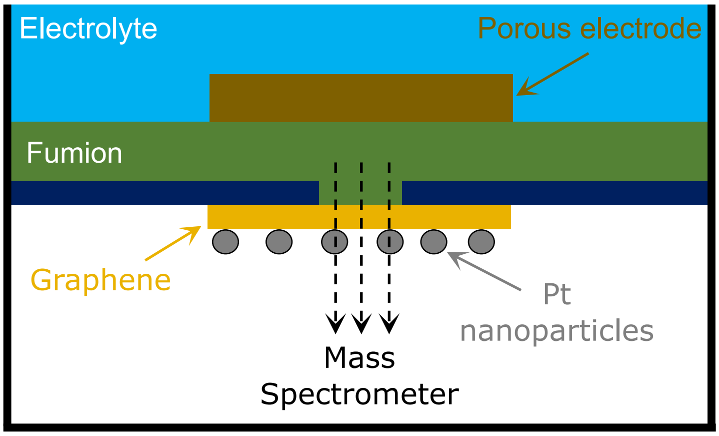

Figure 5.11: Experimental setup for hydrogen gas flux measurement.

read-out in the leak detector should stay at the background level ($\sim 10^{-8}$ bar cm^3/s). Otherwise, the setup is leaky.

Alternatively, a complete setup can be used to measure the leak rate of the device more precisely. The device is clamped between two chambers in this setup. One chamber is filled with helium gas, and the other one is evacuated and connected with the leak detector. The leak rate should stay at the background level with the helium chamber pressure up to $\sim$ 1 bar. Then we can ensure the airtightness of the device. Otherwise, a noticeable leak rate will arise with the increasing helium pressure if the device is leaky.

After confirming the airtightness of the setup, the top side of the device is filled with KOH solutions. Neither a zero bias nor a positive bias applied to graphene results in detectable hydrogen flux signals. Only under the right polarity (negative voltage bias), hydrogen gas can be generated on the graphene surface from protons transporting across the graphene. The hydrogen flux and the electric current can then be measured simultaneously.

5.2.3 Oxygen flux measurement

The oxygen flux measurement techniques were developed by the author of this thesis, which is based on an oxygen concentration sensor. The design of the experimental setup (Fig. 5.12) was inspired by works that measure oxygen concentration [140, 141].

A Clark-type oxygen sensor (OX-NP, purchased from UNISENSE CO., LTD.) is used to measure the concentration of dissolved oxygen in the electrolytes. The numerical derivative of the oxygen concentration against time is calculated for the oxygen flux.

A schematic of the oxygen sensor used in this thesis is displayed in Fig. 5.12a [142]. The basic structure of the oxygen sensor is an oxygen-reducing electrode, known as the sensing cathode, which is polarised against an internal Ag/AgCl electrode. The oxygen reducing reaction is given by

$$\mathrm{O_2\,(g) + 2\,H_2O\,(l) + 4\,e^- \longrightarrow 4\,OH^-\,(aq)} \tag{5.1}$$

The rate of this reaction is dependent on the oxygen concentration near the cathode, which is converted to current passing between the sensing cathode and an Ag/AgCl reference electrode. The sensing cathode is a glass-coated platinum wire with a porous gold tip [142]. It consumes only a negligible amount of oxygen, which accurately quantifies the oxygen concentration near the electrode.

The sensing cathode is placed at the tip of the sensor near a silicon membrane. The silicone membrane is impermeable to all ions and highly permeate to gases[143]. This creates a chamber acting as a stable electrolyte reservoir for the electrodes. The diffusion of oxygen through the membrane is then be detected by the sensing cathode. The sensor also contains a guard cathode to get rid of the oxygen already dissolved in the chamber. The guard cathode is essentially a large oxygen-reducing electrode that effectively consumes oxygen in the electrolyte. This guard cathode minimises the zero-oxygen current and increases the responding time of the sensor [142].

During operation, the potential of the sensing cathode is polarised at -0.8 V against the Ag/AgCl reference electrode. This produces a pA-level current signal through the sensing cathode and the reference electrode. An Unisense Microsensor Multimeter is used to polarise the electrodes, to convert the sensor signal to mV-range voltage signal.

As the oxygen sensor responses linearly from zero oxygen to 100% oxygen, a linear calibration is required to convert the mV signal to oxygen concentration. Calibration of the sensor is performed in a deionised water container. The zero-oxygen level of the sensor signal is recorded after the container is purged from oxygen with a 30-minute argon gas bubbling. The atmosphere-level response is then recorded by bubbling the reservoir with air. In this thesis, the atmosphere-level oxygen concentration is looked up in a standard oxygen concentration-temperature table according to the container temperature. Since a linear relationship holds between the electrode potential and the oxygen concentration, the above two-point calibration is sufficient for our oxygen sensor. Now the sensor is ready for measurement.

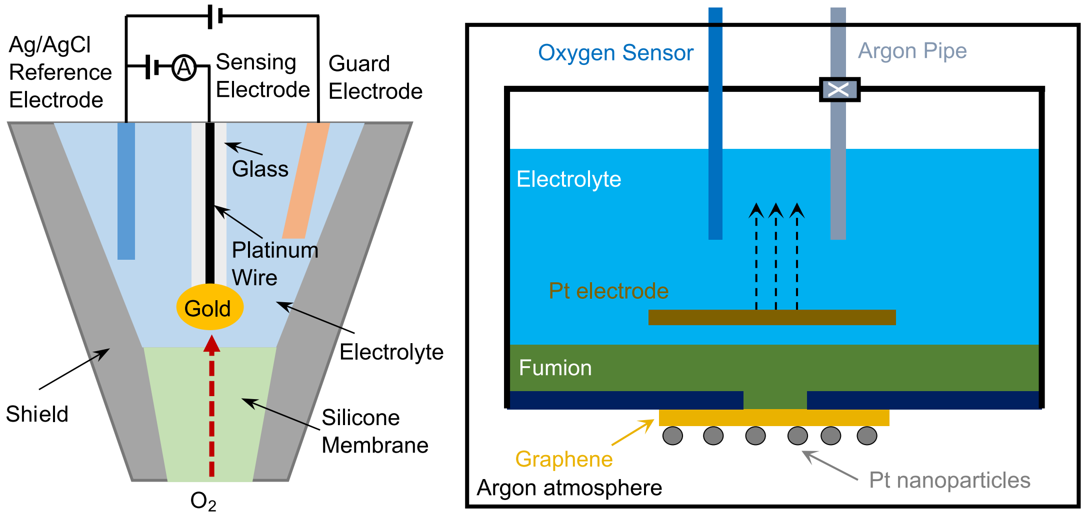

(a) (b)

Figure 5.12: Schematic of experimental setup for oxygen flux measurement. (a) Structure of the oxygen sensor and (b) experimental setup for measuring oxygen concentration.

The schematic for measuring the oxygen flux is displayed in Fig. 5.12b. Devices are clamped to a homemade transparent acrylic liquid cell with the polymer side facing the inside of the cell. The space between the device and the cell is sealed by silicone gaskets. Three outlets are machined through the cell letting in an oxygen sensor, a needle connected with an Argon supply, and a Pt wire electrode. The outlets are sealed with gaskets. A magnetic stir bar is put inside the cell and kept with a rotation rate of 300 rpm to force the convection of the oxygen dissolved in the solution. To prevent the oxygen leakage of the cell, we put the whole cell in a home-made box that is constantly circulated with argon gas. This allows the oxygen concentration in the cell to relax to a low level well controlled by the argon box other than being exposed directly in the atmosphere.

Before measurement, the cell is filled with 1 mL KOH solution through one of the outlets. The solution is then purged from oxygen by bubbling argon gas through the needle for at least 30 mins. The oxygen concentration in the solution is constantly monitored during the purging process.

Next, we start the measurement by a background recording of both current and concentration without applying any voltage. The current density and the concentration of oxygen are measured simultaneously. Then a fixed voltage is applied between the Au electrode and Pt wire. The corresponding dark current and concentration signals are recorded for 10 mins. After that, the illumination is turned on for another 10 minutes to measure the bright signals. Finally, we turn off the illumination and bias together to let the oxygen concentration in the cell return to the background level. Figure 7.3 shows the result of a typical oxygen flux measurement. The oxygen flux follows the changes of current, which are tuned by voltage and illumination.

Chapter 6

Field Effect in Water Dissociation on Graphene

In ambient conditions, a water molecule can dissociate into a proton and a hydroxide ion. Under a strong electric field, the dissociation of water molecules can be accelerated. The proton-hydroxide ion pair density is hence increased, which leads to an increase of ion current that could be observable in transport experiments. However, transport experiments to measure the field effect in water dissociation are still elusive, because in theory, to yield a field effect in liquid water requires an intensive field of $E \sim 10^8$-10^9 V m^{-1}. In this chapter, we design transport experiments to measure water dissociation reactions in liquid water using one-atom-thick proton-permeable electrodes. We show that water molecules can dissociate across freestanding graphene electrodes, with the one-atom-thick interface separating the resulting protons and hydroxide ions on opposite sides. We attribute these findings to a field effect in the water dissociation reaction. This can be quantified by a net proton current across graphene, which is monotonically dependant on the large electric field presenting near the surface of any electrodes.

Contributions

My contributions to the work in this chapter include: flake preparation, lithography, contact and catalysts deposition, suspended membrane fabrication; electrical and optical measurements; theoretical calculation (Fig. 6.10 and 6.11), conductivity and potential analysis, Onsager analysis.

The author conducted fabrication and measurement works in the initial stage of this project. After the main idea in this chapter had been prototyped, Victor G. Moreira joined the group helping with fabrication, and produced one device that was used in Fig. 6.9, measured by myself. Later, Eoin Griffin joined this project helping with hydrogen-pressure dependence measurement and control experiments. Victor G. Moreira and Eoin Griffin produced data for Fig 6.5 and 6.6, and the graphite curve in Fig. 6.9b.

6.1 Introduction

The electrical double layer (EDL) theory predicts that, in a few angstroms to the surface of electrodes immersed in water, the electric field can typically reach $\sim 10^8$-10^9 V m^{-1} at low applied voltages $\lesssim 1$ V (see bottom graph in Fig. 6.1) [9, 71]. The strong electric field shifts the water dissociation equilibrium and increase the free ion pair density (n_f) near the surface of the electrode [7, 8, 10]. In theory, the increase of free ion density (Δn_f) should be observable as an increase in the ion conductance in transport experiments.

However, since the electric field decays rapidly in just a Debye length (tens of angstroms) away from the electrode surface, n_f reduces to its bulk value, limiting the ion conductance of the cell [25, 71]. This would require two electrodes being built angstroms close to each other in order to eliminate the limit of bulk electrolyte [144],

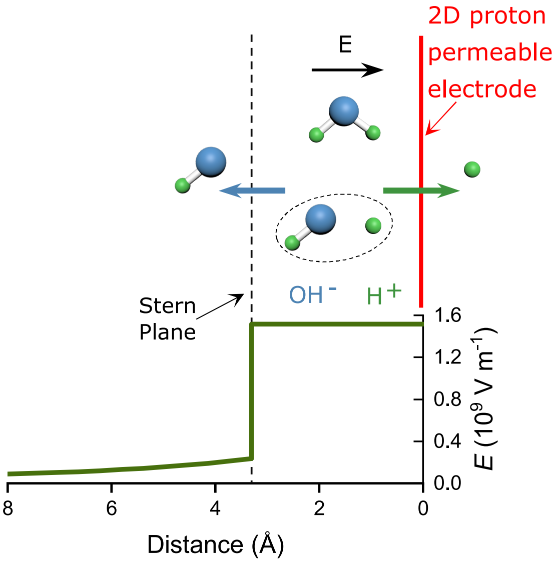

Figure 6.1: Illustration of the working principle of the experimental setup. Bottom graph: the electric field as a function of distance from the surface of graphene, calculated using the modified Gouy-Chapman-Stern model for $\phi_0 = 0.75$ V and 1 mM electrolyte concentration.

which would instantly lead to the collapse of the electrodes because of enormous pressure from the electric field [145]. For this task, graphene is a preferred electrode material, for it combines both high in-plane electron conductivity [80], out-of-plane proton permeability [5], and high proton selectivity [113]. A cell made with a suspended graphene electrode should facilitate the generation of free ion pairs on the electrode surface under the electric field, allowing for the free ion pairs to be spatially separated across the opposite sides of the one-atom-thick interface. A conceptual schematic of the above principle is shown in Fig. 6.1. In the following sections, we present experimental results on such a cell.

6.2 Devices and Experimental Setup

The structure of devices and a basic experimental setup for *I*-*V* measurement are illustrated in Fig. 6.2a. The devices were made with monolayer graphene suspended

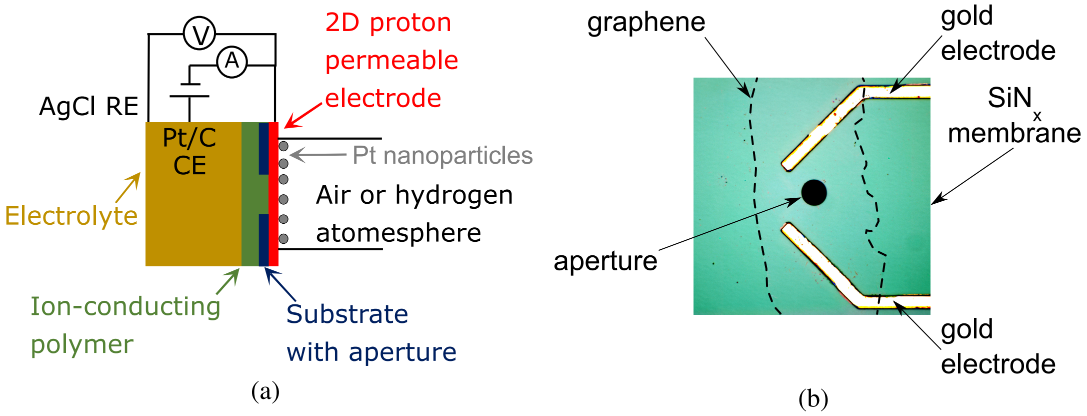

Figure 6.2: Experimental setup. (a). Schematic of the experimental setup. Counter electrode (CE): a Pt/carbon electrode. Reference electrode (RE): an Ag/AgCl reference electrode. (b). Optical image of a device. The image shows a graphene flake on two gold contacts, which were shorted before measurement. The dashed lines area is covered with graphene. The middle circle with a diameter of 10 μm is the aperture in the silicon nitride substrate.

over micro-fabricated holes (diameter d, typically 10 μm) etched through silicon nitride substrates. The graphene membrane was electrically connected to gold contacts fabricated on the substrate. On one side of the device, Pt nanoparticles were deposited over an area with diameter D (typically $\sim$ 1 cm) centred around the graphene membrane. Droplets of an anion-exchange polymer dispersion (Fumion FAA Solution, FumaTech) were applied to the opposite side of the device to form a hydroxide-ion conducting layer [146]. The polymer coating provided mechanical support for the membrane, increasing the devices' lifetime. A porous carbon electrode loaded with Pt catalyst was electrically connected to the polymer membrane. Figure 6.2b shows an optical microscopic image of a device as an example. In Fig. 6.2b, a graphene flake was in contact with two gold electrodes and covered the middle hole fabricated on the silicon nitride membrane. For more details on devices fabrication, see Section 5.1.

A Keithley sourcemeter 2636A was used to measure the electrical properties of the devices, following the methods introduced in Section 5.2.1. Unless described otherwise, all experiments were performed in a three-electrode geometry (see Section 5.2.1) with an AgCl reference electrode at room temperature. As shown in Fig 6.2a, a Pt/-carbon electrode was used as counter electrode to apply external voltage bias with graphene electrode, the potential at the graphene electrode was measured against a reference AgCl electrode, and the *I*-*V* response is measured using the sourcemeter. The applied voltage was typically scanned between ±100 mV around the zero current potential at sweep rates of $0.01\ \text{V}\cdot\text{min}^{-1}$. For high quality zero current potential measurement, the open circuit voltage is measureed directly over time to remove hysteresis in *I*-*V* measurement. In this chapter, all devices were measured in the air unless explicitly stated. Neutral to alkaline pH solutions were used as the electrolyte in experiments. Since there is only a trace concentration of proton in electrolytes, any proton transport current measured through the proton-permeable electrode should come from water dissociation.

6.3 Transport Characterisation

In our device, the extent of water dissociation can be inferred from the amount of proton transferring through graphene. This was quantified by the proton areal conductance, G_H, from the current versus voltage measurements (*I*-*V*). The slope of *I*-*V* at small V-bias (typically ±100 mV) is used to estimate G_H. An example of such measurement is shown in Fig. 6.3a. From *I*-*V*curves, the potential drop between the electrode and the bulk solution (ϕ) is conveniently available.

In Fig. 6.3a, the *I*-*V*curves are measured using $C_{\text{KOH}} = 100$ mM. Near the zero current potential of ~ 750 mV, the *I*-*V* response is linear. From the slope, we observed a large proton areal conductance ($G_{\text{H}} \approx 50\ \text{mS}\cdot\text{cm}^{-2}$). On top of this, as introduced in Section 2.2, with ϕ and the electrolyte concentration, the electric field E at the graphene-electrolyte interface can be inferred from the EDL model. Our calculation using the modified GCS model with the above experimental input ϕ and C_{KOH} predicts

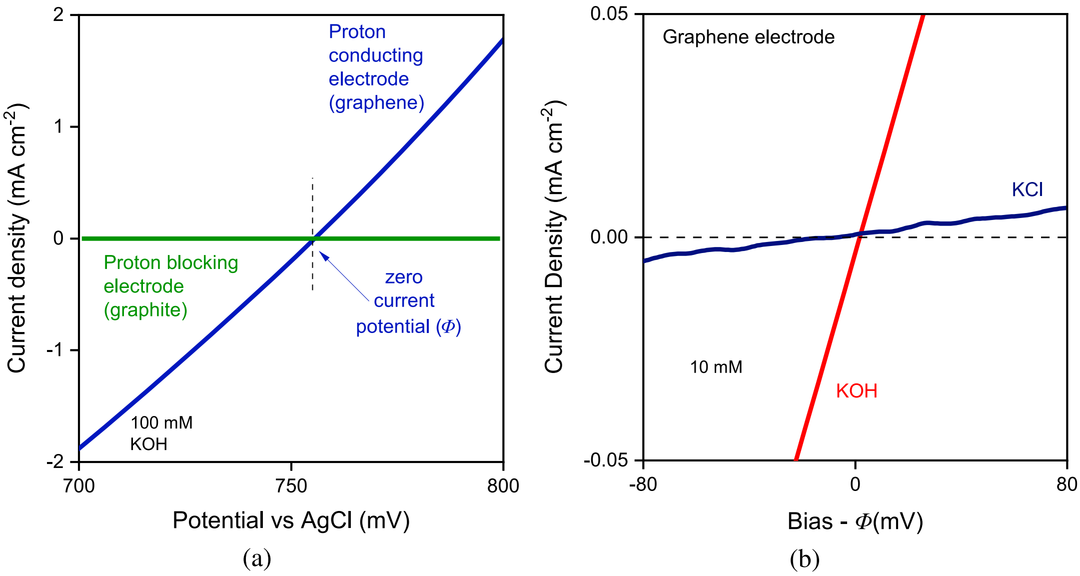

Figure 6.3: Examples of *I*-*V* characteristics. (a) Graphene and control devices measured with 100 mM KOH electrolyte in air. Solid curves are *I*-*V* response obtained from graphene (red) and graphite (yellow) devices, respectively. Dotted line: zero current potential (ϕ) (b) Devices measured with 10 mm KOH and KCl electrolytes respectively in air. Red and black curves were obtained from a graphene device measured with KOH and KCl electrolyte, respectively.

$E \approx 1.3\ \mathrm{GV \cdot m^{-1}}$, which suggests that it could be the field effect that induces the large G_{H}. For there to be a field effect, the measured variables, E and G_H should follow the Onsager function form $G_H(E)$ discussed in Section 2.3.2, which we will seek in the following sections.

To establish the functional relationship $G_H(E)$ experimentally, we settled on utilising the proton activity difference (Δa_{H}) across the graphene membrane. This Δa_{H} is created by the proton and hydroxide ions separated from the membrane with $\Delta a_{\mathrm{H}} = a^o_{\mathrm{H}}/a^i_{\mathrm{H}}$, where a^o_{H} and a^i_{H} are proton activities in the platinum side and the electrolyte side of graphene, respectively [9, 113]. Δa_{H} leads to a potential drop ϕ at zero current conditions and can be measured by extracting the zero current potential in the *I*-*V* response. In principle, ϕ and Δa_{H} follow the Nernst equation $\phi = kT/e \ln \Delta a_{\mathrm{H}}$.

The symmetry between proton and hydroxide ions allows us to control the proton activity on the two sides of the membrane. Since the electrolyte side of the membrane is exposed to electrolytes made with KOH solution, the proton activity is $a_{\mathrm{H}}^{i} = 10^{-\mathrm{pH}}$. With the platinum side exposed to the air (as in Fig. 6.3a), the protons on the Pt side of devices are freely equilibrated. The proton activity difference leads to the non-zero zero-current potential in Fig. 6.3a.

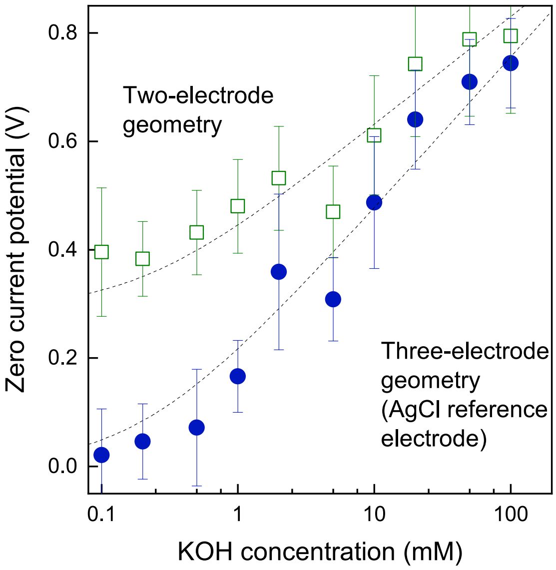

Figure 6.4: Typical zero-current potential measured in two-electrode and three-electrode geometry. The zero-current potential was measured versus time. Error bars are stadard deviation values of the time series. Dashed curves are a guide to the eye.

We further changed KOH from 0.1 mM to 100 mM and measured the zero-current potentials. An example result from a graphene device is displayed in Fig. 6.4. This was measured by taking zero-current potential versus time. The averages are reported when the signal stabilises, with stadard deviation reported as error bars. It is shown that the potential can be changed from ~ 0 to ~ 0.8 V. In Fig. 6.4, we also show the measurement performed in the two-electrode geometry for comparison, which shifted the potential, as we changed the reference to carbon/Pt electrode. This also suggests that the electrode resistance dominates the response of our devices since the deviation of potential between two-electrode and three-electrode geometry are relatively small ($\lesssim 0.21$ V), which is expected in a microelectrode cell.

Furthermore, the Pt-decorated side of the membrane can be exposed to hydrogen gas to generate a fixed hydrogen activity via $a^o_{H_2} = p_{H_2}/p_0$ where $p_0 = 1$ bar. Because hydrogen can split into protons on the Pt surface, this should allow us to control the proton activity on the Pt side of graphene. To verify this, we measured ϕ of our devices at p_{H_2} ranging from 0.01 bar to 1 bar with $C_{KOH} = 1$ mM.

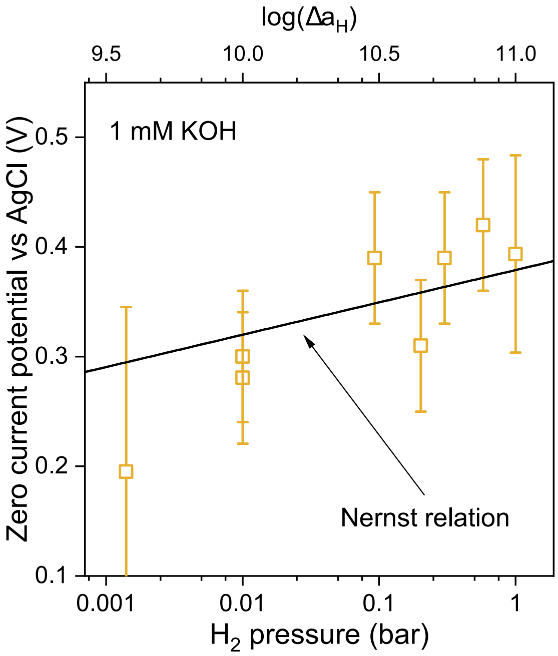

Figure 6.5: H_2 pressure dependency of zero-current potential. Zero-current voltage of the devices as a function of H_2 pressure, measured with 1 mM KOH. Zero-current potential was measured directly versus time. Error bars: standard deviation. The solid line is the Nernst relation.

As shown in Fig. 6.5, ϕ is a function of p_{H_2} that follows exactly the Nernst equation $\phi = \phi_0 + kT/e \ln \Delta a_H$ where $\Delta a_H = \sqrt{a^o_{H_2}}/a^i_H = \sqrt{p_{H_2}/p_0}/a_H$ and $\phi_0 \approx -25$ mV, a small constant. This is expected, as the proton activities are well controlled on both sides in this measurement.

At this point, we have demonstrated that a controllable ϕ and thus E can be generated by tuning the proton activity difference across the graphene membrane.

6.4 Control Experiments

Before heading into investigating the relationship $G_{\mathrm{H}}(E)$, we performed control experiments to verify whether the large G_{H} is indeed a result of proton transport and large electric fields.

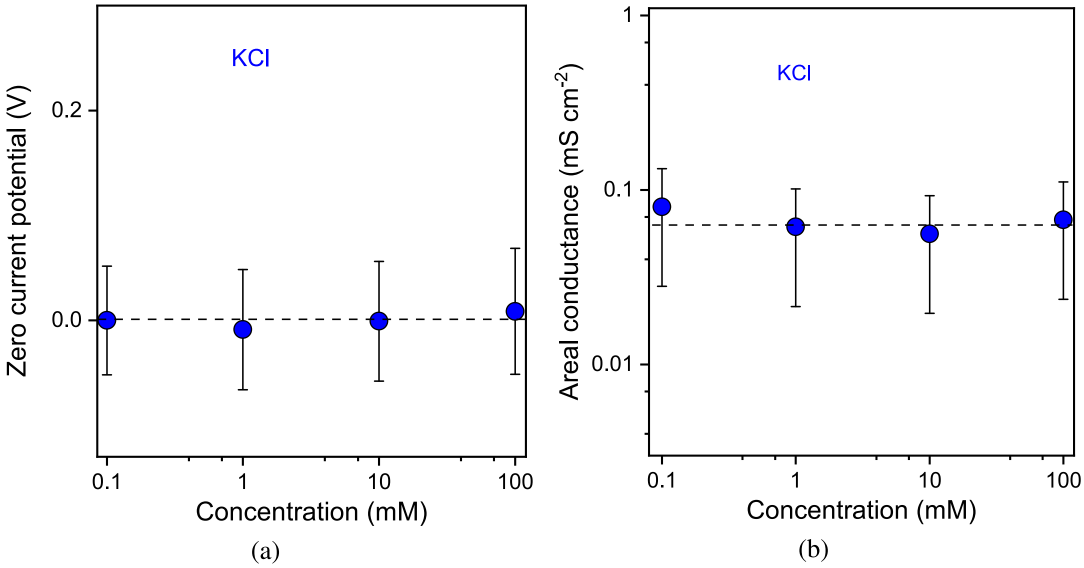

Figure 6.6: Electrical measurements of control device in potassium chloride electrolyte. (a), Zero current potential of graphene devices as a function of KCl electrolyte concentration measured versus AgCl reference electrode. (b), Corresponding areal conductivity for the data in panel (a). The dotted lines are a guide to the eye. The zero current potential and areal conductivity shown here are measured with *I*-*V* response measurement. Error bars: uncertainty of using linear fit to extract the potential and conductivity.

Firstly, we measured devices fabricated similarly to the above described but using few-layer graphene (graphite) instead of monolayer graphene. Since graphite is impermeable to protons [5], this makes proton transport impossible in these control devices. The *I*-*V* responses of these graphite devices in hydroxide electrolyte are shown in Fig. 6.3a, which yields G_{H} that is several orders of magnitude smaller than that of graphene devices. With this evidence, we can confirm that G_{H} is a result of proton transport. 2D proton permeable electrodes are essential to study the field effect in water dissociation. The negligible *I*-*V* response in graphite devices made it impossible to measure the electrode potential and evaluate E-field (Fig. 6.3a).

Then, we performed control experiments in which there is only a very small proton activity difference across graphene by using potassium chloride electrolyte instead of hydroxide. As we can see from Fig. 6.3b, the *I*-*V* response in chloride was much smaller than in hydroxide. For all the C_{KCl} studied (0.1-100 mM), G_{H} $\approx 0.075\ \mathrm{mS} \cdot \mathrm{cm}^{-2}$, see Fig. 6.6b. This conductivity is 1-3 orders of magnitude lower than observed in devices measured with KOH and about six times larger than the background (and graphite devices). The potential drop ϕ in this case is ~ 0 mV (see Fig. 6.6a). This yield a near-zero E-field, which is consistent with the observed small G_{H}. Note that even these small currents were not observed in reference graphite devices, in which protons are blocked by thick graphite, preventing spatial separation of protons from hydroxide ions.

These control experiments confirm that a large electric field is only possible when proton transport is large.

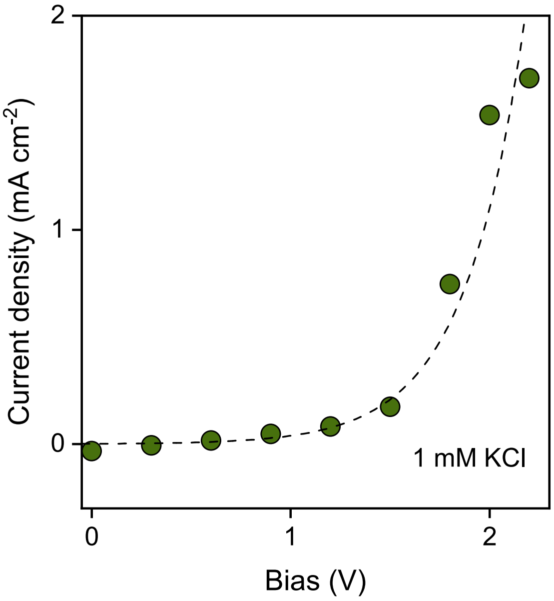

Figure 6.7: Nonlinear *I*-*V* response of a graphene device measured with KCl electrolyte.

The latter experiment also leads to an alternative strategy to achieve high voltage in an electrolysis cell. This would be to use any electrolyte regardless of pH and then apply a sufficiently high potential to the graphene electrode. Here we applied higher voltage bias to the graphene devices in KCl solution, which indeed increased the current in the devices, as we expected, see Fig. 6.7. However, it also yielded non-linear *I*-*V* curves, which turned out to be difficult to interpret. Our approach based on proton activity gradients has the advantage of not only producing large E-fields, but also doing so in equilibrium conditions. Measurement in near-equilibrium conditions yields a linear *I*-*V* response, which allows for robust quantitative analysis. This is a key advantage of our setup over previous works investigating field effect on water dissociation [34, 62, 74].

6.5 Field Effect

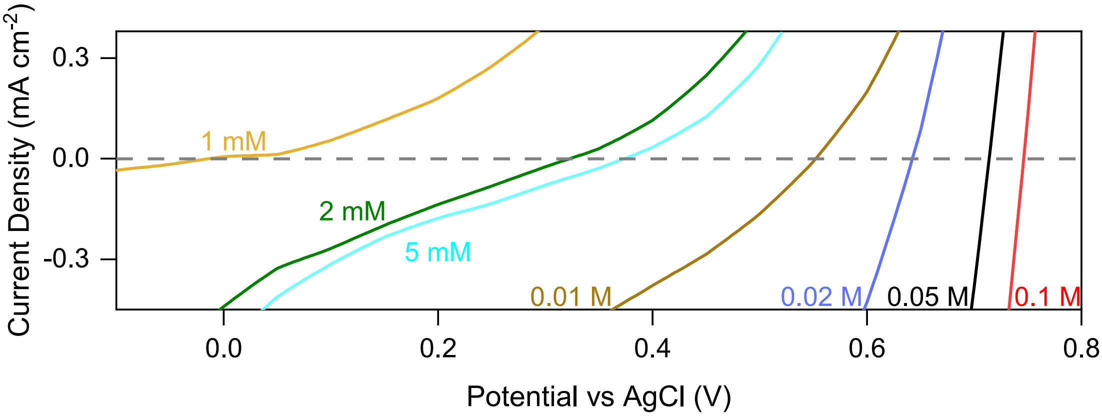

Figure 6.8: Current-voltage response of devices measured with KOH. Example *I*-*V* characteristics of a graphene device measured using potassium hydroxide electrolytes with different concentrations. The *I*-*V* responses are displayed in a wide voltage range that includes parts of the non-linear regime for each concentration to present all these data in a single graph. Typically, within ±50 mV from the zero-current potential, the *I*-*V* responses are linear for each concentration.

After knowing that the field effect induces large proton currents and how to control ϕ and E, it is time to conduct a systematic study on the relation between G_H and E.

We decided to perform experiments to investigate the *I*-*V* response of our devices in different hydroxide concentrations. This decision has an experimental concern that controlling the activity of hydroxide is practically easier than working with hydrogen gases, as hydrogen gasses require an additional sealed container.

We measured devices with the electrolyte side exposed to KOH solution of concentration ranging from 0.1 to 100 mM. Example *I*-*V* responses for a graphene device is shown in Fig. 6.8. For each *I*-*V* curve, ϕ and G_H were extracted from data within the linear regime (±50 mV from the zero-current potential).

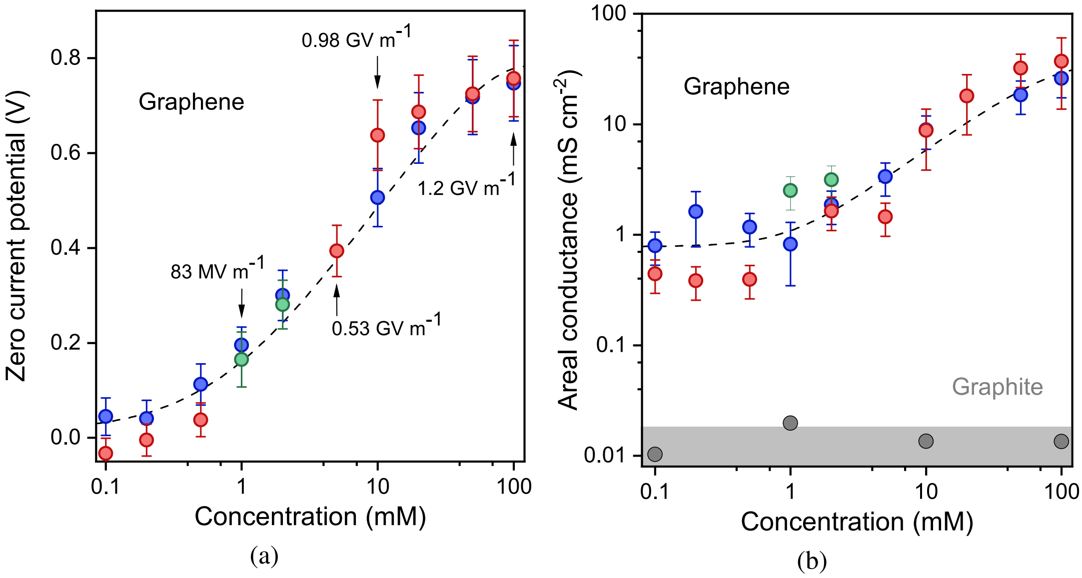

(a) (b)

Figure 6.9: Electrical measurements of water dissociation across graphene electrodes. (a). Zero-current voltage (ϕ) of devices dependent on hydroxide concentration. The labels with arrows mark the *E*-field calculated from the modified Gouy-Chapman-Stern model for several pairs of ϕ and C_{KOH} values (b). Areal conductance G_H of the devices in panel a as a function of C_{KOH}. Solid data points are devices measured with KOH electrolyte. Gray points are a graphite control device. The dashed lines are a guide to the eye. The blue, red and green data points are from three different graphene devices. Error bars: uncertainty of using linear fit to extract the ϕ and G_H. The saturation of conductivity observed at $C_{KOH} \leq 1$ mM is caused by fixed charges in the anion-exchange polymer. The shaded area is typical conductivity induced by leakage current.

Figure 6.9 summaries the dependence of ϕ and G_H on C_{KOH}. As shown in Fig. 6.9a,

ϕ increases with C_{KOH}. With calculation using the modified GCS model, E can be controlled in a wide range from $\sim 10^7 - 10^9$ V $\cdot$ m^{-1}. E as high as ~ 1.2 GV $\cdot$ m^{-1} can be achieved at $C_{\mathrm{KOH}} = 100$ mM. measurement in 1 M KOH resulted in $\phi \approx 0.8$ V, which leads to a estimation of higher E of ~ 2 GV $\cdot$ m^{-1}. Unfortunately, such harsh conditions greatly shortened the lifetime of our devices which did not survive more than several minutes in electrical measurements. The graphene membranes ruptured as examined by optical microscopy, which is probably caused by mechanical strain induced by high E-field [147] or dielectric breakdown of near-surface water and polymer [148]. Apart from that, G_{H} in Fig. 6.9b shows a monotonic dependence on C_{KOH} similar to ϕ.

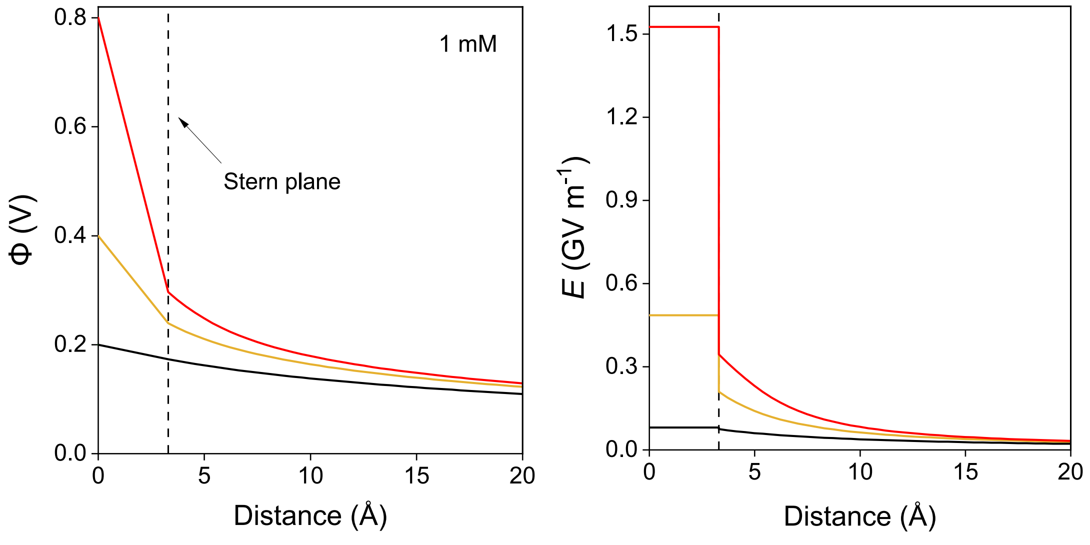

(a) (b)

Figure 6.10: Electric potential and field profiles in the electrical double layer model. (a). Electric potential profiles for different electrode potential (0.8 V, 0.4 V, and 0.2 V) calculated by the EDL model for 1 mMconcentration. The dotted line indicates the Stern plane. (b). Electric field profiles corresponding to the potential in panel a.

Figure 6.10 shows example of ϕ and E-field profiles calculated with this model (see details in Section 2.2.4). The non-continuous slope of potential and step-like E-field are results of discrete dielectric constant profile across the Stern layer (field-dependant) and diffuse layer ($\varepsilon_r = 78$) of our EDL model. This analysis was repeated for all the combinations of $\phi(x = 0)$ (zero-current potentials) and electrolyte concentration in the experiments (examples are the labels in Fig. 6.9a).

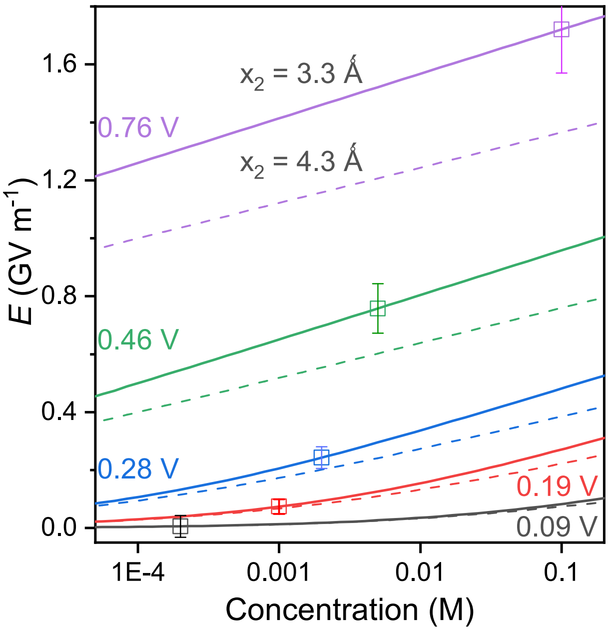

Figure 6.11: Electric field in the Stern layer as a function of concentration. The electric fields are calculated from the EDL model for different fixed electrode potentials ($\phi(x=0)$) obtained experimentally. The solid lines are E-field calculated for Stern plane distance of $x_2 = 3.3$ Å. The dotted lines, same potentials but for $x_2 = 4.3$ Å. Squared scatter, E-field calculated from experimentally determined $\phi(x=0)$ and the corresponding concentration using $x_2 = 3.3$ Å. Error bars are the uncertainty inferred from the experimental accuracy of $\phi(x=0)$.

An important parameter of the EDL model is the Stern layer thickness, which was chosen as $x_2 = 3.3$ Å. This is based on the theoretical calculation of potassium diameter for potassium and hydroxide in contact with graphene [149, 150]. The uncertainty in this parameter was estimated to be ± 1 Å, resulting in $\simeq 10\%$ uncertainty in the E-field (Fig. 6.11). This uncertainty is comparable to those induced by the experimental error of $\phi(X=0)$, which demonstrates the robustness of our EDL model.

With E and G_H, we are able to reveal a relation between them by combining the two data sets in Fig. 6.12. It is clear that G_H increases monotonically with E. Hence, this empirical relation we found demonstrates a field effect in water dissociation. Similar concentration dependency experiments were performed in the control devices, as we introduced above, graphite devices measured with KOH solution (Fig. 6.9) and graphene devices measured with KCl solution (Fig. 6.6). In both cases, ϕ and G_{H} did not show a dependence on electrolyte concentration.

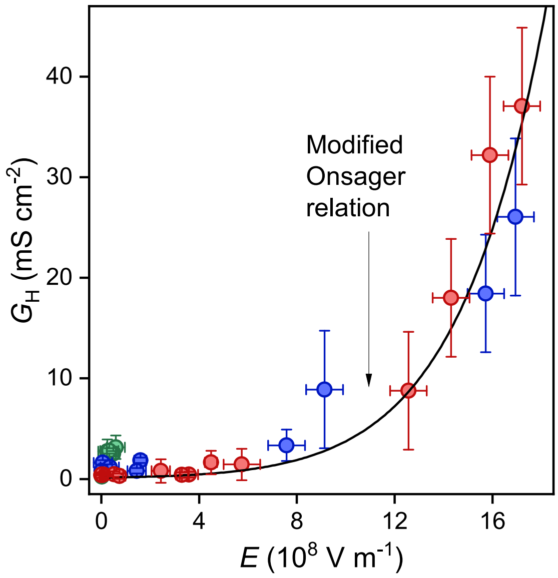

Figure 6.12: Onsager relation for dark conditions. The proton conductance (G_{H}) from Fig. 6.9a is plotted as a function of the E-field extracted from Fig. 6.9b. The blue, red and green data points corresponds to the graphene devices in Fig. 6.9. Black curve is Onsager's theory of the second Wien effect, $G_{\mathrm{H}}(E) = F[\alpha E, \varepsilon_r(E)]G_{\mathrm{H}}(0)$ with $G_{\mathrm{H}}(0) = 0.15\ \mathrm{mS \cdot cm^{-2}}$ and $\alpha = 0.26$ as fitting parameters. Y-error bars: uncertainty of using linear fit to extract G_{H}. X-error bars: uncertainty inferred from the experimental accuracy of $\phi(x = 0)$.

As introduced in Section 2.3.2, Onsager developed a theory of the second Wien effect, which should be able to describe mathematically the $G_{\mathrm{H}}(E)$ relation we found in experiments. Onsager found that the free ion pair density n_{f} with and without E-field is governed by the formula $F(E) = n_{\mathrm{f}}(E)/n_{\mathrm{f}}(0) = [I_1(\sqrt{8x}/\sqrt{2x})]^{1/2}$ where F notes for the Onsager function, I_1 is a modified Bessel function, $x = e^3E/(8\pi\varepsilon_0\varepsilon_r(k_BT)^2)$, with e the elementary charge, eo the vacuum permittivity, ε_r the dielectric constant of water, and k_BT the thermal energy [7, 8]. The dielectric constant ε_r was then expressed in the field-dependant form given by Eq. 2.32, which yields $F[E, \varepsilon_r(E)]$. Note that the proton areal conductance G_{H} is proportional to the proton density that is equal to n_f in this case [5, 113]. Then the ratio $G_\mathrm{H}(E)/G_\mathrm{H}(0) = n_\mathrm{f}(E)/n_\mathrm{f}(0)$ should agree with Onsager's theory. Here, the zero-field conductivity, $G_\mathrm{H}(0)$, was used as a fitting parameter to establish the Onsager relation. Additionally, we introduced an extra parameter α into the Onsager's formula to scale the electric field but without scaling again the $\varepsilon_r(E)$ [22], i.e. we used $F[\alpha E, \varepsilon_r(E)]$ instead of $F[E, \varepsilon_r(E)]$. This α accounts for the estimated Stern layer thickness affecting the calculation of the electric field. With $G_\mathrm{H}(0) = 0.15\ \mathrm{mS \cdot cm^{-2}}$, $\alpha = 0.26$, Onsager's theory matches well with our data, which explains excellently the experimental $G_\mathrm{H}(E)$ relation.

The parameter $G_\mathrm{H}(0)$ found above is an estimation of the conductivity of devices measured in KOH at zero E-field. This value is consistent with the conductivity measured in KCl ($\approx 0.075\ \mathrm{mS \cdot cm^{-2}}$, Fig. 6.6b), in which we observed nearly zero E-field as well. Hence, for low electric fields, we obtained the same water dissociation rate in devices measured with KOH or KCl, as expected.

Nevertheless, it is instructive to compare the rate with the literature using different systems. If we consider small applied voltages, $V \lesssim k_B T/e$, $G_\mathrm{H}(0)$ can be converted to a current density of $I(0) \sim 1\ \mathrm{\mu A \cdot cm^{-2}}$. In the literature, $I(0)$ can be estimated by $I(0) \approx k_d F t C_{\mathrm{H_2O}}$, where $k_d \approx 2 \times 10^{-5}\ \mathrm{s^{-1}}$ is the intrinsic rate of water dissociation [151, 152], F the Faraday constant, t the reaction layer thickness, and $C_{\mathrm{H_2O}} = 1/18\ \mathrm{mol \cdot cm^{-1}}$ the concentration of water molecules for pure water. Reaction layer thickness is typically from 100 nm to 10 microm [62, 152]. From the above $I(0)$ is approximately from $1\ \mathrm{\mu A \cdot cm^{-2}}$ to $100\ \mathrm{\mu A \cdot cm^{-2}}$. Our $I(0)$ is within the lower range of the literature values, which is reasonable, considering the proton permeation barrier imposed by graphene [5].

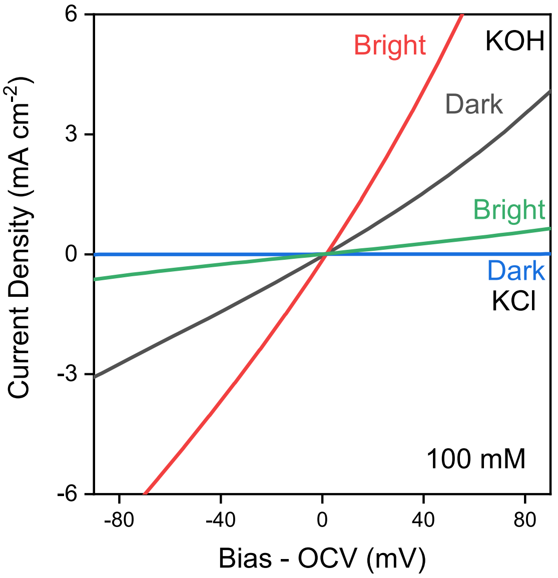

Figure 6.13: *I*-*V* characteristics of devices in dark and bright condition. In order to present all the *I*-*V* curves in one graph, the potential axis is shifted by subtracting it with the zero current potential for each curve. The red and grey lines are graphene devices measured in KOH electrolyte. The green and blue lines, graphene devices measured in KCl electrolyte.

6.6 Enhancement with Photo-proton Effect

From our previous work, we observed that low-power illumination increases the proton conductivity of graphene [131]. It is now of interest to verify if this enhancement of proton conductivity still exists in this work and how would the field effect couple with graphene's photo-responsivity.

By using a calibrated Newport Oriel Sol3A light source, we performed *I*-*V* characterisations on graphene devices in KOH and KCl electrolytes. The typical photo-response of the devices under illumination power density of 100 $\mathrm{mW \cdot cm^{-2}}$ is shown in Fig. 6.13. Increased proton current under bright conditions is observed in both electrolytes, which is expected since enhanced proton conductivity can promote the rate of water dissociation, even without a strong E-field.

This makes it possible to investigate the field effect in water dissociation across a different material, essentially graphene, with an enhanced proton conductivity. Same measurements of ϕ and G_{H} versus hydroxide concentration ($C_{\mathrm{KOH}} = 0.1$-100 mM) were repeated for the devices under illumination (power density 100 $\mathrm{mW \cdot cm^{-2}}$). The results are displayed in Fig. 6.14. The potential and conductance increased with concentrations as observed in dark conditions. As shown in Fig. 6.14a, the potential was shifted by about -200 mV with respect to the dark, which can be attributed to local photovoltage induced by light generated hot electrons [131]. For all concentrations, the conductance was $\sim$ 10 times higher than that in dark condition (Fig. 6.14b).

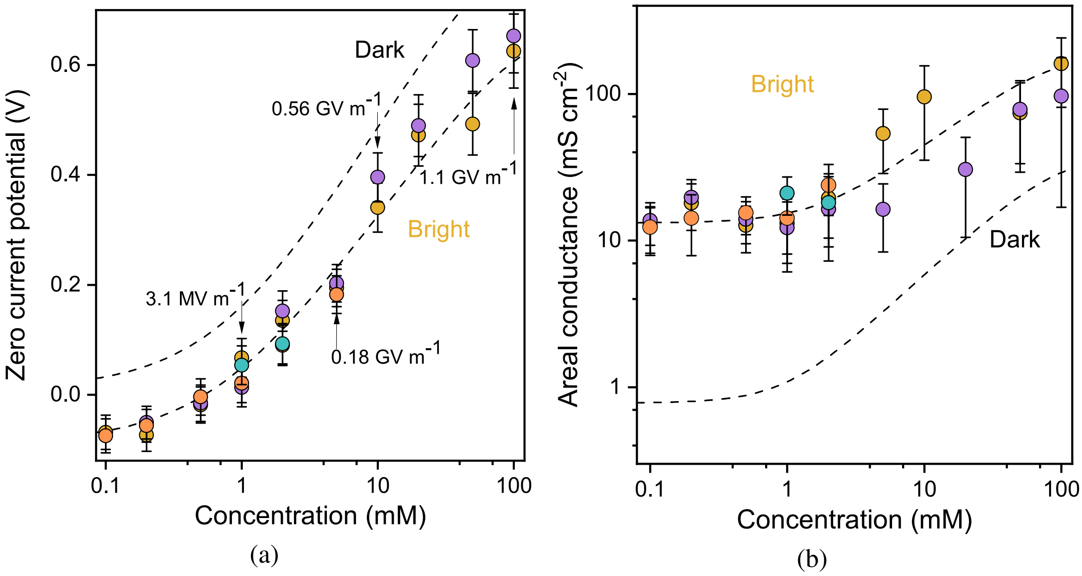

(a)

(b)

Figure 6.14: Electrical measurements of water dissociation across graphene electrodes under illumination. Simulated solar illumination with power density 100 $\mathrm{mW \cdot cm^{-2}}$ was used. (a). Zero-current voltage of devices as a function of hydroxide concentration. The annotations mark the E-field calculated from the modified Gouy-Chapman-Stern model for several pairs of ϕ and C_{KOH}. (b). Areal conductance as a function of hydroxide concentration. The yellow, purple, orange and cyan data points are four graphene devices measured with KOH electrolyte. The dashed lines are a guide to the eye for devices measured in dark conditions and under der illumination. The saturation at $C_{\mathrm{KOH}} \leq 1$ mM is caused by fixed charges in the anion-exchange polymer. Error bars: uncertainty of using linear fit to extract the ϕ and G_{H}.

The ϕ and G_{H} in bright are combined in Fig. 6.15, which again shows a field effect in good agreement with Onsager's theory. The same $\alpha = 0.26$ as in the dark condition is used, and the $G_{\mathrm{H}}(0)$ parameter for this case is 1.39 $\mathrm{mS \cdot cm^{-2}}$, which is $\sim$ 7 times as large as $G_\mathrm{H}(0)$ in the dark. Such behaviour is expected as the measured proton current depends on the electrode resistance, which is lowered by illumination. This also implies that the observed field effect is independent of the electrode material's characteristics.

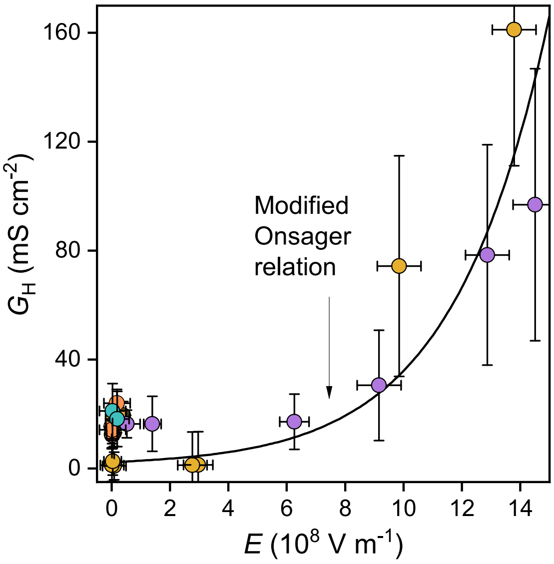

Figure 6.15: Onsager relation for bright conditions. The proton conductance (G_H) from Fig. 6.14a is plotted as a function of the E-field extracted from Fig. 6.14b. The yellow, purple, orange and cyan data points corresponds to the graphene devices in Fig. 6.14. Black curve is Onsager's theory of the second Wien effect with $G_\mathrm{H}(0) = 1.39\ \mathrm{mS} \cdot \mathrm{cm}^{-2}$ and $\alpha = 0.26$ as fitting parameters. Y-error bars: uncertainty of using linear fit to extract G_H. X-error bars: uncertainty inferred from the experimental accuracy of $\phi(x = 0)$.

6.7 Conclusion

In conclusion, we demonstrated the field effect in water dissociation with systematic transport experiments. With a beautiful match between the experimentally found $G_\mathrm{H}(E)$ relation and the Onsager's theory of second Wien effect, we extended the experimental evidence of the field effect to E-field as high as $\sim 10^9\ \mathrm{V} \cdot \mathrm{m}^{-1}$. Using these devices would enable new research to study proton-transfer reactions at high E-field, improving the efficiency of these reactions that are especially essential in the energy industry.

Chapter 7

Water Electrolysis with Monolayer Graphene

In Chapter 6, we reported transport measurements of field effects in the water dissociation reaction. Experimentally, we found that proton conductance through graphene is proportional to the proton density, which is dependant on the electric field near the electrode. This can be accurately described by Onsager's theory of Wien effect. However, in the above experiments, only the equilibrium properties were characterised. It is unclear but possible that the field effect would also accelerate the full water electrolysis reaction, which follows water dissociation at a higher voltage ($\gtrsim$ 1.23 V). In this chapter, we study the out-of-equilibrium behaviour of water dissociation at the high-voltage regime. We demonstrate large water electrolysis current densities over 10 A cm^{-2} at $\gtrsim$ 2 V due to field effect, which is one to two orders of magnitude larger than in conventional water electrolysis cells. Such a high current density allows direct measurement of the rates of H_2 and O_2 gases evolving in our micrometre-sized cell.

Contributions

The work presented in this chapter is the author's own work. My contribution includes: device fabrication, electrical and optical measurements, hydrogen and oxygen flux measurements.

7.1 Introduction

It is demonstrated in Chapter 6 that field effect accelerates the rate of water dissociation reaction ($H_2O \longrightarrow H^+ + OH^-$), which is excellently explained by our analysis using Onsager's theory. The proton current, limited by the electrode resistance of our graphene devices, can also be enhanced by low-power illumination. However, the above findings are all based on indirect measurements of water dissociation by inferring proton current from electric current. The experiments were controlled in (near) equilibrium conditions, in which we focused on quantities at zero proton current. We note that at sufficiently large voltages ($\gtrsim$ 1.23 V), the full reaction of hydrogen and oxygen evolution ($H_2O \longrightarrow H_2 + \frac{1}{2}O_2$) follows the water dissociation [62, 153]. To explore this regime, we will explore the out-of-equilibrium behaviour of water dissociation across graphene electrodes. Moreover, quantifying the gaseous products of water electrolysis via mass-transport experiments allows for direct measurement of water dissociation. It is worth attention that the light-enhanced conductivity of graphene is of merit in this task, as mass-transport techniques are less sensitive than electrical measurement and thus require a larger current. We will present the experimental results in the following sections.

7.2 Experimental Setup

A schematic of the experimental setup is shown in inset Fig. 7.1. The devices follow the same structure as in Chapter 6. A Keithley's SourceMeter was used to apply bias to the device and measure current. A calibrated solar simulator (Newport Oriel Sol3A) was used to illuminate the devices. Apart from the *I*-*V* characterisation in the non-equilibrium regime, we used mass transport techniques to quantify the water electrolysis products. Due to graphene's impermeability to any gases, hydrogen and oxygen gases were separated readily on each side of the graphene membrane. This allows two chambers/cells to connect to the devices and to collect the gas products. Hydrogen flux was measured directly using a mass spectrometer (Inficon UL200 Detector). For oxygen, the dissolved oxygen concentration in the electrolyte was measured using an oxygen sensor (UNISENSE, OX-NP), and oxygen flux was inferred from the derivative of the concentration. Note that due to the different sensitivities and other experimental limitations, hydrogen and oxygen were not measured at the same time. For more details on the mass transport measurement, please refer to the methods described in Section 5.2.2 and 5.2.3.

7.3 Water Electrolysis and Mass Transport

Following our light enhancement experiments in Section 6.6, we decided to explore the potential of field effect under solar-simulated illumination to utilise a more proton-conductive system. We started with characterising the dark and bright *I*-*V* responses of the devices.

Electrical measurements of two-electrode geometry were performed in a KOH electrolyte of concentration 100 mM both in dark conditions and under solar simulated illumination of 100 $\mathrm{mW \cdot cm^{-2}}$. Figure 7.1 shows that in this voltage-bias regime, the

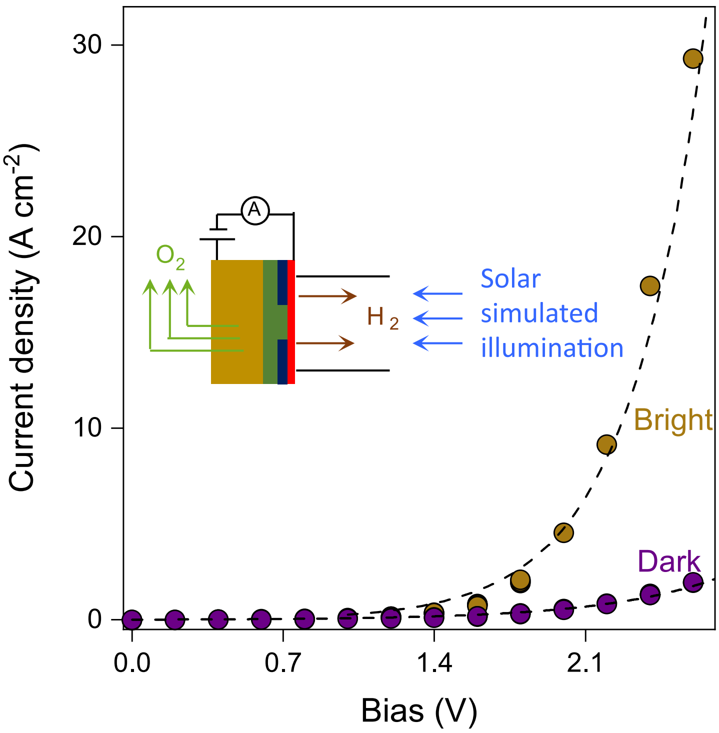

Figure 7.1: Example *I*-*V* characterisation of water electrolysis across graphene electrodes. Typical *I*-*V* curves from a graphene device measured with 100 mM hydroxide electrolyte in dark (purple data points) and bright conditions (brown data points). The dashed curves are a guide to the eye. Inset, schematic of the experimental setup.

I-*V* response becomes non-linear. More details will be covered in Section 7.4. As can be seen at voltage $\gtrsim 2$ V, the current grows exponentially, and an exceptionally fast water electrolysis rate was achieved. This is apparently a result of the field effect. Indeed, we observed $I \sim 1\ \mathrm{A \cdot cm^{-2}}$ in dark conditions and $\sim 10\ \mathrm{A \cdot cm^{-2}}$ under illumination at about 2 V. The bright current is at least one to two orders of magnitude larger than in state-of-the-art water electrolysers operating at similar voltages which typically yield $\sim 0.1 - 1\ \mathrm{A \cdot cm^{-2}}$ [34, 42, 44, 154], also see discussion in Section 3.2.3. Here, we demonstrated the potential of field effect in accelerating water electrolysis reaction. Note that the rate of the reaction is now clearly limited by the conductivity of the proton-permeable electrode material, which explains the larger response of graphene under illumination than in the dark.

Following naturally, the next step is to measure the gaseous products of the water

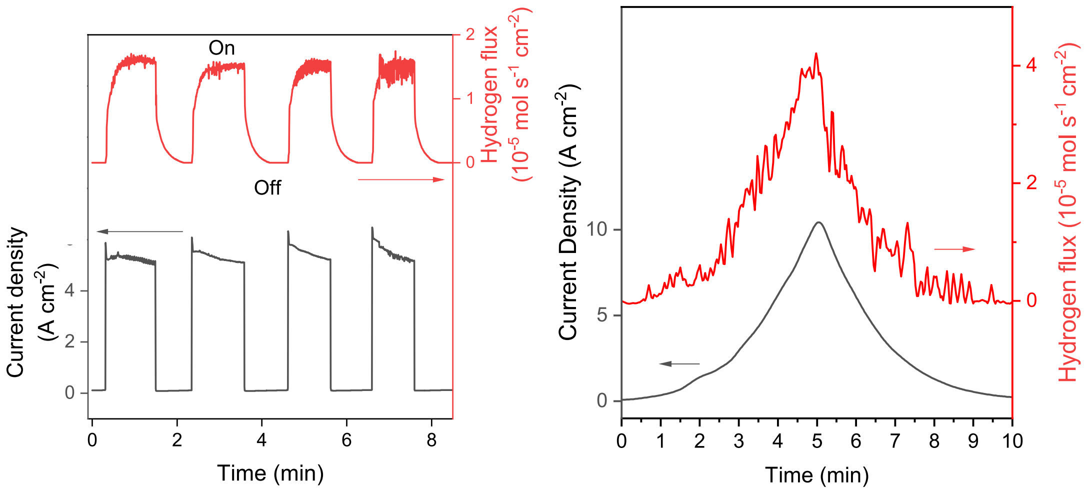

(a) (b)

Figure 7.2: Hydrogen mass-transport experiment. (a). Typical results of current density and hydrogen flux measurements recorded simultaneously under pulsed illumination (100 $\mathrm{mW \cdot cm^{-2}}$). V-bias, 1.8 V. (b). Example of current density and hydrogen flux measurements with a sweeping bias voltage (0–2 V). Illumination, 100 $\mathrm{mW \cdot cm^{-2}}$. Panel a and b are from two different graphene device. The summary of the hydrogen flux measurement is shown in Fig. 7.4.

electrolysis occurring in our devices. With the large electrolysis current, the product of water electrolysis should be detectable by mass transport experiments. It is now possible to study this reaction by measuring the products directly rather than inferring them from electrical measurements. To this end, we measured the O_2 and H_2 gases resulting from the water electrolysis both in dark conditions and under illumination.

For hydrogen measurements, the graphene electrode faced a chamber that was connected to a mass spectrometer and evacuated to the vacuum before experiments. The opposite side of the device was connected to a cell containing the hydroxide solution (inset Fig. 7.1). In the absence of an applied voltage bias or if a positive voltage was applied to graphene, no H_2 signals could be detected by the spectrometer, which is consistent with the known impermeability of graphene to all gasses [110]. For the right polarity, as shown in inset Fig. 7.1, both H_2 flux and electrical current were detected and measured simultaneously.

Typical results of H_2 mass transport experiments are shown in Fig. 7.2. In Fig. 7.2a, voltage was fixed (1.8 V) and the device was illuminated in on-off cycles (peak power $100\ \mathrm{mW}\cdot\mathrm{cm}^{-2}$). The hydrogen flux follows the trend of electrolysis current with immediate response to on-off cycles of illumination. In Fig. 7.2b, we kept the illumination on ($100\ \mathrm{mW}\cdot\mathrm{cm}^{-2}$) and swept the voltage ($0-2$ V). Again, the hydrogen flux follows the current, which is controlled by voltage bias in this case.

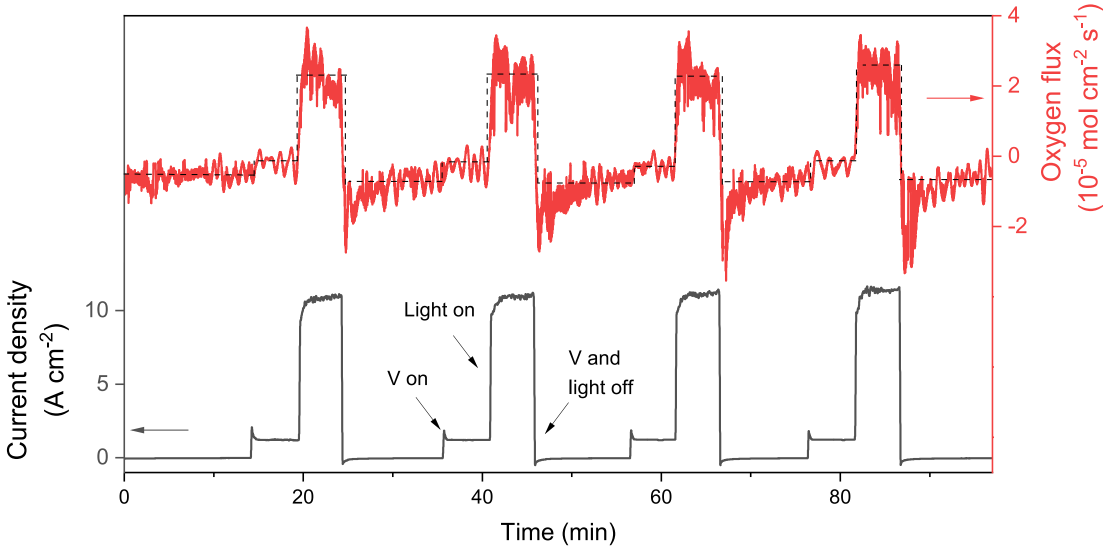

Figure 7.3: Oxygen mass-transport experiment. This figure shows typical current density and oxygen flux data recorded simultaneously from a graphene device. Measuring sequences: zero voltage bias, dark; a fixed voltage applied, dark (labelled as V on); illumination switched on (Light on); both voltage and illumination switched off (V and light off). The dashed lines are a guide to the eye. Same experiments was repeated for different voltage bias. The summary of the oxygen flux measurement is shown in Fig. 7.4.

On the other hand, O_2 evolution was quantified by monitoring the concentration of the dissolved oxygen in the solution (1 mM KOH of volume 1 ml) using a microsensor. Oxygen gases were collected by connecting the polymer side of the device to a homemade cell in which O_2 was depleted by bubbling the electrolyte with argon gas. The whole apparatus was placed in a box filled with argon atmosphere to prevent O_2 in the air from getting into the cell. Both current and oxygen concentration $[O_2]$ are measured simultaneously as a function of applied bias and illumination.

In a typical measurement, four steps were taken and maintained for a certain duration. A background is firstly recorded, followed by a constant voltage being applied to the device. Then the illumination is turned on. After that, both illumination and voltage are turned off at the same time. The four-step cycle is repeated several times for each voltage bias. The typical result of an O_2 experiment can be found in Fig. 7.3 showing $\frac{d[O_2]}{dt}$ and current versus time. As the electrolysis current jumps in steps, the oxygen flux changes in the same way, which shows apparently that the two quantities are correlated with each other.

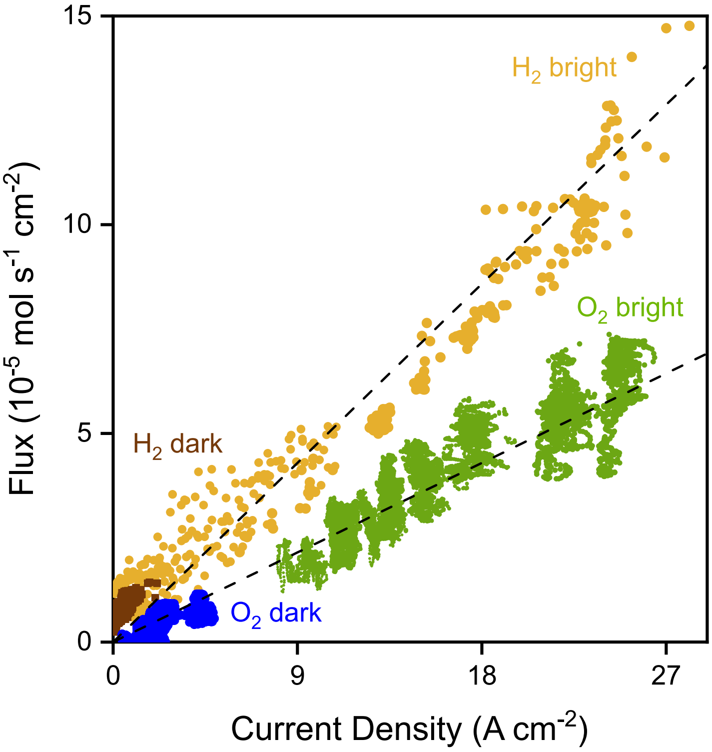

Figure 7.4: Summary of mass-transport experiments. Hydrogen flux (ϕ_{H_2}) as a function of current density in dark and bright conditions is plotted in brown and yellow data points, respectively. Dotted line corresponds to $\phi_{H_2} = I/2F$. Oxygen flux (ϕ_{O_2}) as a function of current density in dark and bright conditions, plotted in blue and green data points, respectively. Dotted line, $\phi_{O_2} = I/4F$. Data from four different graphene devices are shown in this figure, with two devices each for hydrogen and oxygen measurement.

Multiple mass transport data sets of both H_2 and O_2 for various voltage bias are combined in Fig. 7.4. For every H_2 molecule detected in the spectrometer, two electrons flowed through the electric circuit. This charge-to-mass conservation is described by Faraday's law of electrolysis: $\phi_{H_2} = I/2F$, where ϕ_{H_2} is the hydrogen flux, I is the current density and F is the Faraday constant. For O_2, the area-normalised derivative of the concentration versus time, $\frac{d[O_2]}{dt \cdot A}$ was also correlated to I via Faraday's law $\phi_{O_2} = \frac{d[O_2]}{dt \cdot A} = I/4F$. The dashed lines in Fig. 7.4 indicate the above Faradaic analysis inferring the H_2 and O_2 flux from experimental I values. The experimental data points of H_2 and O_2 flux match well with the theoretical prediction. This demonstrates that H_2 and O_2 molecules are generated in a 2:1 ratio and confirm that water electrolysis occurs with 100% Faradaic efficiency.

7.4 Non-equilibrium Behaviours

In the last section, we directly demonstrate the water electrolysis in our graphene devices by measuring the gas products. Now let us look back to the non-equilibrium behaviours of these devices systematically.

We measured the dependence of the I-V response in this regime on KOH concentration ($C_{KOH} = 0.1 - 100$ mM) using a three-electrode configuration – both in dark conditions and under illumination. The bias was swept in the intermediate range from $0 - 1$ V.

Figure 7.5 shows that as the voltage bias approaches ~ 0.8 V, the I-V response for low concentration in both dark and bright conditions converges towards the response observed for $C_{KOH} = 100$ mM. As we mentioned in Page 113, in the equilibrium regime, H^+ ions migrate across graphene, leaving OH^- ions behind. This results in proton-hydroxide accumulation on each side of the interface, leading to the proton

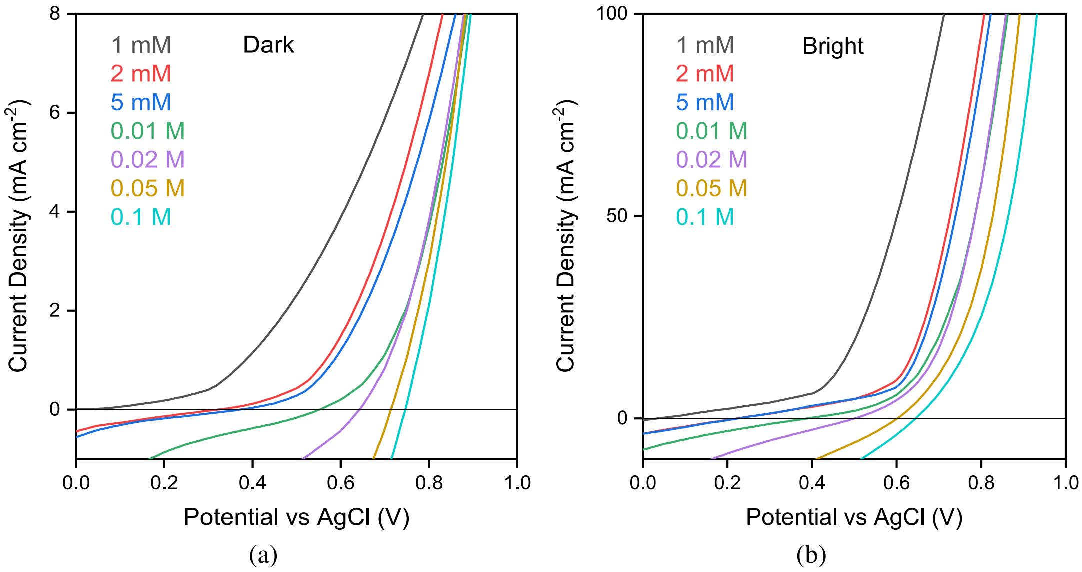

(a)

(b)

Figure 7.5: Typical *I*-*V* characteristics in the nonlinear regime. (a). Current density versus potential of a graphene device measured in potassium hydroxide electrolytes with different concentrations in dark conditions using a three-electrode configuration. (b). *I*-*V* responses of a graphene device measured under illumination (100 $\mathrm{mW \cdot cm^{-2}}$).

activity difference Δa_{H} across graphene. We have demonstrated that high concentration leads to Δa_{H} increases (see Fig. 6.9a), and apparently, voltage has a similar effect, which can be used to explain the *I*-*V* behaviours observed here.

The explanation goes below. High voltage bias drives the reaction away from the equilibrium and producing more proton and hydroxide ions. The higher the voltage bias, the more protons and hydroxide ions generated, thus the greater Δa_{H}. As a result, the *I*-*V* response starts approaching the one observed at a higher concentration. This finding is similar to the behaviour observed in bipolar membranes water electrolysis, in which water dissociation causes proton-hydroxide accumulation at the bipolar interface and thus leads to similar *I*-*V* response in the non-linear regime [153, 155]. This observation is another evidence that proton activity gradients play an important role in driving the *I*-*V* response of these devices.

Next, we study the light response of our devices in the non-equilibrium regime by investigating the dependence of the response with illumination intensity.

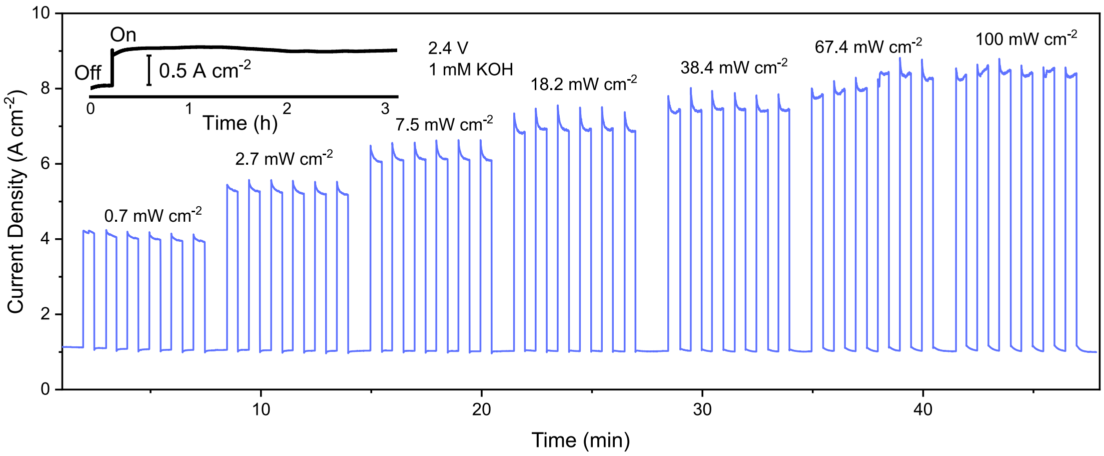

Figure 7.6: Current density versus time under pulsed illumination with intensity gradient. Six measurements were performed for each illumination power density. The experiment was repeatedd for different voltage bias. A summary of these experiments is shown in Fig 7.7. The inset shows the stability results under hours of continuous illumination.

To this end, the solar simulator's aperture diaphragm was used to control the light intensity from 0.1 $\mathrm{mW \cdot cm^{-2}}$ to 100 $\mathrm{mW \cdot cm^{-2}}$. For this experiment, the device was placed in 1 mM hydroxide electrolyte, a fixed voltage was applied to the device, the current was monitored as a function of time, and the light was turned on and off in pulses. The on-off cycles were repeated six times for each voltage bias. Figure 7.6 shows a typical result of this measurement at a fixed voltage (2.4 V).

The same experiments were repeated for different voltages. The results are summarised in Fig. 7.7 As we can see, the current density, I, displayed a saturated dependence with the illumination power density (P) for all voltage bias, which could be described by the empirical relation $I \propto P^{0.2}$. This power dependence $I(P)$ is consistent with the photo-proton effect reported previously [131], in which we demonstrate a proton conductivity enhancement due to hot electrons in graphene (see Section 4.4). At weak illumination of $P \leq 5\ \mathrm{mW \cdot cm^{-2}}$, the power dependence $I(P)$ can be linear approximated (Fig. 7.7a). This yields a photo-responsivity around $3 \times 10^3\ \mathrm{A \cdot W^{-1}}$, which is nearly in the same order of magnitude as the previously reported graphene

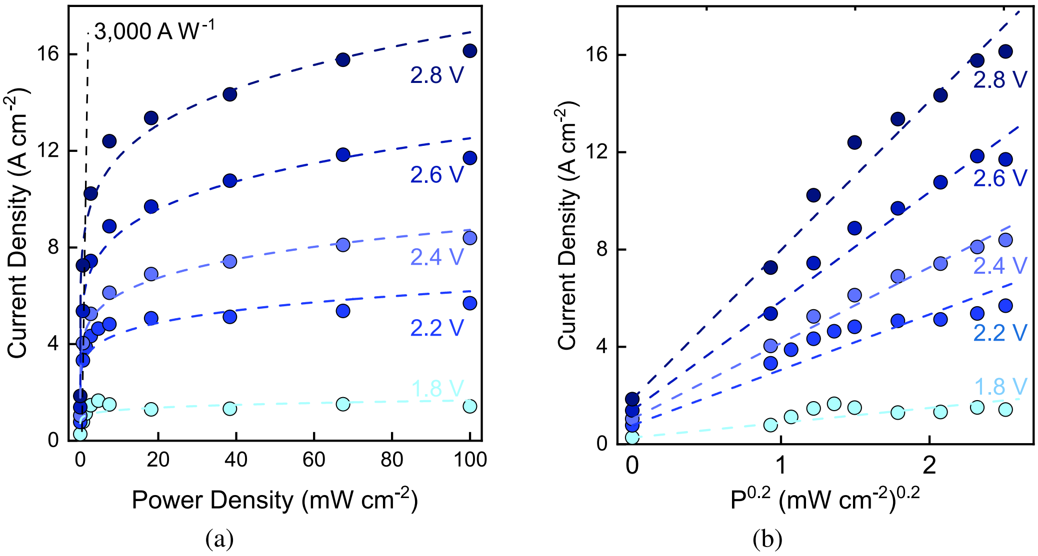

Figure 7.7: Dependence of current density on illumination intensity. (a). Current density as a function of illumination power density P for different voltage biases, measured with one graphene device. The dashed curves are a guide to the eye. The dashed black line indicates responsivity at low illumination powers. (b). The power dependence of I can be described by the relation $I(P) \propto P^{0.2}$. The dashed lines are a guide to the eye.

devices [131]. These agreements further confirm that the increases of proton current under illumination result from light-enhanced conductivity in graphene.

We also performed long-term stability tests over the electrolysis current under illumination. As shown in inset Fig. 7.6, the photo-response was stable over time and showed no signs of deterioration for hours of continuous illumination, which is also in agreement with our previous work [131]. This indicates that both the electrolysis reaction and the light-enhanced proton conductivity of graphene has excellent stability.

7.5 Conclusion

In summary, we performed direct measurement of H_2 and O_2 gases evolving in our micrometre-sized cells, which provides further evidence of water electrolysis. The devices show large water electrolysis current densities that surpass water electrolysis rates in conventional cells by at least an order of magnitude, demonstrating the potential of field effect in accelerating reactions. Systematic investigation on the non-equilibrium behaviours of devices reveals the impact of proton-activity difference to the I-V responses. Further characterisation of the light response confirms that the similar mechanism of light-enhanced proton conductivity in graphene was utilised in our devices.

Chapter 8

Conclusions

Field dissociation of molecules, the Wien effect, has been observed for near one century. Strong E-fields high enough to accelerate these dissociation reactions exist readily near any electrode in electrolytes. Despite that, electrochemical approaches to utilise field effect in water dissociation are still elusive due to screening from the large dielectric constant of water.

In this thesis, we have demonstrated that electric fields can accelerate water dissociation reaction across atomically thick graphene electrodes. Our results show an exponential improvement of water dissociation rate under E-fields up to $10^9\ \mathrm{V \cdot m^{-1}}$. The field-accelerated dissociation found experimentally can be accurately described by Onsager's theory of the Wien effect. The field effect led to water electrolysis current densities exceeding $10\ \mathrm{A \cdot cm^{-2}}$ (at ~ 2 V), which is one-two orders of magnitude higher than state-of-the-art electrolysers. We further verified the occurrence of water electrolysis by direct measuring the rates of H_2 and O_2 gas generation, in which we also demonstrated ideal Faradaic efficiency. By using graphene as a proton selective and gas-impermeable electrode, we can accelerate the water electrolysis reaction and separate the evolved gases in the meanwhile.

The proton activity gradient approach we used provides the ability to perform conductivity measurement in equilibrium conditions. Such a method allows neat and robust quantitative measurements in comparison with conventional methods in the literature. In this thesis, we took advantage of the light-enhanced proton conductivity of graphene to effectively use a more proton-conductive material than graphene to study the field effect in water dissociation and yield a higher electrolysis rate than the conventional cells. With other two-dimensional materials and nano-engineered graphene [132, 156] that have higher proton conductivity, we anticipate that this bench-top setup would achieve faster water electrolysis.

Moreover, this work would be a starting point to study other reactions related to proton transfer, which are of interest in the energy industry, such as CO_2 reduction [157] and hydrogen production from ammonia [158]. Beyond this, the development of 2D electrodes selective to other ions would enable the field effect on a broader scope of chemical reactions.

The E-field approach in this thesis is fundamentally different from the chemical catalytic route. These results are the initial step towards a physical method for accelerating chemical reactions. Further works, such as optimisation and scale-up of our prototype, are needed to realise industry-level applications. Moreover, this field enhancement can also be used in combination with chemical catalysts in BPM water electrolysis [62].

Another intriguing research direction is to exploit the photon-proton effect together with the electric field effect to improve the performance of solar water splitting cells [159, 160]. Solar water splitting is an approach to harvesting solar energy in order to break water molecules to obtain hydrogen, which demands multifunctional membranes/electrodes that are proton–electron conductive, gas impermeable, environmentally stable and optically transparent/sensitive. In this sense, graphene could come into play as a life-changing material.

Bibliography

1. Alberts, B. *et al. Essential cell biology* (Garland Science, 2015) (cit. on p. 13).
2. Bean, B. P. The action potential in mammalian central neurons. *Nature Reviews Neuroscience* **8,** 451–465 (2007) (cit. on p. 13).
3. Larminie, J. & Dicks, A. *Fuel Cell Systems Explained* **1-2,** 285 (John Wiley & Sons, Ltd,., West Sussex, England, Feb. 2003) (cit. on p. 13).
4. Novoselov, K. S. *et al.* A roadmap for graphene. *Nature* **490,** 192–200 (2012) (cit. on p. 13).
5. Hu, S. *et al.* Proton transport through one-atom-thick crystals. *Nature* **516,** 227–230 (Dec. 2014) (cit. on pp. 13, 78–81, 83, 84, 87, 100, 103, 110, 116, 123).
6. Vermaak, L., Neomagus, H. W. & Bessarabov, D. G. Recent advances in membrane-based electrochemical hydrogen separation: A review. *Membranes* **11,** 1–32 (2021) (cit. on p. 13).
7. Kaiser, V., Bramwell, S. T., Holdsworth, P. C. & Moessner, R. Onsager's Wien effect on a lattice. *Nature materials* **12,** 1033–1037 (2013) (cit. on pp. 13, 35, 38, 109, 122).
8. Onsager, L. Deviations from Ohm's law in weak electrolytes. *The Journal of chemical physics* **2,** 599–615 (1934) (cit. on pp. 13, 35, 38, 39, 59, 109, 122).
9. Bard, A. J., Faulkner, L. R. & Aikens, D. A. *Electrochemical methods, fundamentals and applications* **1,** 3–18 (wiley New York, 2010) (cit. on pp. 13, 25, 28, 31, 32, 109, 113).
10. Stuve, E. M. Ionization of water in interfacial electric fields: An electrochemical view. *Chemical Physics Letters* **519-520,** 1–17 (Jan. 2012) (cit. on pp. 14, 34, 59, 62, 109).
11. Zemaitis, J. F., Clark, D. M., Rafal, M. & Scrivner, N. C. *Handbook of Aqueous Electrolyte Thermodynamics* 75 (Wiley, 1986) (cit. on p. 17).
12. Smith, A. M., Lee, A. A. & Perkin, S. The electrostatic screening length in concentrated electrolytes increases with concentration. *The journal of physical chemistry letters* **7,** 2157–2163 (2016) (cit. on p. 20).
13. Pitzer, K. S. *Activity Coefficients in Electrolyte Solutions* (CRC Press, 2018) (cit. on p. 21).
14. Allen, J. B. & Larry, R. F. *Electrochemical methods fundamentals and applications* (John Wiley & Sons, 2001) (cit. on p. 21).

15. Gonella, G. *et al.* Water at charged interfaces. *Nature Reviews Chemistry* **5,** 466–485 (2021) (cit. on p. 22).
16. Helmholtz, H. Ueber einige Gesetze der Vertheilung elektrischer Ströme in körperlichen Leitern mit Anwendung auf die thierisch-elektrischen Versuche. *Annalen der Physik und Chemie* **165,** 211–233 (1853) (cit. on p. 22).
17. Helmholtz, H. Studien über electrische Grenzschichten. *Annalen der Physik und Chemie* **243,** 337–382 (1879) (cit. on p. 22).
18. Gouy, M. Sur la constitution de la charge électrique à la surface d'un électrolyte. *Journal de Physique Théorique et Appliquée* **9,** 457–468 (1910) (cit. on p. 23).
19. Chapman, D. L. LI. A contribution to the theory of electrocapillarity. *The London, Edinburgh, and Dublin Philosophical Magazine and Journal of Science* **25,** 475–481 (Apr. 1913) (cit. on p. 23).
20. Stern, O. The theory of the electrolytic double-layer. *Z. Elektrochem* **30,** 1014–1020 (1924) (cit. on p. 25).
21. Montenegro, A. *et al.* Asymmetric response of interfacial water to applied electric fields. *Nature* **594,** 62–65 (2021) (cit. on pp. 28–30).
22. Wang, X., Liu, K. & Wu, J. Demystifying the Stern layer at a metal-electrolyte interface: Local dielectric constant, specific ion adsorption, and partial charge transfer. *Journal of Chemical Physics* **154** (2021) (cit. on pp. 28–31, 123).
23. Li, C. Y. *et al.* In situ probing electrified interfacial water structures at atomically flat surfaces. *Nature Materials* **18,** 697–701 (2019) (cit. on pp. 28, 30).
24. Bikerman, J. XXXIX. Structure and capacity of electrical double layer. *The London, Edinburgh, and Dublin Philosophical Magazine and Journal of Science* **33,** 384–397 (May 1942) (cit. on p. 28).
25. Wang, H. & Pilon, L. Accurate simulations of electric double layer capacitance of ultramicroelectrodes. *Journal of Physical Chemistry C* **115,** 16711–16719 (2011) (cit. on pp. 29, 30, 109).
26. Fumagalli, L. *et al.* Anomalously low dielectric constant of confined water. *Science* **360,** 1339–1342 (2018) (cit. on p. 30).
27. Booth, F. The dielectric constant of water and the saturation effect. *The Journal of Chemical Physics* **19,** 391–394 (1951) (cit. on p. 30).
28. Shampine, L. F. & Reichelt, M. W. The matlab ode suite. *SIAM journal on scientific computing* **18,** 1–22 (1997) (cit. on p. 32).
29. Dormand, J. R. & Prince, P. J. A family of embedded Runge-Kutta formulae. *Journal of computational and applied mathematics* **6,** 19–26 (1980) (cit. on p. 32).
30. Eckstrom, H. C. & Schmelzer, C. The wien effect: Deviations of electrolytic solutions from ohm's law under high field strengths. *Chemical Reviews* **24,** 367–414 (1939) (cit. on pp. 34, 35, 58).

31. Persoons, A. & Hellemans, L. New electric field methods in chemical relaxation spectrometry. *Biophysical Journal* **24,** 119–134 (1978) (cit. on p. 35).
32. De Levie, R. The electrolysis of water. *Journal of Electroanalytical Chemistry* **476,** 92–93 (1999) (cit. on p. 41).
33. Teschke, O. & Zwanziger, M. G. Operation of a steady-state pH-differential water electrolysis cell. *International Journal of Hydrogen Energy* **7,** 933–937 (1982) (cit. on p. 45).
34. Giesbrecht, P. K. & Freund, M. S. Recent Advances in Bipolar Membrane Design and Applications. *Chemistry of Materials* **32,** 8060–8090 (2020) (cit. on pp. 45, 48, 56, 118, 131).
35. Carmo, M., Fritz, D. L., Mergel, J. & Stolten, D. A comprehensive review on PEM water electrolysis. *International Journal of Hydrogen Energy* **38,** 4901–4934 (Apr. 2013) (cit. on pp. 46, 47).
36. Hunter, B. M., Gray, H. B. & Müller, A. M. Earth-Abundant Heterogeneous Water Oxidation Catalysts. *Chemical Reviews* **116,** 14120–14136 (2016) (cit. on p. 46).
37. Miles, M. *et al.* The oxygen evolution reaction on platinum, iridium, ruthenium and their alloys at 80 C in acid solutions. *Electrochimica Acta* **23,** 521–526 (1978) (cit. on p. 46).
38. Conway, B. E. & Tilak, B. V. Interfacial processes involving electrocatalytic evolution and oxidation of H2, and the role of chemisorbed H. *Electrochimica Acta* **47,** 3571–3594 (2002) (cit. on p. 46).
39. Zwaschka, G., Tong, Y., Wolf, M. & Kramer Campen, R. Probing the Hydrogen Evolution Reaction and Charge Transfer on Platinum Electrodes on Femtosecond Timescales. *ChemElectroChem* **6,** 2675–2682 (2019) (cit. on p. 47).
40. Marković, N. M., Grgur, B. N. & Ross, P. N. Temperature-dependent hydrogen electrochemistry on platinum low-index single-crystal surfaces in acid solutions. *Journal of Physical Chemistry B* **101,** 5405–5413 (1997) (cit. on p. 47).
41. Watzele, S., Fichtner, J., Garlyyev, B., Schwämmlein, J. N. & Bandarenka, A. S. On the Dominating Mechanism of the Hydrogen Evolution Reaction at Polycrystalline Pt Electrodes in Acidic Media. *ACS Catalysis* **8,** 9456–9462 (2018) (cit. on p. 47).
42. Zeng, K. & Zhang, D. Recent progress in alkaline water electrolysis for hydrogen production and applications. *Progress in Energy and Combustion Science* **36,** 307–326 (June 2010) (cit. on pp. 47, 55, 131).
43. Rashid, M. M., Mesfer, M. K. A., Naseem, H. & Danish, M. Hydrogen Production by Water Electrolysis: A Review of Alkaline Water Electrolysis, PEM Water Electrolysis and High Temperature Water Electrolysis. *International Journal of Engineering and Advanced Technology,* 2249–8958 (2015) (cit. on p. 47).

44. Shiva Kumar, S. & Himabindu, V. Hydrogen production by PEM water electrolysis – A review. *Materials Science for Energy Technologies* **2,** 442–454 (2019) (cit. on pp. 47, 56, 131).

45. David, M., Ocampo-Martínez, C. & Sánchez-Peña, R. Advances in alkaline water electrolyzers: A review. *Journal of Energy Storage* **23,** 392–403 (2019) (cit. on p. 47).

46. Vincent, I. & Bessarabov, D. Low cost hydrogen production by anion exchange membrane electrolysis: A review. *Renewable and Sustainable Energy Reviews* **81,** 1690–1704 (2018) (cit. on pp. 47, 56).

47. Mauritz, K. A. & Moore, R. B. State of Understanding of Nafion. *Chemical Reviews* **104,** 4535–4586 (Oct. 2004) (cit. on p. 48).

48. Marino, M. G., Melchior, J. P., Wohlfarth, A. & Kreuer, K. D. Hydroxide, halide and water transport in a model anion exchange membrane. *Journal of Membrane Science* **464,** 61–71 (Aug. 2014) (cit. on p. 48).

49. Elliott, J. A., Wu, D., Paddison, S. J. & Moore, R. B. A unified morphological description of Nafion membranes from SAXS and mesoscale simulations. *Soft Matter* **7,** 6820–6827 (2011) (cit. on pp. 48, 49).

50. Kreuer, K. D. Proton conductivity: Materials and applications. *Chemistry of Materials* **8,** 610–641 (1996) (cit. on p. 49).

51. Marx, D. Proton transfer 200 years after Von Grotthuss: Insights from ab initio simulations. *ChemPhysChem* **7,** 1848–1870 (2006) (cit. on p. 49).

52. Tuckerman, M. E., Marx, D. & Parrinello, M. The nature and transport mechanism of hydrated hydroxide ions in aqueous solution. *Nature* **417,** 925–929 (June 2002) (cit. on pp. 49–51).

53. Agmon, N. *et al.* Protons and Hydroxide Ions in Aqueous Systems. *Chemical Reviews* **116,** 7642–7672 (2016) (cit. on pp. 49–51).

54. Headrick, J. M. *et al.* Chemistry: Spectral signatures of hydrated proton vibrations in water clusters. *Science* **308,** 1765–1769 (2005) (cit. on p. 50).

55. Choi, P., Jalani, N. H. & Datta, R. Thermodynamics and Proton Transport in Nafion. *Journal of The Electrochemical Society* **152,** E123 (2005) (cit. on pp. 50, 51).

56. Tanaka, Y. *Ion Exchange Membranes Fundamentals and Applications Second Edition* 546 (Elsevier, 2007) (cit. on pp. 52, 53).

57. Brauns, J. *et al.* Evaluation of Diaphragms and Membranes as Separators for Alkaline Water Electrolysis. *Journal of the Electrochemical Society* **168,** 014510 (2021) (cit. on p. 55).

58. Vargas-Barbosa, N. M., Geise, G. M., Hickner, M. A. & Mallouk, T. E. Assessing the utility of bipolar membranes for use in photoelectrochemical water-splitting cells. *ChemSusChem* **7,** 3017–3020 (Nov. 2014) (cit. on p. 56).

59. McDonald, M. B., Ardo, S., Lewis, N. S. & Freund, M. S. Use of bipolar membranes for maintaining steady-state pH gradients in membrane-supported, solar-driven water splitting. *ChemSusChem* **7,** 3021–3027 (2014) (cit. on p. 56).
60. Mafé, S., Manzanares, J. A., Ramrez, P. & Termodinamica, D. Model for ion transport in bipolar membranes. *Physical Review A* **42,** 6245–6248 (Nov. 1990) (cit. on pp. 57, 62–64).
61. Simons, R. Water splitting in ion exchange membranes. *Electrochimica Acta* **30,** 275–282 (1985) (cit. on pp. 57, 64).
62. Oener, S. Z., Foster, M. J. & Boettcher, S. W. Accelerating water dissociation in bipolar membranes and for electrocatalysis. *Science* **369,** 1099–1103 (2020) (cit. on pp. 57, 62, 64, 118, 123, 129, 141).
63. Oener, S. Z., Twight, L. P., Lindquist, G. A. & Boettcher, S. W. Thin Cation-Exchange Layers Enable High-Current-Density Bipolar Membrane Electrolyzers via Improved Water Transport. *ACS Energy Letters* **6,** 1–8 (2021) (cit. on pp. 57, 58).
64. Shehzad, M. A. *et al.* Shielded goethite catalyst that enables fast water dissociation in bipolar membranes. *Nature Communications* **12** (2021) (cit. on p. 57).
65. Thiele, S. *et al.* Bipolar membrane electrode assemblies for water electrolysis. *ACS Applied Energy Materials* **3,** 9635–9644 (2020) (cit. on pp. 57, 58).
66. Shen, C., Wycisk, R. & Pintauro, P. N. High performance electrospun bipolar membrane with a 3D junction. *Energy and Environmental Science* **10,** 1435–1442 (2017) (cit. on pp. 57, 58).
67. Chen, Y. *et al.* High-Performance Bipolar Membrane Development for Improved Water Dissociation. *ACS Applied Polymer Materials* **2,** 4559–4569 (2020) (cit. on p. 57).
68. Saitta, A. M., Saija, F. & Giaquinta, P. V. Ab Initio Molecular Dynamics Study of Dissociation of Water under an Electric Field. *Physical Review Letters* **108,** 207801 (May 2012) (cit. on pp. 59, 60).
69. Geissler, P. L., Dellago, C., Chandler, D., Hutter, J. & Parrinello, M. Autoionization in liquid water. *Science* **291,** 2121–2124 (Mar. 2001) (cit. on p. 59).
70. Hassanali, A., Prakash, M. K., Eshet, H. & Parrinello, M. On the recombination of hydronium and hydroxide ions in water. *Proceedings of the National Academy of Sciences* **108,** 20410–20415 (Dec. 2011) (cit. on p. 60).
71. Brüesch, P. & Christen, T. The electric double layer at a metal electrode in pure water. *Journal of Applied Physics* **95,** 2846–2856 (2004) (cit. on pp. 60, 61, 109).
72. Inghram, M. G. & Gomer, R. Mass spectrometric analysis of ions from the field microscope. *The Journal of Chemical Physics* **22,** 1279–1280 (1954) (cit. on pp. 61, 62).

73. Schmidt, W. Massenspektrometrische Untersuchung der Feldionisation von Wasserdampf an Spitzen aus Wolfram, Platin und Iridium. *Zeitschrift für Naturforschung A* **19,** 318–327 (1964) (cit. on pp. 61, 62).

74. Wang, Y., Narayanan, S. R. & Wu, W. Field-Assisted Splitting of Pure Water Based on Deep-Sub-Debye-Length Nanogap Electrochemical Cells. *ACS Nano* **11,** 8421–8428 (2017) (cit. on pp. 62, 63, 118).

75. Rothfuss, C. J., Medvedev, V. K. & Stuve, E. M. The influence of the surface electric field on water ionization: A two step dissociative ionization and desorption mechanism for water ion cluster emission from a platinum field emitter tip. *Journal of Electroanalytical Chemistry* **554-555,** 133–143 (2003) (cit. on p. 62).

76. Li, T. & Hu, W. Electrochemistry in nanoscopic volumes. *Nanoscale* **3,** 166–176 (2011) (cit. on p. 62).

77. Edwards, M. A. *et al.* Nanoscale electrochemical kinetics & dynamics: The challenges and opportunities of single-entity measurements. *Faraday Discussions* **210,** 9–28 (2018) (cit. on p. 62).

78. Blommaert, M. A., Vermaas, D. A., Izelaar, B., In'T Veen, B. & Smith, W. A. Electrochemical impedance spectroscopy as a performance indicator of water dissociation in bipolar membranes. *Journal of Materials Chemistry A* **7,** 19060–19069 (2019) (cit. on p. 64).

79. Novoselov, K. S. *et al.* Electric field in atomically thin carbon films. *Science* **306,** 666–669 (Oct. 2004) (cit. on pp. 65–67, 70, 72).

80. Geim, A. K. & Novoselov, K. S. The rise of graphene. *Nature Materials* **6,** 183–191 (Mar. 2007) (cit. on pp. 65, 66, 71–73, 110).

81. Landau, L. D. Zur Theorie der phasenumwandlungen II. *Phys. Z. Sowjetunion* **11,** 26–35 (1937) (cit. on p. 65).

82. Peierls, R. *Quelques propriétés typiques des corps solides* in *Annales de l'institut Henri Poincaré* **5** (1935), 177–222 (cit. on p. 65).

83. Venables, J. A., Spiller, G. D. & Hanbucken, M. Nucleation and growth of thin films. *Reports on Progress in Physics* **47,** 399–459 (1984) (cit. on pp. 65, 66).

84. Evans, J. W., Thiel, P. A. & Bartelt, M. C. Morphological evolution during epitaxial thin film growth: Formation of 2D islands and 3D mounds. *Surface Science Reports* **61,** 1–128 (2006) (cit. on pp. 65, 66).

85. Castro Neto, A. H., Guinea, F., Peres, N. M. R., Novoselov, K. S. & Geim, A. K. The electronic properties of graphene. *Reviews of Modern Physics* **81,** 109–162 (Jan. 2009) (cit. on pp. 66, 67, 69).

86. Lee, C., Wei, X., Kysar, J. W. & Hone, J. Measurement of the elastic properties and intrinsic strength of monolayer graphene. *Science* **321,** 385–388 (July 2008) (cit. on p. 67).

87. Torres, L. E. F., Roche, S. & Charlier, J.-C. *Introduction to graphene-based nanomaterials: from electronic structure to quantum transport* (Cambridge University Press, 2020) (cit. on p. 67).

88. Mayorov, A. S. *et al.* Micrometer-scale ballistic transport in encapsulated graphene at room temperature. *Nano Letters* **11,** 2396–2399 (2011) (cit. on p. 67).
89. Balandin, A. A. *et al.* Superior thermal conductivity of single-layer graphene. *Nano Letters* **8,** 902–907 (2008) (cit. on p. 67).
90. Wallace, P. R. The Band Theory of Graphite. *Physical Review* **71,** 622–634 (May 1947) (cit. on pp. 67, 68).
91. Katsnelson, M. I. *Graphene: carbon in two dimensions* (Cambridge university press, 2012) (cit. on p. 67).
92. Novoselov, K. S. *et al.* Two-dimensional gas of massless Dirac fermions in graphene. *Nature* **438,** 197–200 (2005) (cit. on pp. 71–73).
93. Bonaccorso, F., Sun, Z., Hasan, T. & Ferrari, A. C. Graphene photonics and optoelectronics. *Nature Photonics* **4,** 611–622 (2010) (cit. on pp. 73, 74).
94. Fai, K., Ju, L., Wang, F. & Heinz, T. F. Optical spectroscopy of graphene : From the far infrared to the ultraviolet. *Solid State Communications* **152,** 1341–1349 (2012) (cit. on pp. 73, 74).
95. Koppens, F. H. *et al.* Photodetectors based on graphene, other two-dimensional materials and hybrid systems. *Nature Nanotechnology* **9,** 780–793 (2014) (cit. on p. 73).
96. Nair, R. R. *et al.* Fine structure constant defines visual transparency of graphene. *Science* **320,** 1308 (June 2008) (cit. on p. 74).
97. Mak, K. F. *et al.* Measurement of the opptical conductivity of graphene. *Physical Review Letters* **101,** 2–5 (2008) (cit. on p. 74).
98. Mak, K. F., Shan, J. & Heinz, T. F. Seeing many-body effects in single- and few-layer graphene: Observation of two-dimensional saddle-point excitons. *Physical Review Letters* **106,** 1–4 (2011) (cit. on p. 74).
99. Xia, F., Mueller, T., Lin, Y. M., Valdes-Garcia, A. & Avouris, P. Ultrafast graphene photodetector. *Nature Nanotechnology* **4,** 839–843 (2009) (cit. on pp. 74, 75).
100. Park, J. & Ruiz-vargas, C. Imaging of Photocurrent Generation and Collection in Single-Layer Graphene 2009. *Nano,* 16–18 (2009) (cit. on pp. 74, 75).
101. Lee, E. J., Balasubramanian, K., Weitz, R. T., Burghard, M. & Kern, K. Contact and edge effects in graphene devices. *Nature Nanotechnology* **3,** 486–490 (2008) (cit. on pp. 74, 75).
102. Gabor, N. M. *et al.* Hot Carrier-Assisted Intrinsic Photoresponse in Graphene. *Science* **334,** 648–652 (Nov. 2011) (cit. on pp. 74–77).
103. Graham, M. W., Shi, S. F., Ralph, D. C., Park, J. & McEuen, P. L. Photocurrent measurements of supercollision cooling in graphene. *Nature Physics* **9,** 103–108 (2013) (cit. on pp. 74, 75, 77).
104. Echtermeyer, T. J. *et al.* Photothermoelectric and photoelectric contributions to light detection in metal-graphene-metal photodetectors. *Nano Letters* **14,** 3733–3742 (2014) (cit. on pp. 74, 75).

105. Lau, C. N. *et al.* Generation of photovoltage in graphene on a femtosecond timescale through efficient carrier heating. *Nature Nanotechnology* **10,** 437–443 (2015) (cit. on p. 74).

106. Wang, X., Cheng, Z., Xu, K., Tsang, H. K. & Xu, J. B. High-responsivity graphene/silicon-heterostructure waveguide photodetectors. *Nature Photonics* **7,** 888–891 (2013) (cit. on pp. 74, 75).

107. Bunch, J. S. *et al.* Impermeable atomic membranes from graphene sheets. *Nano Letters* **8,** 2458–2462 (Aug. 2008) (cit. on p. 78).

108. Koenig, S. P., Wang, L., Pellegrino, J. & Bunch, J. S. Selective molecular sieving through porous graphene. *Nature Nanotechnology* **7,** 728–732 (2012) (cit. on p. 78).

109. Wang, L. *et al.* Molecular valves for controlling gas phase transport made from discrete ångström-sized pores in graphene. *Nature Nanotechnology* **10,** 785–790 (2015) (cit. on p. 78).

110. Sun, P. Z. *et al.* Limits on gas impermeability of graphene. *Nature* **579,** 229–232 (2020) (cit. on pp. 78, 80, 84, 132).

111. Algara-Siller, G. *et al.* Square ice in graphene nanocapillaries. *Nature* **519,** 443–445 (2015) (cit. on p. 78).

112. Sint, K., Wang, B. & Král, P. Selective ion passage through functionalized graphene nanopores. *Journal of the American Chemical Society* **130,** 16448–16449 (2008) (cit. on p. 78).

113. Mogg, L. *et al.* Perfect proton selectivity in ion transport through two-dimensional crystals. *Nature Communications* **10,** 4243 (Dec. 2019) (cit. on pp. 78, 80, 82, 83, 110, 113, 123).

114. Sun, C. *et al.* Mechanisms of Molecular Permeation through Nanoporous Graphene Membranes. *Langmuir* **30,** 675–682 (Jan. 2014) (cit. on p. 78).

115. Sone, Y., Ekdunge, P. & Simonsson, D. Proton Conductivity of Nafion 117 as Measured by a Four-Electrode AC Impedance Method. *Journal of The Electrochemical Society* **143,** 1254–1259 (Apr. 1996) (cit. on p. 79).

116. Schalenbach, M. *et al.* Gas Permeation through Nafion. Part 1: Measurements. *Journal of Physical Chemistry C* **119,** 25145–25155 (2015) (cit. on p. 80).

117. Lozada-Hidalgo, M. *et al.* Sieving hydrogen isotopes through two-dimensional crystals. *Science* **351,** 68–70 (2016) (cit. on pp. 80, 81, 84).

118. Allouche, A., Jelea, A., Ciraci, S., Wang, W. L. & Kaxiras, E. Graphene hydrate: theoretical prediction of a new insulating form of graphene. *New Journal of Physics* **C** (2010) (cit. on p. 81).

119. Miao, M., Nardelli, M. B., Wang, Q. & Liu, Y. First principles study of the permeability of graphene to hydrogen atoms. *Physical Chemistry Chemical Physics* **15,** 16132 (2013) (cit. on p. 81).

120. Tsetseris, L. & Pantelides, S. T. Graphene: An impermeable or selectively permeable membrane for atomic species? *Carbon* **67,** 58–63 (2014) (cit. on p. 81).

121. Feng, Y. *et al.* Hydrogenation Facilitates Proton Transfer through Two-Dimensional Honeycomb Crystals. *Journal of Physical Chemistry Letters* **8,** 6009–6014 (2017) (cit. on pp. 82, 83).

122. Fu, W., Wang, Y., Hu, S., Zhou, X. & Long, X. Hydrogen Isotope Separation via Ion Penetration through Group-IV Monolayer Materials in Electrochemical Environment. *Journal of Physical Chemistry Letters* **10,** 4618–4624 (2019) (cit. on pp. 82, 83).

123. Bartolomei, M., Hernández, M. I., Campos-Martínez, J. & Hernández-Lamoneda, R. Graphene multi-protonation: A cooperative mechanism for proton permeation. *Carbon* **144,** 724–730 (Apr. 2019) (cit. on pp. 82, 84).

124. Fu, W., Hu, S., Zhou, X. & Long, X. Effect of Electrolyte on the Proton Transport through Graphane in the Electrochemical Cell: A First-Principles Study. *Journal of Physical Chemistry Letters* **11,** 3025–3031 (2020) (cit. on pp. 82–84).

125. Kroes, J. M., Fasolino, A. & Katsnelson, M. I. Density functional based simulations of proton permeation of graphene and hexagonal boron nitride. *Physical Chemistry Chemical Physics* **19,** 5813–5817 (2017) (cit. on p. 82).

126. Shi, L., Xu, A., Chen, G. & Zhao, T. Theoretical Understanding of Mechanisms of Proton Exchange Membranes Made of 2D Crystals with Ultrahigh Selectivity. *Journal of Physical Chemistry Letters* **8,** 4354–4361 (2017) (cit. on pp. 82, 83).

127. Achtyl, J. L. *et al.* Aqueous proton transfer across single-layer graphene. *Nature Communications* **6,** 6539 (May 2015) (cit. on pp. 82, 83).

128. Walker, M. I., Braeuninger-Weimer, P., Weatherup, R. S., Hofmann, S. & Keyser, U. F. Measuring the proton selectivity of graphene membranes. *Applied Physics Letters* **107** (2015) (cit. on pp. 82, 83).

129. Li, S. *et al.* Large transport gap modulation in graphene via electric-field-controlled reversible hydrogenation. *Nature Electronics* **4,** 254–260 (2021) (cit. on p. 83).

130. Poltavsky, I., Zheng, L., Mortazavi, M. & Tkatchenko, A. Quantum tunneling of thermal protons through pristine graphene. *Journal of Chemical Physics* **148** (2018) (cit. on p. 84).

131. Lozada-Hidalgo, M. *et al.* Giant photoeffect in proton transport through graphene membranes. *Nature Nanotechnology* **13,** 300–303 (Apr. 2018) (cit. on pp. 84, 87, 100, 103, 124, 125, 137, 138).

132. Mogg, L. *et al.* Atomically thin micas as proton-conducting membranes. *Nature Nanotechnology* **14,** 962–966 (2019) (cit. on pp. 87, 100, 141).

133. Pant, B. D. & Tandon, U. S. Etching of silicon nitride in CCl2F2, CHF3, SiF4, and SF6 reactive plasma: A comparative study. *Plasma Chemistry and Plasma Processing* **19,** 545–563 (1999) (cit. on p. 89).

134. Bean, K. Anisotropic etching of silicon. *IEEE Transactions on Electron Devices* **25,** 1185–1193 (Oct. 1978) (cit. on p. 91).

135. Blake, P. *et al.* Making graphene visible. *Applied Physics Letters* **91** (2007) (cit. on p. 95).

136. Ferrari, A. C. *et al.* Raman spectrum of graphene and graphene layers. *Physical Review Letters* **97,** 1–4 (2006) (cit. on p. 96).

137. Nair, R. R. *et al.* Graphene as a transparent conductive support for studying biological molecules by transmission electron microscopy. *Applied Physics Letters* **97,** 22–25 (2010) (cit. on p. 96).

138. Tombros, N. *et al.* Large yield production of high mobility freely suspended graphene electronic devices on a polydimethylglutarimide based organic polymer. *Journal of Applied Physics* **109** (2011) (cit. on p. 98).

139. Bolotin, K. I. *et al.* Ultrahigh electron mobility in suspended graphene. *Solid State Communications* **146,** 351–355 (2008) (cit. on p. 98).

140. Shi, Y. *et al.* CuO-Functionalized Silicon Photoanodes for Photoelectrochemical Water Splitting Devices. *ACS Applied Materials and Interfaces* **8,** 696–702 (2016) (cit. on p. 105).

141. Lin, S. *et al.* Electrochemical Water Oxidation by a Catalyst-Modified Metal–Organic Framework Thin Film. *ChemSusChem* **10,** 469 (2017) (cit. on p. 105).

142. Revsbech, N. P. An oxygen microsensor with a guard cathode. *Limnology and Oceanography* **34,** 474–478 (1989) (cit. on pp. 105, 106).

143. Hwang, S.-t., Tang, T. E. S. & Kammermeyer, K. Transport of dissolved oxygen through silicone rubber membrane. *Journal of Macromolecular Science, Part B* **5,** 1–10 (Mar. 1971) (cit. on p. 105).

144. Takae, K. & Onuki, A. Molecular Dynamics Simulation of Water between Metal Walls under an Electric Field: Dielectric Response and Dynamics after Field Reversal. *Journal of Physical Chemistry B* **119,** 9377–9390 (2015) (cit. on p. 109).

145. Yang, Q. *et al.* Capillary condensation under atomic-scale confinement. *Nature* **588,** 250–253 (2020) (cit. on p. 110).

146. Merle, G., Wessling, M. & Nijmeijer, K. Anion exchange membranes for alkaline fuel cells: A review. *Journal of Membrane Science* **377,** 1–35 (2011) (cit. on p. 111).

147. Fogler, M. M., Guinea, F. & Katsnelson, M. I. Pseudomagnetic fields and ballistic transport in a suspended graphene sheet. *Physical Review Letters* **101,** 1–4 (2008) (cit. on p. 120).

148. Stygar, W. A. *et al.* Water-dielectric-breakdown relation for the design of large-area multimegavolt pulsed-power systems. *Physical Review Special Topics - Accelerators and Beams* **9,** 1–9 (2006) (cit. on p. 120).

149. Williams, C. D., Dix, J., Troisi, A. & Carbone, P. Effective Polarization in Pairwise Potentials at the Graphene-Electrolyte Interface. *Journal of Physical Chemistry Letters* **8,** 703–708 (2017) (cit. on p. 121).

150. Grosjean, B., Bocquet, M. L. & Vuilleumier, R. Versatile electrification of two-dimensional nanomaterials in water. *Nature Communications* **10,** 1–8 (2019) (cit. on p. 121).

151. Eigen, M. Methods for investigation of ionic reactions in aqueous solutions with half-times as short as 10 –9 sec. Application to neutralization and hydrolysis reactions. *Discuss. Faraday Soc.* **17,** 194–205 (1954) (cit. on p. 123).

152. Tanaka, Y. Water dissociation reaction generated in an ion exchange membrane. *Journal of Membrane Science* **350,** 347–360 (2010) (cit. on p. 123).

153. Vermaas, D. A., Sassenburg, M. & Smith, W. A. Photo-assisted water splitting with bipolar membrane induced pH gradients for practical solar fuel devices. *Journal of Materials Chemistry A* **3,** 19556–19562 (2015) (cit. on pp. 129, 136).

154. Lagadec, M. F. & Grimaud, A. Water electrolysers with closed and open electrochemical systems. *Nature Materials* **19,** 1140–1150 (2020) (cit. on p. 131).

155. Vermaas, D. A., Wiegman, S., Nagaki, T. & Smith, W. A. Ion transport mechanisms in bipolar membranes for (photo)electrochemical water splitting. *Sustainable Energy and Fuels* **2,** 2006–2015 (2018) (cit. on p. 136).

156. Wang, L. *et al.* Fundamental transport mechanisms, fabrication and potential applications of nanoporous atomically thin membranes. *Nature Nanotechnology* **12,** 509–522 (2017) (cit. on p. 141).

157. Liu, M. *et al.* Enhanced electrocatalytic CO2 reduction via field-induced reagent concentration. *Nature* **537,** 382–386 (2016) (cit. on p. 141).

158. Davis, S. J. *et al.* Net-zero emissions energy systems. *Science* **360,** eaas9793 (June 2018) (cit. on p. 141).

159. Symes, M. D. The Artificial Leaf: Recent Progress and Remaining Challenges. *Makara Journal of Science* **20,** 155–159 (Dec. 2016) (cit. on p. 141).

160. Chabi, S., Papadantonakis, K. M., Lewis, N. S. & Freund, M. S. Membranes for artificial photosynthesis. *Energy and Environmental Science* **10,** 1320–1338 (Mar. 2017) (cit. on p. 141).